

INTEGRATED OPTICAL MODULATORS BASED ON PHOTONIC CRYSTALS

A THESIS SUBMITTED TO
THE GRADUATE SCHOOL AND APPLIED SCIENCES
OF
MIDDLE EAST TECHNICAL UNIVERSITY

BY

ALPEREN GÖVDELI

IN PARTIAL FULFILLMENT OF THE REQUIREMENTS
FOR
THE DEGREE OF MASTER OF SCIENCE
IN
ELECTRICAL AND ELECTRONICS ENGINEERING

JULY 2018

Approval of the Thesis:

**INTEGRATED OPTICAL MODULATORS BASED ON PHOTONIC
CRYSTALS**

Submitted by **ALPEREN GÖVDELİ** in partial fulfillment of the requirements for the degree of **Master of Science in Electrical and Electronics Engineering Department, Middle East Technical University** by,

Prof. Dr. Halil Kalıpçılar
Dean, Graduate School of **Nature and Applied Science** _____

Prof. Dr. Tolga Çiloğlu
Head of Department, **Electrical and Electronics Engineering** _____

Assist. Prof. Dr. Serdar Kocaman
Supervisor, **Electrical and Electronics Engineering Dept., METU** _____

Examining Committee Members:

Prof. Dr. Özlem Aydın Çivi
Electrical and Electronics Engineering Dept., METU _____

Assist. Prof. Dr. Serdar Kocaman
Electrical and Electronics Engineering Dept., METU _____

Assoc. Prof. Dr. Özgür Ergül
Electrical and Electronics Engineering Dept., METU _____

Assoc. Prof. Dr. İsa Navruz
Electrical and Electronics Engineering Dept., Ankara University _____

Prof. Dr. Barış Akaoglu
Physics Engineering Dept., Ankara University _____

Date: **04.07.2018**

I hereby declare that all information in this document has been obtained and presented in accordance with academic rules and ethical conduct. I also declare that, as required by these rules and conduct, I have fully cited and referenced all material and results that are not original to this work.

Name, Last name : Alperen GÖVDELI

Signature :

ABSTRACT

INTEGRATED OPTICAL MODULATORS BASED ON PHOTONIC CRYSTALS

Gövdeli, Alperen

MS., Department of Electrical and Electronics Engineering

Supervisor: Asst. Prof. Dr. Serdar Kocaman

July 2018, 100 pages

Photonic Crystals, artificial optical structures making manipulation of the light possible, have become a popular platform since their first development. Here, such optical components are studied theoretically and their unusual behaviors are utilized for integrated optics components. In particular, ability to change the effective index contribution of photonic crystals is exploited for the design of a low-voltage and area efficient integrated optical modulator. Variety of different aspects are compared between the existing on-chip modulator implementations and a novel approach based on photonic crystals is presented for further improvement. The proposed design is a Mach-Zehnder interferometer whose arms contain identical photonic crystal slabs. In order to create a relative phase along the arms of the interferometer, plasma dispersion effect is utilized where the novelty of the design comes from the source of the phase shift. Unlike the existing optical modulators in the literature, plasma dispersion effect is used to perform a band-to-band transition on the photonic crystal at the operation wavelength. According to the numerical analyses performed on photonic band diagram of photonic crystals, such transition provides a huge effective index change leading to a large phase shift, which results in the possibility of extremely small device sizes and low operation voltages for a proper intensity modulation at the output at extremely high speeds.

Keywords: Optical modulators, Mach-Zehnder Interferometer, Photonic Crystal

ÖZ

FOTONİK KRİSTAL TABANLI ENTEGRE OPTİK MODÜLATORLER

Gövdeli, Alperen

Yüksek Lisans, Elektrik ve Elektronik Mühendisliği Bölümü

Tez Yöneticisi: Dr. Öğr. Üyesi Serdar Kocaman

Temmuz 2018, 100 sayfa

Işığın manipülasyonunu mümkün kılan yapay malzemelerden olan fotonik kristaller ilk defa geliştirildikleri günden bugüne oldukça popüler bir platform haline geldi. Burada bu yapılar teorik olarak çalışıldı ve sıra dışı davranışları entegre optik bileşenlerde kullanıldı. Özellikle optik sistemlerde kırıcılık indisine olan katkısını değiştirebilme özelliği, düşük voltajda çalışan ve kapladığı alan açısından verimli bir entegre optik modülatör geliştirmek için kullanıldı. Halihazırda var olan entegre modülatörler birçok farklı açıdan karşılaştırıldı ve yeni bir yöntem sunuldu. Yapı temel olarak kolları birbirine eş fotonik kristaller bulunduran Mach-Zehnder interferometresidir. Kollar arasında faz farkı oluşturmak için plazma dağılım etkisi kullanıldı. Fakat, sunulan yapının seleflerinden farkı üretilen faz kaymasının kaynağıdır. Başka bir deyişle plazma dağılım etkisi optik dalga boyunda çalışan modülatördeki fotonik kristalin fotonik bantları arasında geçişi sağlamak için kullanılmıştır. Yapılan sayısal analizlere göre banttan banda geçiş fotonik kristalin kırıcılık indisinde yüksek miktarda değişikliğe yol açarak büyük faz farkları oluşmasını ve dolayısıyla da normal bir optik modülasyon işleminin daha küçük yapılarla ve elektriksel gerilimlerle yüksek hızlarda gerçekleşmesini mümkün kılmıştır.

Anahtar Kelimeler: Optik Modülatör, Mach-Zehnder İnterferometre, Fotonik Kristal

Aileme...
To My Family...

ACKNOWLEDGMENTS

I would like to express my gratitude to my advisor Assist. Prof. Dr. Serdar Kocaman for his guidance and support throughout my graduate studies. He was the reason for me to start studying in photonics. Since my undergraduate education, I have had the chance to improve myself in terms of both theoretical and experimental work under his supervision. It is a privilege for me to work with him and use research opportunities provided by him.

I am thankful to Prof. Dr. Özlem Aydın Çivi, Assoc. Prof. Dr. Özgür Ergül, Assoc. Prof. Dr. İsa Navruz and Prof. Dr. Barış Akaoğlu for accepting to be on my thesis committee.

During this study, I acknowledge the financial support of TUBITAK BİDEB 2210-A 2016-1 Scholarship Program.

I would like to thank my friends Utku Karaca and Murat Can Sarihan for their contributions to this thesis, technical comments and suggestions, as well as their friendship. Also, I would like to thank all my friends in METU for touching my life in many ways.

I am deeply grateful to my mother Zeliha and my father Yalçın for their endless love, care and support. They were my first teachers and they had an important effect on me to have an interest in science. Without the sacrifices they made, I would not be the person I am today. Their thrust and belief on me has pushed me forward throughout my life and their presence has given me confidence. I would like to thank my sister Züleyha and brother Tuğrul for their love and coloring my life. I am thankful to my love Büşra for her never-ending love, support and encouragement. She is always patient with me even if I drive her crazy. Since the day we met, she has been always with me in any difficulty that I encountered. She supports me all the time and never lets go of my hand. I am the luckiest person in the world to have her in my life.

TABLE OF CONTENTS

ABSTRACT.....	v
ÖZ.....	vi
ACKNOWLEDGMENTS.....	viii
TABLE OF CONTENTS.....	ix
LIST OF TABLES.....	xii
LIST OF FIGURES.....	xiii
LIST OF SYMBOLS AND ABBREVIATIONS.....	xvi
CHAPTERS	
1. INTRODUCTION.....	1
1.1. Background: Optical Communication System.....	1
1.2. Components of Optical Communication.....	5
1.2.1. Optical Sources.....	5
1.2.2. Fiber Optic Cables.....	6
1.2.3. Modulation.....	8
1.2.4. Receivers.....	11
1.3. Integrated Photonic.....	12
2. OPTICAL MODULATORS.....	15
2.1. Controlling the Index of Materials.....	16
2.1.1. Franz-Keldysh Effect and Quantum-Confined Stark Effect...	16
2.1.2. Kerr's Effect and Pockel's Effect.....	16
2.1.3. Thermal Modulation.....	17
2.1.4. Plasma Dispersion Effect.....	17
2.2. Intensity Modulation.....	20
2.3. Mach-Zehnder Interferometers (MZI).....	21

2.3.1.	Basic Working Principle.....	22
2.3.2.	Mach-Zehnder Interferometer Based Modulators	24
2.4.	Ring Resonators.....	27
2.4.1.	Basic Working Principle.....	28
2.4.2.	Ring Resonator Based Modulators.....	31
2.5.	Figure of Merits.....	32
3.	PHOTONIC CRYSTALS.....	35
3.1.	Theory.....	36
3.2.	Numerical Analysis Methods.....	41
3.2.1.	Photonic Band Structure.....	41
3.2.2.	Equipfrequency Contours.....	42
3.2.3.	Electric Field Distribution.....	43
3.3.	Photonic Crystal Slab.....	44
3.4.	Effective Refractive Index Calculations.....	46
3.4.1.	Field Distribution.....	47
3.4.2.	Snell’s Law.....	48
3.4.3.	EFCs.....	51
4.	PHOTONIC BAND-TO-BAND TRANSITION BASED OPTICAL MODULATOR.....	53
4.1.	Band Gap Adjustment.....	55
4.2.	Band-to-Band Transition.....	57
4.3.	The P-I-N Diode.....	61
4.3.1.	Determination of Diode Parameters.....	61
4.3.2.	The structure of the Proposed P-I-N Diode.....	63
5.	RESULTS AND DISCUSSION.....	65
5.1.	Optical Modulation Operation.....	65
5.2.	Modulation Speed.....	67
5.3.	Optical Insertion Loss.....	68
5.4.	DC Analysis of the Device.....	69
5.5.	Tuning Range.....	72
5.6.	Field Distribution During Optical Modulation.....	73

6. CONCLUSION AND FUTURE WORK.....	75
REFERENCES.....	79
APPENDICES	
A. PHOTONIC BAND DIAGRAM.....	89
B. EQUI-FREQUENCY CONTOURS.....	91
C. FIELD DISTRIBUTION FOR PHASE ACCUMULATION.....	95
D. FIELD DISTRIBUTION (APPLICATION OF SNELL’S LAW).....	97

LIST OF TABLES

TABLES

Table 6.1. Comparison of several designs in the literature with the proposed design.....	77
--	----

LIST OF FIGURES

FIGURES

Figure 1.1. The entire electromagnetic spectrum.....	2
Figure 1.2. Schematic representation of the electrical communication.....	3
Figure 1.3. Schematic illustration of a fiber optic cable.....	6
Figure 1.4. Optical loss spectrum in a single mode fiber.....	7
Figure 1.5. Illustration of the direct modulation with laser diode.....	8
Figure 1.6. Illustration of the external modulation with laser diode.....	9
Figure 1.7. Schematic representation of optical communication with direct and external modulation.....	10
Figure 1.8. Schematic representation of a photodiode composed of p-n structure.....	12
Figure 2.1. Different structures for carrier transport: (a) p-n diode, (b) p-i-n diode, (c) MOS capacitor.....	19
Figure 2.2. Interference of different waves: (a) Constructive interference of two in-phase waves, (b) Destructive interference of two out-of-phase waves.....	21
Figure 2.3. Basic structure of a Mach-Zehnder interferometer.....	22
Figure 2.4. Normalized optical intensity at the output for phase difference between the waves in the arms of the MZI.....	24
Figure 2.5. MZI based optical modulator structures: (a) MZI with p-i-n diode whose intrinsic region is simple waveguide as a phase shifter, (b) MZI with photonic crystal waveguide on both arms, (c) MZI with photonic crystal waveguide and pull-push drive on both arms.....	26
Figure 2.6. Basic structure of a ring resonator.....	27
Figure 2.7. Model of a ring resonator composed of a single waveguide and a ring with radius of r	28
Figure 2.8. Representative spectral normalized intensity of a single ring resonator.....	30
Figure 2.9. Schematic structure of a ring resonator based optical modulator with p-i-n diode.....	31

Figure 2.10. Representative spectral intensity of a single ring resonator for different resonance conditions.....	32
Figure 3.1. Representative schema of a photonic crystal slab composed of an air hole hexagonal lattice with radius of r , thickness of h and lattice constant of a	36
Figure 3.2. Diagrams of hexagonal and square lattices in real and reciprocal spaces	40
Figure 3.3. PhC slab structure in the form of SOI.....	44
Figure 3.4. Photonic band diagram of the PhC with hexagonal air-hole lattice of radius $0.3a$, thickness $0.6a$ for TM-like polarization.....	45
Figure 3.5. Electric field distribution and field profile along the PhC slab with hexagonal lattice on oxide ($r=0.3a$, $h=0.6a$, $a=0.5\mu\text{m}$) at the normalized frequency of 0.26 and 0.32 ($\omega a/2\pi c$).....	48
Figure 3.6. Schematic representation of the light refraction at the boundary of two different medium with refractive indices.....	49
Figure 3.7. The propagation in PhC obtained via FDTD method for the incoming light with the frequencies of (a) 0.26 ($\omega a/2\pi c$) and (b) 0.32 ($\omega a/2\pi c$).....	50
Figure 3.8. The EFC plots for the PhC slab of hexagonal lattice with air-holes (radius of $r=0.3a$, thickness of $h=0.6a$ where lattice constant is $a=0.5\mu\text{m}$) for the frequencies at the (a) first and (b) second photonic bands.....	52
Figure 4.1. (a)The illustration of the proposed design which is a MZI-based optical modulator. (b) Schematic representation of the p-i-n diode.....	54
Figure 4.2. (a) Band diagrams of silicon PhCs with hexagonal lattice (thickness of $0.6a$) on SOI for different radii of air-hole. (b) Size of the first band gaps for different radius.....	56
Figure 4.3. (a) Schematic representation of the MZI-based optical modulator for off-state (blue-solid) and on-state (red-dashed). (b) The band diagram of the phase shifter (PhC) for TM-like polarization at two states.....	59
Figure 4.4. Effective refractive index of the phase shifter (PhC) calculated via EFCs at the off-state (blue-circle, solid) and on-state (red-rectangle, dashes) of the modulator.....	60
Figure 4.5. Schematic representation of the proposed p-i-n whose intrinsic region is the PhC with hexagonal lattice.....	63
Figure 4.6. (a) The operation voltage values for different doping densities in order to obtain carrier injection of $4.1 \times 10^{18} \text{ cm}^{-3}$ in the intrinsic region (PhC) (b) Free carrier concentration in PhC during on-state for various operation voltages in the proposed p-i-n diode.....	64

Figure 5.1. (a) Spectral phase difference between the arms during on-state ($V_{sig}=1.091V$) for the wavelength range of 1542nm-1557nm. (b) Spectral phase difference between the arms during on-state ($V_{sig}=1.091V$) for the wavelength range of 1542nm-1557nm.....	66
Figure 5.2. Time response of the current passing through the p-i-n diode under the forward bias obtained via time dependent simulations on the diode.....	67
Figure 5.3. Optical transmission spectrum for the reference (no-diode, red-solid) and device arms (diode biased with 1.091V, blue-dashes) of the MZI during on-state.....	68
Figure 5.4. DC characteristics of the proposed p-i-n diode.....	69
Figure 5.5. (a) The total charge accumulated in the intrinsic region (PhC) for different forward biases. (b) Diffusion capacitance of the diode for varying voltage under forward bias condition.....	71
Figure 5.6. Photonic band diagrams for various biasing voltages. As the biasing voltage increases the bands shift more (from 3 nm to 11 nm with 2.4V)	72
Figure 5.7. Operation bandwidth of the modulator for different on-state voltages. The bandwidth increases with increasing voltages.....	73
Figure 5.8. (a)Electric field distributions on the phase shifter regions (PhC) along the reference and device arms of the MZI during on-state with $V_{DC}=2.4V$ at the wavelength of 1.55 μ m. (b) Field profile of the waves at the input side (c) Field profile of the waves at the output side.....	74

LIST OF SYMBOLS AND ABBREVIATIONS

UHF	ultra-high frequency
VHF	very-high frequency
EMI	electromagnetic interference
RFI	radio-frequency interference
EMP	electromagnetic impulses
LED	light emitting diode
ILD	injection laser diode
AM	amplitude modulation
FM	frequency modulation
E_g	energy band gap
$h\nu$	energy of light with frequency of ν
Δn	refractive index change
MZI	Mach-Zehnder Interferometer
Gb/s	Gigabit per second
APF	all-pass filter
NF	notch filter
PhC	photonic crystal
DBR	distributed Bragg reflectors
VCSELs	vertical cavity surface emitting lasers
ϵ_0	permittivity of the vacuum
μ_0	permeability of the vacuum
ϵ	relative permittivity
μ	relative permeability
BZ	Brillouin zone
IBZ	irreducible Brillouin zone

FDTD.....	finite-difference time-domain
EFCs.....	equi-frequency contours
TM.....	transverse magnetic
SOI.....	silicon-on-insulator

CHAPTER 1

INTRODUCTION

1.1 Background: Optical Communication System

Since the beginning of the human civilization, communication has become an important need, which results in improvement of various communication systems. The most primitive ways of transmitting the signals in the form of voice or light from one place to another were using smoke or signaling fire.

During the sixth century BCE, the first mailing system was established in Persia Empire to communicate between long distances in the country. Then, other ancient nations such as Rome, Egypt and China constructed their own postal services. In fifth century BCE, by relying on their ability to find the way to their nest regardless of how long the distance is, pigeons were used for mailing. These are examples for communication in ancient times.

When we come to the history closer today, in fifteenth century using flags was one of the methods to symbolize each letter or number and to communicate. In 1672, it was discovered by Robert Hooke that sound waves could be transmitted over wires. After the discovery of electricity, communication has gained a new way and direction.

The invention of the telegraph in 1838 was the beginning of the electrical communication [1]. It was followed by the invention of the telephone in 1876. In proceeding years, larger data rates and information capacities were obtained via electrical systems. This can be also explained with the widening in the electromagnetic spectrum (Fig.1.1) that can be used for data sending and receiving through the communication systems. Electrical communication systems use communication

channels that are based on the superimposing the main signal (information) with a sinusoidal electromagnetic signal (carrier). This process relies on the frequency of the carrier signal since it is directly related to the transmission bandwidth. In other words, the larger the transmission bandwidth, the larger the information capacity conveyed is. For instance, high carrier frequencies such as UHF and VHF have been used for radio communication, which are shown in electromagnetic spectrum in Fig.1.1.

The idea is sending the signal to the destination via a transmission medium. In a communication system (i.e. electrical communication system), a modulator, which is required to modulate the main signal (information) with an electrical signal used as carrier signal, transmission medium and demodulator, which obtains the information from the modulated signal transmitted through transmission medium. The schematic representation of a typical communication system is shown in Fig. 1.2. The transmission medium could be a copper line, which is mostly a coaxial cable, or free space on which a radio link is created. In all type of transmission mediums, there are some nonidealities such as attenuation of the signal due to loss, degradation due to noise coming from the environment and distortions associated with the medium. Such undesired effects can be tolerable up to some distances of the transmission path. After that distance information would be corrupted. Thus, in order to eliminate the signal attenuation and distortions, and to increase the signal amplitude so that it could be detected at the output properly, repeaters and amplifiers are placed at certain intervals along the transmission link.

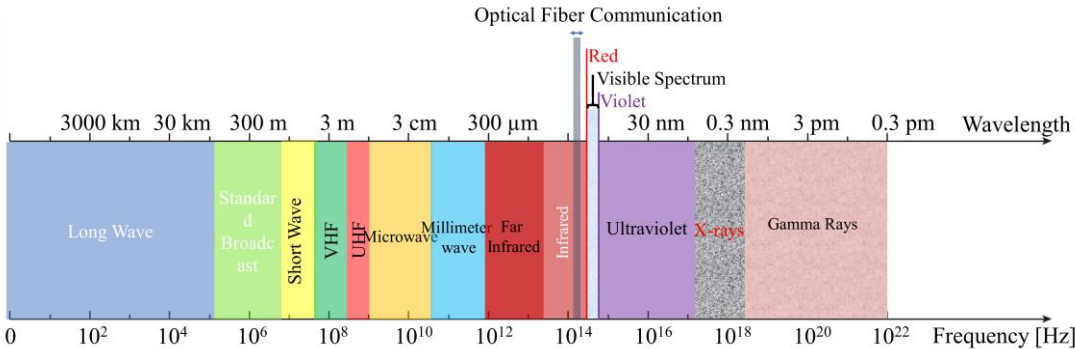


Figure 1.1. The entire electromagnetic spectrum [2]

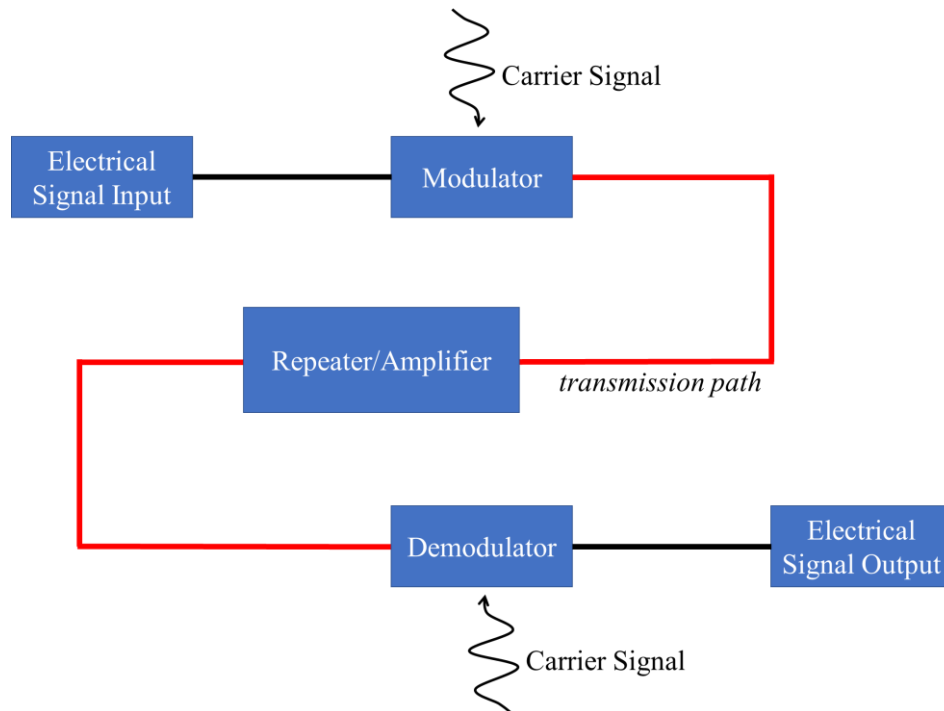


Figure 1.2. Schematic representation of the electrical communication. It contains modulator/demodulator, repeater and transmission path (red line).

As time passed, with the motivation to increase the data rate, which means sending more information, and to increase the distance at which the information could be transmitted, optical communication systems were developed. Although it has been used for many years (its first examples are signaling fire, mirrors and signaling lamps), the mile stone for the optical communication in today's sense was the invention of the laser [3]. Due to its coherent light output and ability to modulate the light, long distance communication gained the ability to transmit and receive much more data with high speeds. Especially, development of optical fibers and dielectric waveguides in order to carry the optical signals provided longer transmission distances and better transmission performances. Therefore, the copper based electrical transmission lines have been replaced with their optical counterparts, optical fiber lines, for a long time.

Optical fiber communication has several advantages that explain this replacement as follows.

- Optical fibers have much more data capacity compared to electrical transmission lines. Although a typical electrical coaxial cable has transmission bandwidth of ~20MHz, an optical carrier frequency on the

order of terahertz provides much more potential transmission bandwidth. Moreover, this is only for one optical carrier frequency and optical systems present the opportunity to use wavelength division multiplexing, which multiplies the number of channels on a single optical transmission path [4,5].

- The optical loss for communication wavelength in silicon fiber is extremely small ($\sim 0.2\text{dB/km}$). This makes possible transmission of data in long distances without much data loss and reduces the requirement for amplification of the signal.
- Unlike electrical lines, fiber optical cables are not affected from electromagnetic interference (EMI), radio-frequency interference (RFI) or electromagnetic impulses (EMPs). Thus, they do not require a shielding from these noises.
- Optical fibers are safe for human and environment since they do not create an arc or spark. Also, they are made from glass or plastic polymer, they do not conduct electricity and can safely be used in electrically noisy environment.
- Optical fibers have small size and weight. Their diameter is generally not larger than that of a human hair. This reduces the cost to lay a communication line.
- The optical transmission medium is made of sand and it is less expensive compared to copper-based transmission lines. Also, with the development on the interconnect technologies, repeaters used to increase the signal amplitude suffered from the loss has started to become all-optic rather than previous electronic based interconnects, which reduced the cost.

An optical communication system is based on similar concepts in a typical communication system. They contain an optical source to generate the light as carrier, fiber optic cables as medium for transmission, modulator for light modulation and superimposing carried signal with carrier signal or transforming electrical signal into optical signal, and an optical receiver for collecting the transmitted information at the output of the transmission line.

1.2 Components of an Optical Communication

1.2.1 Optical Sources

In the case of optical communication system, the incoming information is transmitted with optical source through optical transmission path, which is fiber optic cable, and obtained in the receiver. The main optical sources used for fiber optic communication are light-emitting diodes (LEDs) and injection laser diodes (ILD) due to their compatibility to optical fiber, high efficiency and suitability to large scale of optical applications [6,7,8]. Although both sources have similar structure which is p-n junction made up of III-V semiconductor material with direct-band-gap, their output profiles are different. To be more specific, the light coming from the LED is incoherent. On the contrary, laser diodes can produce coherent output. The reason for such a difference is that optical energy generated in a laser diode relies on optical resonant cavity. This structure produces both spatial and temporal coherent light. In other words, the output of a laser diode is directional and monochromatic. On the other hand, the outcome of a LED has a broad spectral width and an optical power distributed with cosine function on a hemisphere, which is also called Lambert's cosine law. Therefore, these two types of optical sources are used in different applications. For example, LEDs are more suitable to short-distance communication with multimode fiber, which transmits more than one optical wavelength on a single fiber [6]. On the other hand, laser diodes are used in long distance communication systems with single mode fibers as well as systems with multimode fiber.

1.2.2 Fiber Optic Cables

Fiber optic cables are the analogy of electrical coaxial cables in optical communication systems. They are transmission channels, which are made of dielectric materials, for long/short distance optical communication.

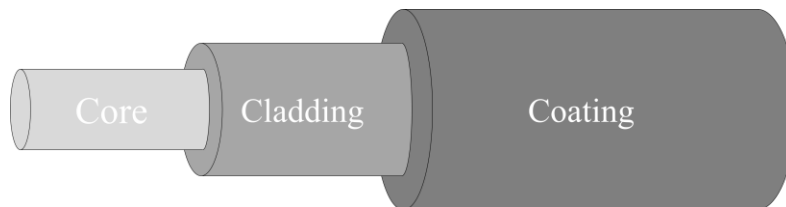


Figure 1.3. Schematic illustration of a fiber optic cable. Basically, it consists of core, cladding and coating layers.

They are composed of three nested structures namely core, cladding and coating (Fig. 1.3). The light is confined to the core and propagates inside that region. Core is surrounded by another region called cladding. Both core and cladding are made up of silica (SiO_2), but the refractive indices of these regions are not the same. There is a slight difference in the indices ($n_{\text{core}} > n_{\text{cladding}}$) which is the reason for the propagation of the light in the fiber along the long distances. The function of the outermost layer, coating, is to protect the inner layers from environmental effects. Optical fibers are divided into two types namely multimode and single mode. The first one is used in short distance communication and has relatively large core diameter compared to the other one. As the name suggest, it confines more than one mode inside the fiber at the same time. Since it carries large number of light signals in a single structure, it is subjected to undesired effects such as dispersion, which limits the maximum distance along which signals are transmitted. The second type of fiber, single mode fiber, confines only one optical mode inside the fiber and has a very small core diameter. It can be used for long distance communication due to their relatively high tolerance to the nonidealities such as dispersion and optical loss. As mentioned before, the maximum distance that an optical power transmitted is determined by the optical loss inside the optical fibers since signal is attenuated during the transmission

and receivers at the output require a level of optical power to detect the signal. Therefore, optical loss is important for optical communication systems.

The optical loss is not the same for different optical wavelengths [9]. There are three major factors determining the optic loss spectrum for fiber optic cables. At short wavelengths, Rayleigh scattering in the SiO₂ becomes dominant, whose effect is inversely proportional to fourth power of the wavelength ($1/\lambda^4$). At high wavelengths, intrinsic absorption occurs due to the molecules of SiO₂. Also, there is an extrinsic absorption due to the impurities inside the fiber material. These effects create three transmission windows namely first, second and third window. The lowest loss occurs near 1.55 μ m, which is the common transmission wavelength used in optical communication systems. The optical loss spectrum and windows are shown in Fig. 1.4.

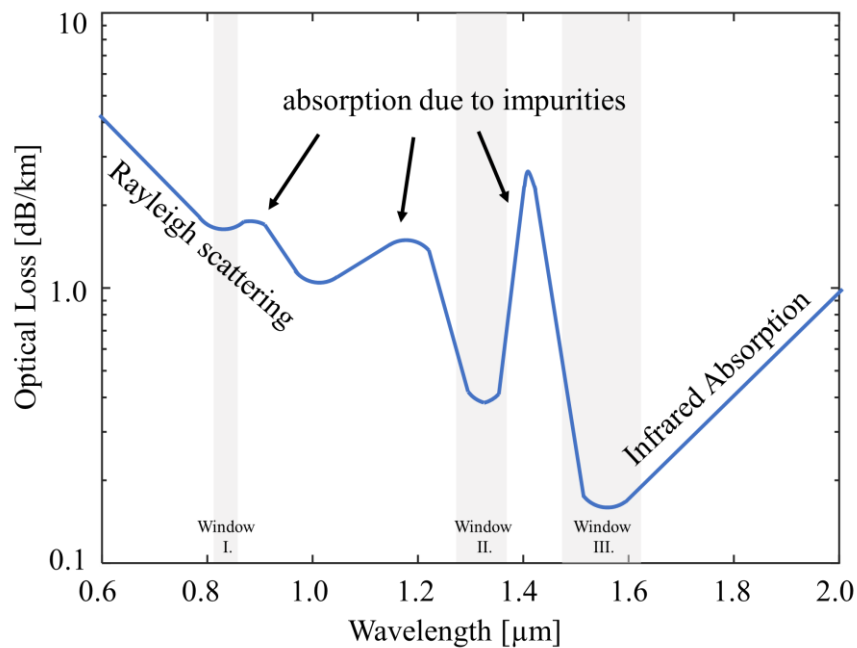


Figure 1.4. Optical loss spectrum in a single mode fiber. There are three optical windows used for communication.

1.2.3 Modulation

The process of transforming the electrical data into optical data is called modulation. The signal transmitted through the optical channel is the optical carrier modulated with the electrical signal (information). The modulation process could be performed for analog or digital signal. The analog modulation may use amplitude (AM) or frequency (FM) modulation techniques and requires a high signal-to-noise ratio for receiver part as well as a linearity at the optical source [10]. Therefore, analog signal modulation is not preferable for many optical applications [10,11]. For the digital modulation, high and low light intensity is coded with on (mark) and off (space) pulses, respectively. Such signal stages correspond to “1” and “0” bits. This process is the intensity modulation and it is quite common since its detection at the output of the communication system can be performed via a simple photodetector whose photocurrent is proportional to intensity of the incoming optical signal. However, there are other types of modulations such as phase, frequency or polarization as well.

In a communication system, the implementation of the modulation could be in two ways. One of them is direct modulation. Light beam is emitted only when the electrical incoming signal (to be transmitted) become logic “1” (mark). In other words, a laser diode is toggled as “on” and “off” for “1” and “0” bits, respectively as shown in Fig. 1.5. This process is performed by the driving current as an electrical signal, which is proportional to the optical output of a laser diode. However, since it relies on driving the optic source directly with data, it can be used for relatively slower systems compared to the external modulation [12].

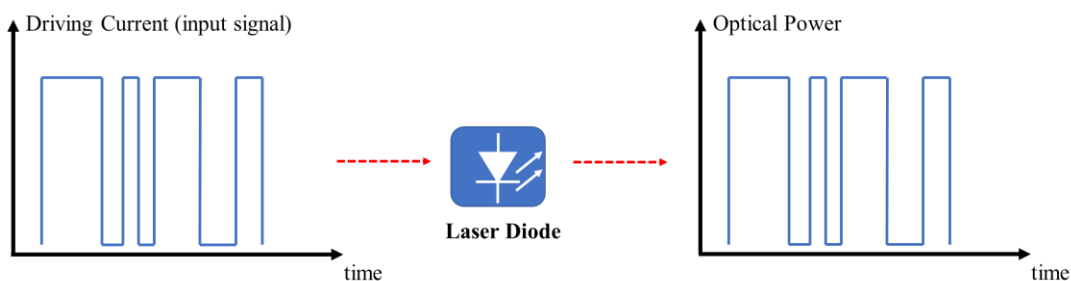


Figure 1.5. Illustration of the direct modulation with laser diode. The laser diode is driven by the current associated with the electrical input signal and the transmitted optical signal is generated.

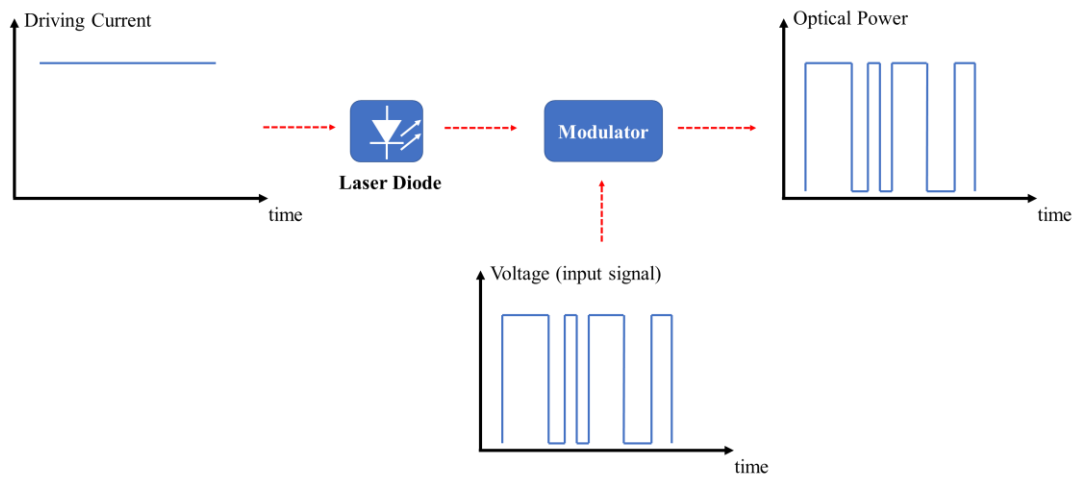


Figure 1.6. Illustration of the external modulation with laser diode. Laser diode emits constant light and an extra component is used to modulate the light according to the input signal.

Other way of modulation is external modulation. In this case, laser diode emits light constantly and an external component called modulator is used in order to switch the light according to the modulating electrical signal applied to the modulator. When the electrical signal is high (mark), the transmitted optical signal becomes high, vice versa. Optical modulators will be discussed in the section 2.1. Different types of modulation are illustrated in the schematic representations of optical communication systems in Fig. 1.7.

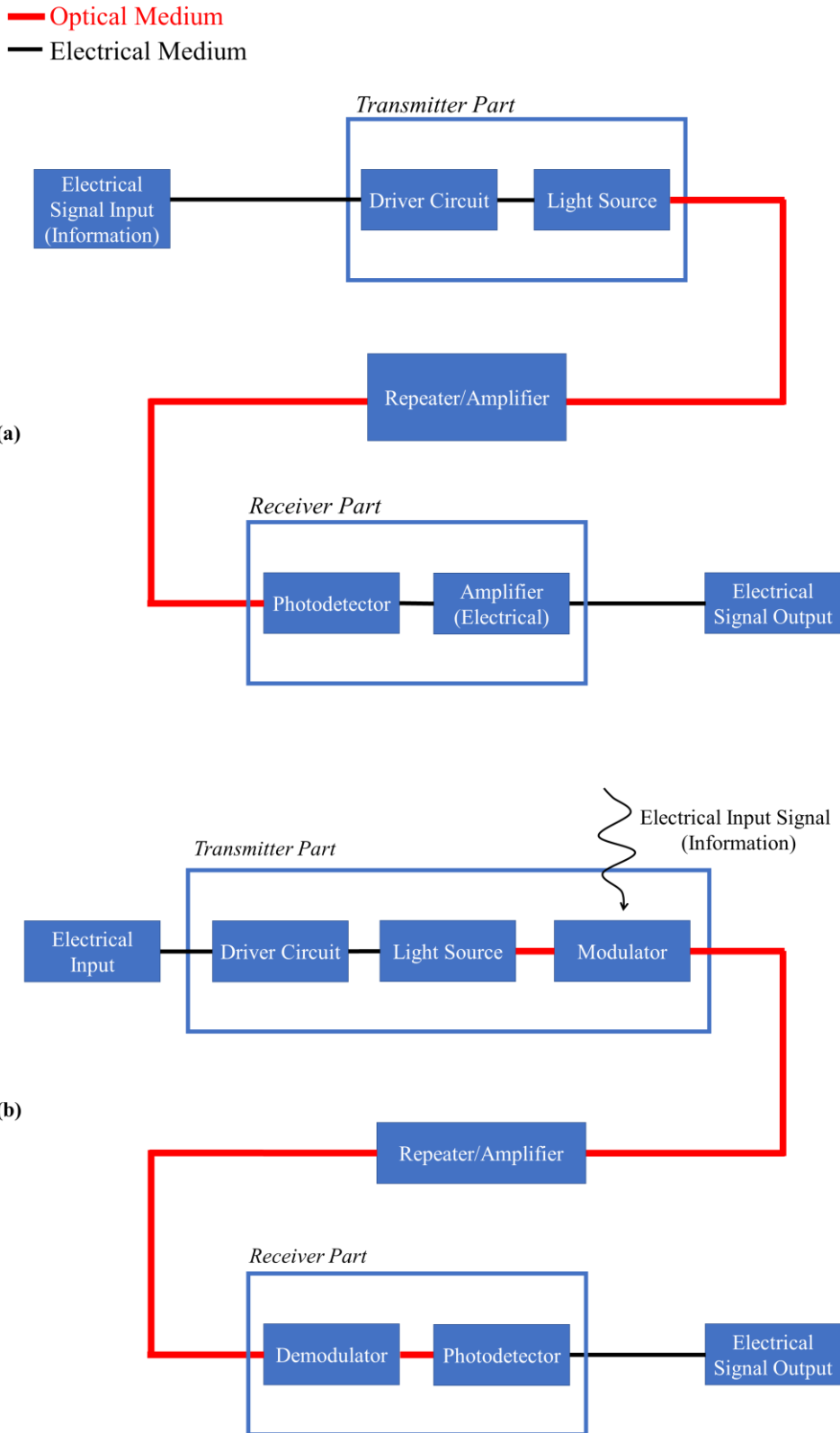


Figure 1.7. Schematic representation of optical communication with **(a)** direct modulation and **(b)** external modulation. In both systems, electrical (black lines) and optical (red lines) mediums were used along the transmission.

1.2.4 Receivers

The final step in an optical system is to receive the transmitted optical signal and convert it into electrical signal. It is performed via photodetectors. In general photodetectors are photodiodes composed of p-n or p-i-n junction structures. A photodiode works under reverse bias and when light falls photons are absorbed by the junction. If the energy of the incoming light is high enough to break the bond between the valence electron and the parent atom (generally silicon atom), the electron becomes free and can move freely with the electric field in the environment. The empty place that electron left behind is called hole and behaves like a positive charge. Note that n-type and p-type materials are produced by doping the main material with some specific atoms so that dominant electron or hole concentration occurs in the materials, respectively. For the case of photodiode with p-n junction (Fig. 1.8), a light absorption creates electron-hole pairs throughout the junction. The minority carriers (holes in n-type material, electrons in p-type material) in the depletion region are subjected to built-in and external electric field. Thus, electrons move towards n-type doped region and reach positive terminal of the voltage source. On the contrary, motion of holes is towards p-typed doped region inside the diode and they reach negative terminal. When no optical illumination available, the current is extremely small. Note that such current is independent from the reverse bias and only related to minority carriers in p-n junction, whose concentration can be increased with the light illumination. Depending on the photon falling on the structure photocurrent increases. Consequently, optical signal (light) is converted to electrical signal (current). It is only one example -a simple one- for photodetector. There are more complicated structures in the literature. Moreover, various semiconductor materials such as Si, Ge, GaAs and InP have been utilized in detectors [13].

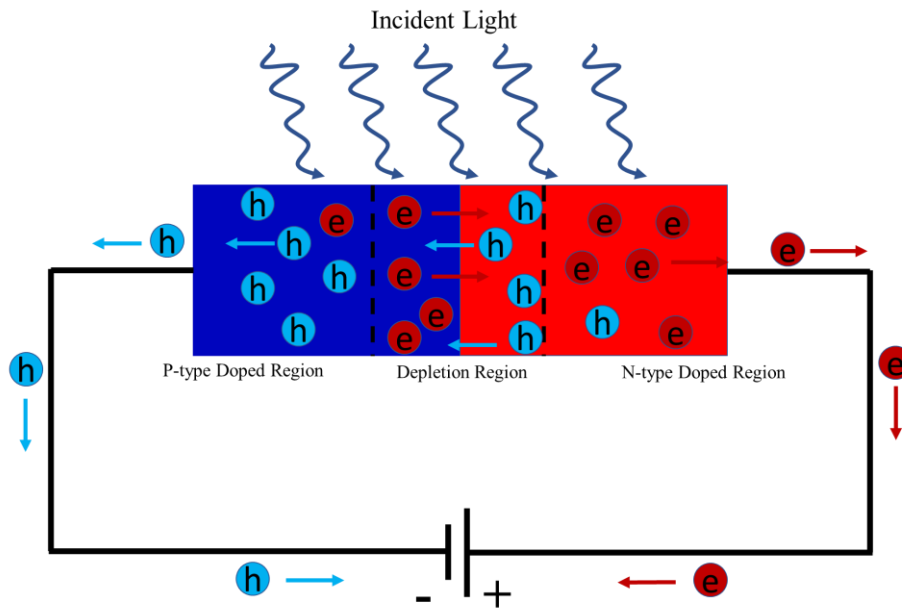


Figure 1.8. Schematic representation of a photodiode composed of p-n structure. The dark current exists at no-illumination condition and is not affected by reverse bias. Light illumination creates electron-hole pair, which gain motion via electric field. This results in photocurrent.

1.3 Integrated Photonics

One of the most popular concepts for optical communication is the fiber optic cables as mentioned in previous sections. The long and short distance data transmissions have been performed with such components. Moreover, with the new developments on fabrication technology, optical data transfer has taken place in fiber-to-device, device-to-device and chip-to-chip connections. After transmission, the data is processed and utilized in electronic systems. At this point, we start to talk about integrated circuits and systems on chip scale. Such structures contain various components on a single circuit or chip and the number of components has been tried to increased for a long time with advances on CMOS technology. In fact, there is a famous rule called Moore's law [14] stating that the number of transistors in an integrated circuit doubles in every two years. For years it has been applied in the semiconductor industry. Even memory capacities and number of pixels in cameras have been increased parallel to this rule. In order to fit more and more component in an integrated chip, sizes of components have been reduced. CMOS fabrication techniques made such integration

possible. Starting from 10 μ m in the first processor [15] in 1971, the feature sizes have been reduced to 14 nm in 2014 [15]. Consequently, as the components shrink, more component can be fitted in electronic chips, which results in much more processing speeds and higher computation efficiency. However, rate of this improvement has been slow down year-by-year since size of the transistors has been getting close to the physical limits. In fact, the diameter of a silicon atom is \sim 0.2 nm and currently minimum feature size available corresponds to nearly 70 silicon atoms. Therefore, as a promising method photonic integrated circuits (PICs) has been considered to obtain higher speed and performance for a while [16-18].

Like electronic components specialized for specific objectives, various photonic components have been developed. In silicon photonics, light is guided in silicon. It is a pure crystal material and fabricated as wafers. Surfaces of silicon wafers are oxidized and SiO₂ layer is created under a thin silicon layer, which is called silicon-on-insulator (SOI). Waveguides and other photonic components can be formed from this silicon layer. Although name of the area is silicon photonics, by adding different elements such as Germanium (Ge), Gallium Arsenide (GaAs), Boron (B) or Phosphorus (P), various structures can be obtained. For instance, with Ge or GaAs, one can fabricate photodetectors [19] or optical amplifiers [19,20]. By doping the silicon with B and P, photodiodes or optical modulator [29] can be produced. Photonic components can be divided into two groups namely passive and active elements. The components in the first group do not possess a dynamic interaction with the light. For instance, grating couplers [21,22], which is used for emitting or receiving light to vertical surfaces, or polarization splitters having different coupling capacities for different polarization states [23] are under the scope of the first group. Active elements, on the other hand, have dynamic light-matter interaction. The examples for such components are photodetectors [24-26], optical amplifiers [27,28] and optical modulators, which is also the focus of this thesis. Implementation of all these optical components on a single chip is the photonic integration.

The topic of this thesis is a new type of optical modulator. Until the proposed design is explained, first different types of optical modulators are mentioned in terms of operation principles. In chapter 2, main principles of optical modulators such as control of material index are explained. Different methods to provide such control are mentioned and compared. Among these methods, plasma dispersion effect is explained in detail since it is used in the proposed design here. Also, two structures namely Mach-Zehnder Interferometers and ring resonators for the intensity modulation, which is required in optical systems, are examined in terms of both operation principles and figure of merits such as modulation speed, footprint, optical bandwidth, power consumption and optical insertion loss.

Since the proposed optical modulator relies on photonic crystals, such structures are important for this study. Different computations on photonic crystals were conducted throughout the study. Therefore, in chapter 3, the theory of photonic crystals and numerical methods to examine photonic crystals are mentioned.

In chapter 4, the proposed optical modulator design is explained step-by-step. First, photonic crystal, which covers the phase shifter region of the modulator, is designed. Second, p-i-n diode structure, which provides the electrical operation, is designed and examined.

In chapter 5, the optical modulator, whose design procedure is explained in chapter 4, is analyzed in terms of phase modulation, switching speed, optical insertion loss, DC characteristics and tuning range.

In chapter 6 chapter, the overall design procedures, analysis results of the structure and the upcoming studies based on this theoretical work is mentioned.

CHAPTER 2

OPTICAL MODULATORS

An optical modulator is a device that is used to modulate the optical signal by changing several characteristics of the light such as amplitude, phase or polarization. Such a control on the light can be achieved by applying an electric field to the medium of the modulator, which leads to a change in index of the medium. This type of modulation can be named as electro-optic modulation.

Index of a medium has real and imaginary parts as shown in eq. 2.1. Both parts of the index can be altered via applied electric field.

$$N = n + iK \quad (2.1)$$

where N , n and K are the index, refractive index and absorption index of the material, respectively. When we express electrical field component of the light wave as a plane wave (eq. 2.2), then the effects of the change in real and imaginary parts of the index become clearer.

$$|\vec{E}| = Ae^{iN\frac{2\pi}{\lambda}d} = Ae^{i(n+iK)\frac{2\pi}{\lambda}d} = Ae^{in\frac{2\pi}{\lambda}d} e^{-K\frac{2\pi}{\lambda}d} \quad (2.2)$$

$$\phi = n\frac{2\pi}{\lambda}d \quad (2.3)$$

where A , λ , d and ϕ are constant related to the amplitude of the electric field, the wavelength of the light, propagation distance along the corresponding material and phase accumulated along the material, respectively. As the equation 2.2 stated, refractive index is related to the phase (ϕ) and does not affect magnitude of the electric field, which means the intensity of the light. On the other hand, change in imaginary part, which is the absorption index, controls the intensity of the light. Therefore, using electric field to manipulate the light by altering the real and imaginary parts of the material index is known as electro-refractive and electro-absorptive modulation,

respectively [29]. Although the latter one can be used directly to change the intensity of the light with the applied electric field, electro-refraction type modulations requires several processes in order to be used in an optical system, which will be mentioned following sections in this chapter.

2.1 Controlling the Index of Materials

2.1.1 Franz-Keldysh Effect and Quantum-Confined Stark Effect

Electro-absorption modulation relies on the effect of the applied electric field on the energy band diagram of the bulk semiconductor that light passing through. In order a light to be absorb with a material, the energy of the light should be larger than the energy band gap of the corresponding material ($h\nu > E_g$). Otherwise, the absorption of a photon is not possible. However, even for this case, if an electric field is applied to the medium, the band diagram of the material is tilted such that wavefunctions of valence and conduction bands are partially overlap, which means a tunneling occurs. Such a stage gives rise to an absorption whose effectiveness increases with increasing electric field. This effect is known as Franz-Keldysh effect [30,31,32]. The reflection of this effect on quantum-well structures is the Quantum-Confined Stark effect [32]. Franz-Keldysh effect is used only with the materials III-V semiconductors and lacks of high extinction ratio [32].

2.1.2 Kerr's Effect and Pockel's Effect

Electro-refractive modulation is based on the change of refractive index of the medium along which the light propagates. There are different methods to achieve this change such as Kerr's effect and Pockel's effect. The Kerr's effect is the change of the refractive index anisotropically with applied electric field. In other words, electric field applied to the material makes the material birefringent. That is, the refractive index of the material is different for different directions. Such an index change is quadratically proportional to the magnitude of the applied electric field ($\Delta n \propto |E|^2$). This effect is strong in amorphous materials and several liquids such as nitrobenzene and nitrotoluene [33,34]. Like Kerr's effect, the Pockel's effect is the change of refractive

index when an external electric field is applied to the material. The latter one has much lower effect on the material and its effect is observed on the crystal structures without inversion symmetry. The proportionality relation between the index change due to Pockel's effect and the applied electric field is linear ($\Delta n \propto |E|$) [35].

The traditional methods such as Franz-Keldysh effect, Quantum-Confined Stark, Kerr's effect and Pockel's effect used in order to change the index and to create a modulating medium with electric field are not suitable to be applied to silicon for telecommunication systems due to their insufficient index change in silicon [36,37]. Therefore, different approaches have been developed to use silicon in optical modulation applications.

2.1.3 Thermal Modulation

One of the methods to achieve high enough refractive index changes in silicon is to use the thermal modulation. It is an effective approach due to the high thermo-optic coefficient of the silicon ($\sim 1.8 \times 10^{-4} \text{ K}^{-1}$) [38]. The basic structure of such a modulation contains a silicon waveguide in which light to be modulated propagates and a metallic microheater on the waveguide [39]. However, the presence of the metallic surface induces a light absorption and in order to eliminate this optical loss, a silicon dioxide (SiO_2) is placed between silicon waveguide and metallic heater. Since the thermal conductivity of the silicon oxide is low ($\sim 1.44 \text{ Wm}^{-1}\text{K}^{-1}$), oxide layer limits the heat transfer and speed of the thermal modulation [39,40]. Thus, thermal modulation approach consumes high power and the switching process is slow [29]. Another method for silicon-based index change is plasma dispersion effect.

2.1.4 Plasma Dispersion Effect

Plasma dispersion effect is the change of refractive index due to free electron and hole carrier concentration available in the medium. Unlike other methods for phase modulation, the index shift here is not associated directly with the electric field applied to the material. On the contrary, the electric field controls the carrier density inside the optical material. Its effect could be exploited in many different materials. Especially for silicon this method is appropriate to be used in telecommunication purposes due to

high enough index shift of the plasma dispersion effect in silicon. The relation between the free carrier concentration in silicon and refractive index change was examined experimentally by Soref and Bennet [36]. According to the results based on the experimental work the index change with carrier density is given by eq. 2.4 (eq. 2.5) for the optical wavelength of 1.55 μm (1.3 μm) [36].

$$\Delta n = \Delta n_e + \Delta n_h = \{-8.8 \times 10^{-22} \times (\Delta N_e)\} + \{-8.5 \times 10^{-18} \times (\Delta N_h)^{0.8}\} \quad (2.4)$$

$$\Delta n = \Delta n_e + \Delta n_h = \{-6.2 \times 10^{-22} \times (\Delta N_e)\} + \{-6 \times 10^{-18} \times (\Delta N_h)^{0.8}\} \quad (2.5)$$

where Δn , Δn_e , Δn_h , ΔN_e and ΔN_h are the change in refractive index due to both electron and hole carriers, index change due to only electron carriers, index change due to only hole carriers, change in the electron concentration, and change in hole concentration, respectively.

The electrical manipulation on the carriers in an optical system can be performed via different mechanisms such as carrier injection, depletion or accumulation with the help of traditional electrical semiconductor structures such as p-n, p-i-n diodes or MOS structures, whose representative schematics are shown in Fig. 2.1.

For the carrier depletion, a p-n junction is formed as given in Fig. 2.1-a. A depletion region is created between p and n type-doped regions. The width and effect of this region is controlled by the reversed bias. The larger the bias is, the larger the depletion region is. In other words, the depleted carriers are concentrated with the increasing reverse bias. The carrier injection, on the other hand, requires an intrinsic region between n and p type-doped regions (Fig.2.1-b). The intrinsic silicon region is sandwiched between highly doped regions. The carriers injected into the undoped region, which is also the optical waveguide region, in the middle when a forward bias is applied to the device. The structure for carrier accumulation process is similar to a p-n junction. In order to accumulate the carriers, an oxide layer (SiO_2) is placed between the doped materials. The overall structure is some kind of a capacitor. All these three processes of carrier motion can be performed via a MOS structure with different biasing and doping states (Fig.2.1-c).

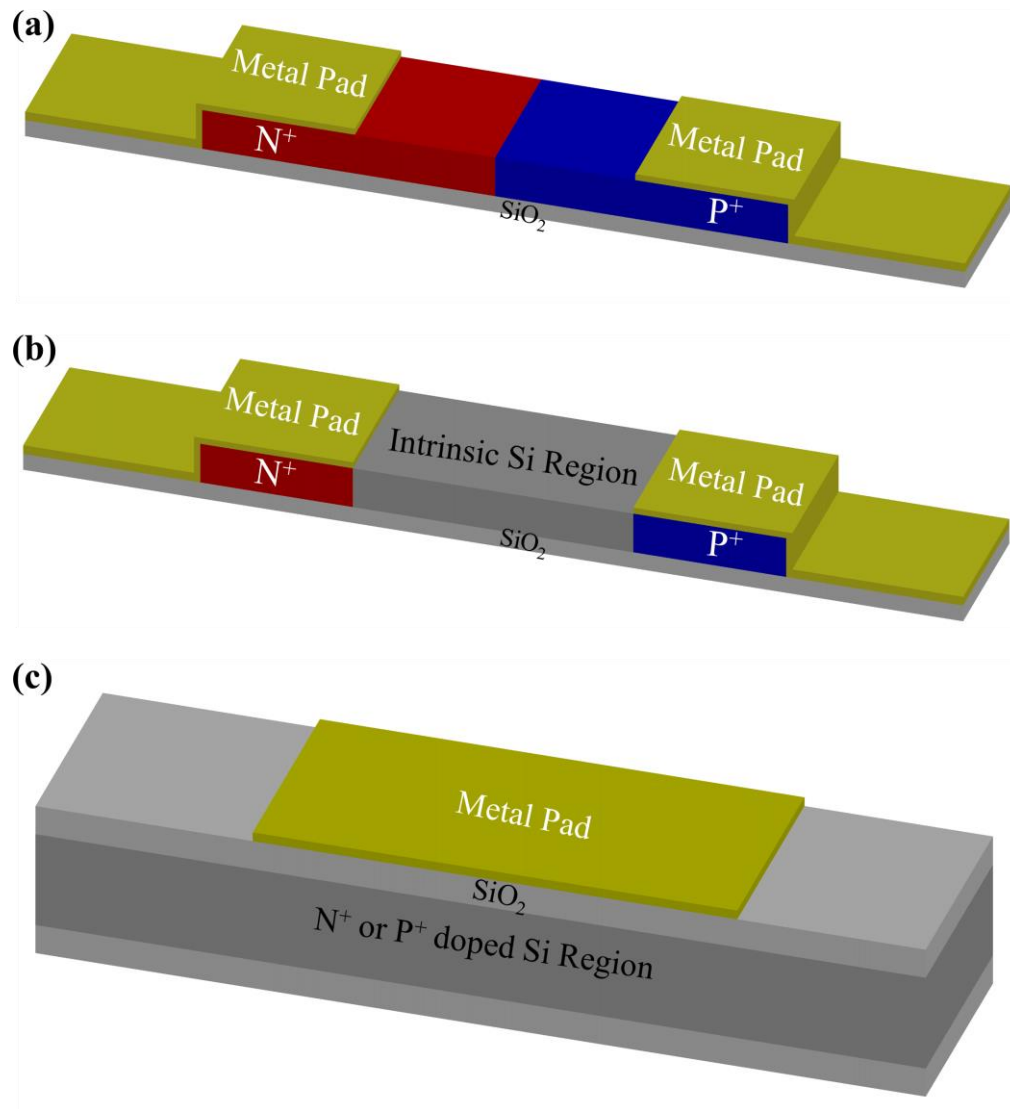


Figure 2.1. Different structures for carrier transport. (a) p-n diode (b) p-i-n diode (c) MOS capacitor. Red, blue and red colored areas represent the n-doped silicon, p-doped silicon regions, and metal pad, respectively. All structures have a silicon bulk layer at the bottom, which is not shown in the illustrations. Depending on the biasing and the physical structure of the device, the behavior of the carriers changes as injection, depletion or accumulation.

2.2 Intensity Modulation

The light beam propagating in the medium whose refractive index is controlled via plasma dispersion effect is modulated in terms of phase according to the eq. 2.3. The detection process at the output of the communication systems relies on intensity detection. In other words, the information transmitted along the optical medium is coded with the light intensity. Thus, intensity control is necessary. Although the alteration in the imaginary part of the refractive index can be directly exploited in intensity modulation, change in the real part of the refractive index, which is associated with the phase of the light as stated in previous sections, requires several structures for transforming the modulation into intensity modulation and to be used in communication systems. There are several approaches for such transformation. Two of the most popular methods are using Mach-Zehnder Interferometer (MZI) or Ring Resonator.

2.3 Mach-Zehnder Interferometers (MZI)

Interference is an optical phenomenon occurred when two waves encounters at the same medium. The resulting wave is the superposition of the two waves. Interference can be different levels such as constructive and destructive. When the incoming waves are in-phase, which means no phase difference between waves, then the resulting wave is the sum of the incoming waves (Fig. 2.2-a). On the other hand, if the waves are out-of-phase, which means there is a π radian phase difference between the waves, they cancel each other (Fig. 2.2-b) during the interference. There are different types of interferometers such as Michelson, Sagnac, Fabry-Perot Interferometers. Mach-Zehnder interferometer is another type of interferometer. It can be used not only on optics but also in integrated photonics. Due to its simplicity in production, it is very common device in chip-scale applications (Fig. 2.3).

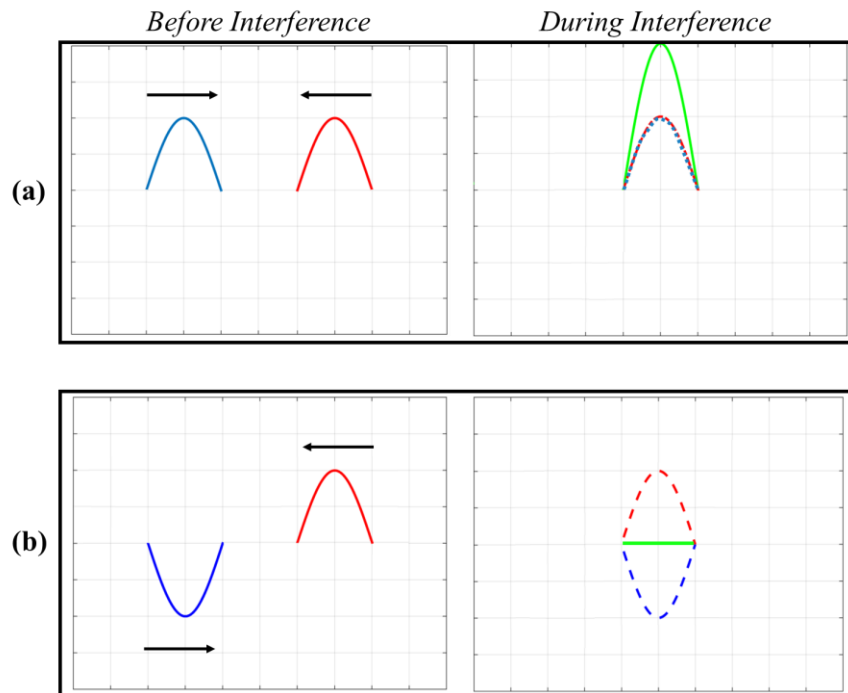


Figure 2.2. Interference of different waves. **(a)** Constructive interference of two in-phase waves. The resulting wave (green-solid) has an intensity which is sum of the waves. **(b)** Destructive interference of two out-of-phase waves. The resulting wave (green-solid) has zero amplitude since waves cancel each other.

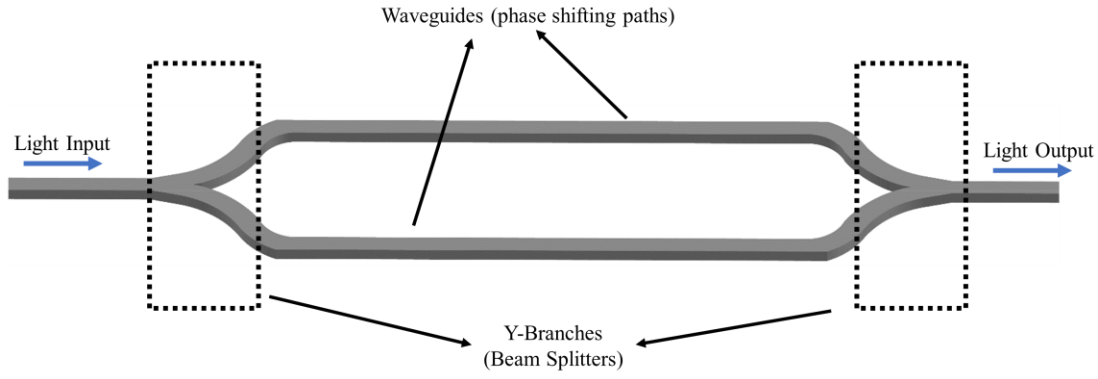


Figure 2.3. Basic structure of a Mach-Zehnder interferometer. It is composed of two Y-branches and two single mode waveguides between splitters.

In a typical MZI as shown in Fig. 2.3, there are two Y-branches, which act as a 3dB splitter or beam splitter, at both input and output sides. The input power is divided into two halves at the input splitter. The half signals propagate through the two arms of the MZI, which are waveguides with the same physical and optical length in general. At the output splitter, the incoming signals interfere depending on the relative phase accumulations along the arms of the MZI. The phase differences can be created at the arms with plasma dispersion effect or other approaches mentioned in the section 2.1.1. Consequently, the phase shift is transformed into intensity modulation.

2.3.1 Basic Working Principle

The process of intensity modulation can be explained with mathematical terms. Assume an ideal device, which means no insertion loss, and let the electric field at the input be E_i . It is divided into two ($E_{1,2}$) at the input splitter (eq. 2.6). During propagation each field gain a phase depending on the optical path, which is related to the refractive index of the path ($\phi = n \frac{2\pi}{\lambda} L$), and two fields at the output are summed (eq. 2.7).

$$E_1 = E_2 = \frac{E_i}{2} \quad (2.6)$$

$$E_0 = E_1 e^{i\phi_1} + E_2 e^{i\phi_2} \quad (2.7)$$

where $E_{1,2}$, E_0 and $\phi_{1,2}$ are the electric fields in the two arms of the MZI at the input side, output field and phase accumulated along the arms, respectively. The output intensity is the square of the electric field amplitude (eq. 2.8).

$$I_0 = |E_0|^2 = |E_1 e^{i\phi_1} + E_2 e^{i\phi_2}|^2 \quad (2.8)$$

$$I_0 = |E_1 e^{i\phi_1}|^2 + |E_2 e^{i\phi_2}|^2 + E_1^* E_2 e^{-i\phi_1} e^{i\phi_2} + E_1 E_2^* e^{i\phi_1} e^{-i\phi_2} \quad (2.9)$$

where $|E_1 e^{i\phi_1}|^2$ and $|E_2 e^{i\phi_2}|^2$ are the intensities (I_1 and I_2 , respectively) in the arms of MZI at the output side. Then, eq. 2.9 can be rewritten as follow.

$$I_0 = I_1 + I_2 + 2\sqrt{I_1 I_2} \cos\phi \quad (2.10)$$

where ϕ is the phase difference between the waves in two arms of the MZI, which is $\phi = \phi_1 - \phi_2$. This relation is a very well-known general interference equation. It is applicable in all interferometer structures. In a typical MZI, since light beam is splitted into halves, light intensities are equal ($I = I_1 = I_2$). The output intensity becomes $I_0 = 2I(1 + \cos\phi)$. Consequently, the optical intensity at the output is depend on the phase difference between the waves in two arms of the MZI. For instance, when there is no phase difference, which means waves are in-phase ($\phi = 0$), the output intensity becomes maximum. On the other hand, a π radian phase shift is created, waves in the arms becomes out-of-phase and output intensity is minimized. The optical intensity for different phase differences is shown in Fig. 2.4. Switching between no-phase and π -phase cases is transformed into intensity modulation and can be implemented in an integrated photonic system with this process in an MZI.

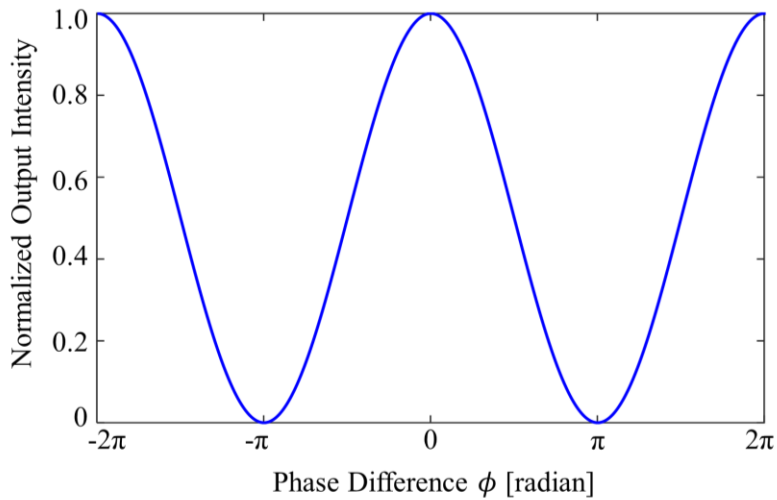


Figure 2.4. Normalized optical intensity at the output for phase difference between the waves in the arms of the MZI. The plot is normalized with $4I$ where I is the light intensity in each arm according to eq. 2.10.

2.3.2 Mach-Zehnder Interferometer Based Modulators

There has been an extensive amount of research on optical modulator based on Mach-Zehnder Interferometer with a phase shifter structures whose operation is based on p-n diode, p-i-n diode or MOS structures. A representative MZI-based modulator with silicon waveguide (Fig. 2.5-a) and with various structures from the literature [41,52] are shown in Fig. 2.5. The required phase shift is generated via such semiconductor devices according to the plasma dispersion effect (See eq. 2.4 and eq. 2.5). These modulators can reach up to 50 Gb/s [41-51]. On the other hand, phase shifter length is also an important specification. These structures require long phase shifter since the operation of the devices relies on the relative phase accumulation. For example, among all these devices [41-51] the shortest interaction length is reported by Terada, Y. et al. [41], Hinakura, Y. et al. [44] and Terada, Y. et al. [45] as 200 μm . Another important concern in optical modulators is the power consumption, which is associated with the operation voltage. In order to generate a high enough relative phase between the arms of the MZI, operation voltage values used in the literature are around 3V_{PP}. The lowest voltage swing for a proper intensity modulation in MZI among many optical modulators reported [41-51] is 1.75V with the DC offset of -0.9V [41,44]. In

order to optimize the modulator and increase its performance, there are various structures and optical components have been used. Photonic crystals (PhCs) are one of such devices used in the arms of the MZIs as a phase shifter. They are artificial structures composed of dielectric materials which are periodically ordered along the optical axis [53]. Beside other optical behaviors that they have provided for the optical system, one of the most interesting and common in MZI based optical modulators is the slow light phenomenon. It is the concept of lowering the group velocity of the light [54-56]. Since PhCs are capable of manipulating the light according to the purpose of the associated optical system, slow light concept is exploited via PhCs in MZIs. Such integration has provided higher performance and smaller device footprint on modulators [41, 44, 45, 52, 54-58]. In this thesis, among such devices, we focused on the one [44] with the smallest phase shifter, which is 80 μ m-length with operation voltage of 2V for 1 Gb/s switching speed. The representative structure of the device is shown in Fig. 2.5-b. Flexibility to control the light behavior propagating through PhC has been provided another promising concept, which is negative refractive index [59]. This phenomenon is related to several extraordinary optical properties such as super-focusing [60,61], inverse Doppler effect and Snell's Law [62,63]. It has been also exploited to obtain near-zero-refractive index by compensating the positive refractive index [64,65]. Negative refractive index phenomenon has an important role in this thesis. Therefore, it was examined in detail in proceeding sections.

The carrier injection/accumulation processes can also be performed in a differential way [41]. In other words, two p-i-n or p-n diode structure can be used in phase modulation step in MZIs rather than one (Fig. 2.5-c) and the electrical signal driving these diodes are given differentially, which is called pull-push drive. This method provides higher phase difference $\Delta\phi$ for the same interaction path or the same $\Delta\phi$ with shorter phase shifter length and same operation voltage. For a simple MZI system, the energy consumption per bit (W_{bit}) can be expressed as $CV_{pp}^2/4$ [66]. On the other hand, MZI system with pull-push drive consumes the energy of $CV_{pp}^2/2$ per bit. This means that although pull-push drive reduces the optical interaction path and device area on an integrated chip, it doubles the energy consumption.

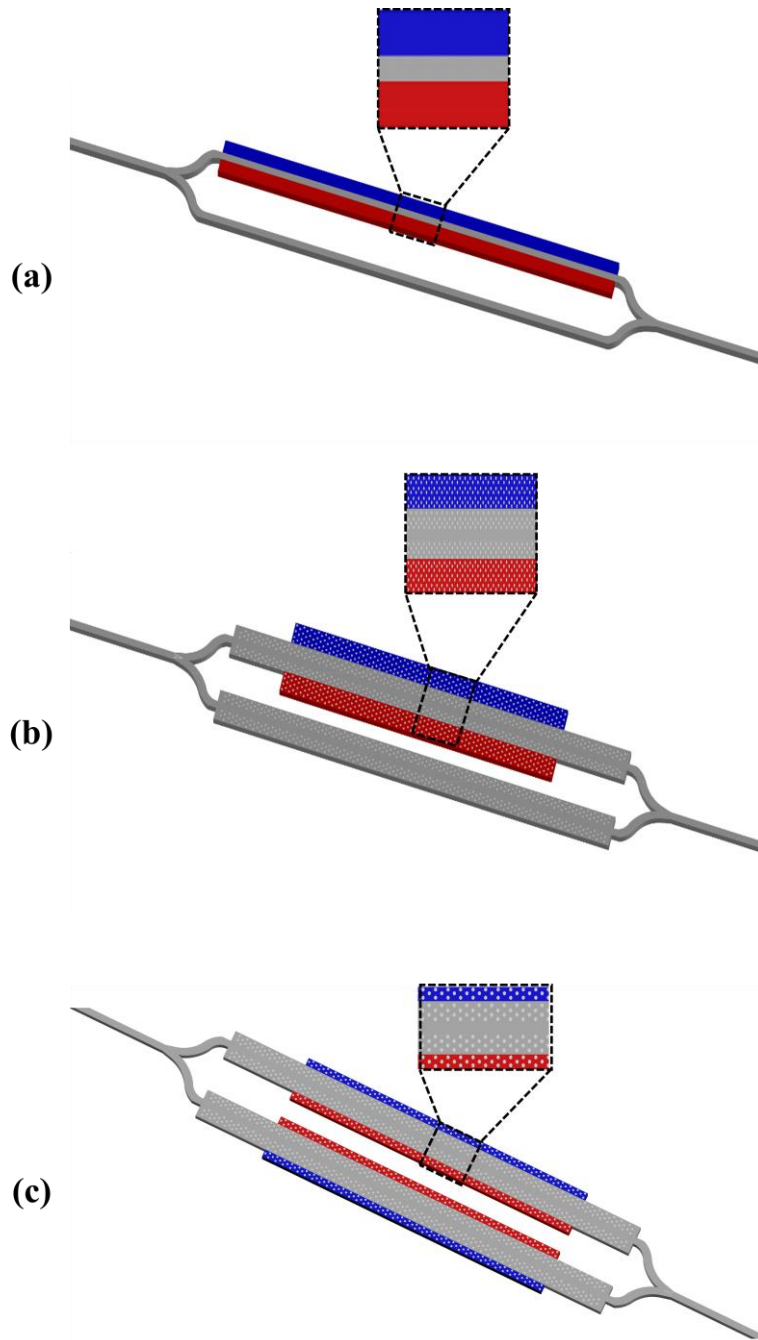


Figure 2.5. MZI based optical modulator structures. P-type and n-type doped regions are represented with blue and red color. (a) Mach-Zehnder Interferometer with p-i-n diode structure whose intrinsic region is simple silicon waveguide as a phase shifter. (b) MZI with photonic crystal waveguide on both arms. The phase modulation is performed via plasma dispersion effect with a p-i-n diode on one arm which an electrical signal is applied to. The length of the phase shifter is $80\mu\text{m}$ and operation speed is 1 Gb/s [44] (c) MZI with photonic crystal waveguide and pull-push drive on both arms. The phase shifter length is $200\mu\text{m}$ for the speed of 32 Gb/s [41]. *Plots are not drawn to scale.*

2.4 Ring Resonators

The Mach-Zehnder Interferometer is not the only common device for the transformation of phase modulation into intensity modulation. Resonance based optical modulators are also commonly used structures in intensity modulation. Among other resonance structures, ring resonators are at forefront for integrated photonic systems.

The simplest form of a ring resonator is composed of a ring and a waveguide, which is shown in Fig. 2.6. The ring is actually constructed by connecting the output of a directional coupler to its input. The incoming light beam is coupled to that ring and propagates part of the light in the ring. After completing the loop of the ring, coupled signal is coupled one more time with the waveguide. The overall output signal of the device depends on the resonance conditions, which is associated with the effective refractive index of the ring, radius of the ring, coupling coefficients and power attenuation coefficient (loss) of the optical path (both ring and waveguide) [67]. Simple ring resonator is also called all-pass filter (APF) or notch filter (NF) due to its optical behavior for several specific cases. When some conditions are satisfied, a ring resonator provides zero transmission for the optical signal at resonant wavelength.

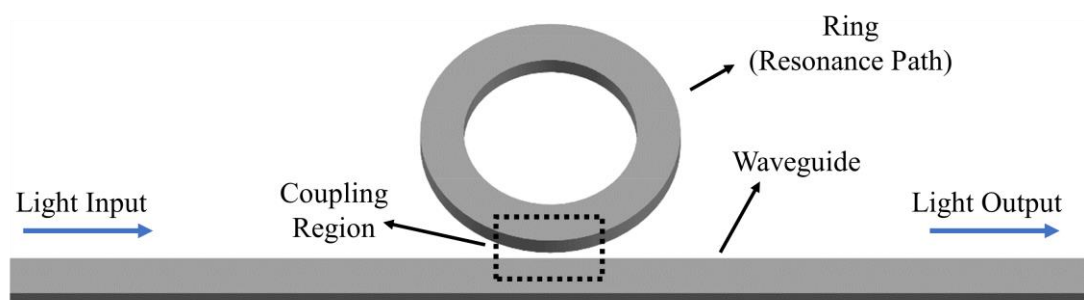


Figure 2.6. Basic structure of a ring resonator

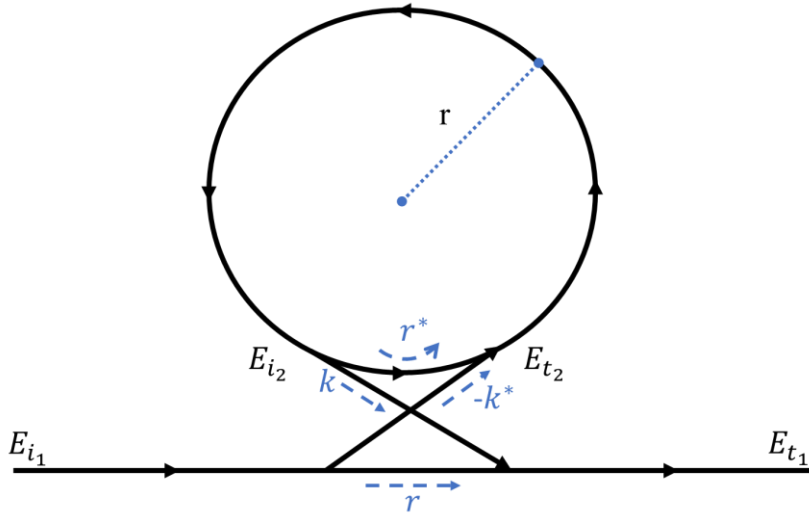


Figure 2.7. Model of a ring resonator composed of a single waveguide and a ring with radius of r . The incident and transmitted electric field vectors are represented with E_{i1} , E_{i2} , E_{t1} and E_{t2} . r and k are the self-coupling and cross-coupling coefficients, respectively. The notation “ $*$ ” denotes the conjugated complex values of coupling coefficients.

2.4.1 Basic Working Principle

The basic spectral behavior of a simple ring resonator can be derived by assuming that input is a continuous wave and by matching the fields in the coupling region [67,68]. The model of the resonator is shown in Fig. 2.7. Considering that a ring resonator with radius r is excited, there is no loss in the coupling, other losses in the device is constant which means attenuation of the fields is constant during the propagation and single polarization is available in the device, the relation between the fields can be expressed as the matrix given in eq. 2.11 as follows.

$$\begin{bmatrix} E_{t1} \\ E_{t2} \end{bmatrix} = \begin{bmatrix} r & k \\ -k^* & r^* \end{bmatrix} \begin{bmatrix} E_{i1} \\ E_{i2} \end{bmatrix} \quad (2.11)$$

The electric fields are defined as complex values and coupling coefficients r and k are determined with the coupling mechanism of the device.

Since the coupling loss is neglected and the system is reciprocal, the equality of $|k|^2 + |r|^2 = 1$ is valid. Also, for the sake of simplicity, we can assume that incident field E_{i_1} is equal to 1. Then, the relation between the fields around the ring is given in eq. 2.12.

$$E_{i_2} = \alpha \cdot e^{i\phi} \cdot E_{t_2} \quad (2.12)$$

where α and ϕ are the loss coefficient and the phase accumulated along the ring, respectively. As stated before, phase is $\phi = \frac{2\pi}{\lambda} n_{eff} L$ where L is the optical path. Here, the optical path is the circumference of the ring, which means $L = 2\pi r$. Then the phase accumulated along the ring is given by eq. 2.13.

$$\phi = \frac{2\pi}{\lambda} \cdot n_{eff} \cdot L = \frac{2\pi}{\lambda} \cdot n_{eff} \cdot 2\pi r \quad (2.13)$$

After the matrix in eq. 2.11 is solved with eq. 2.12 and eq. 2.13, the incident and transmitted fields can be obtained as given in eq. 2.14, 2.15 and 2.16. Note that it is assumed that $E_{i_1} = 1$. The ratio of input and the output fields is given in eq. 2.17.

$$E_{t_1} = \frac{r \cdot e^{-i\phi} - \alpha}{e^{-i\phi} - \alpha \cdot r^*} \quad (2.14)$$

$$E_{i_2} = \frac{-\alpha \cdot k^*}{e^{-i\phi} - \alpha \cdot r^*} \quad (2.15)$$

$$E_{t_2} = \frac{r \cdot e^{-i\phi} - \alpha}{-e^{-i\phi} \cdot \alpha \cdot r^* + 1} \quad (2.16)$$

$$\frac{E_{output}}{E_{input}} = E_{t_1} = \frac{r \cdot e^{-i\phi} - \alpha}{e^{-i\phi} - \alpha \cdot r^*} \quad (2.17)$$

By taking square of the eq. 2.17, we can obtain the intensity transmission T as provided in eq. 2.18.

$$T = \left| \frac{E_{output}}{E_{input}} \right|^2 = \frac{\alpha^2 - 2 \cdot r \cdot \alpha \cdot \cos\phi + r^2}{r^2 \cdot \alpha^2 - 2 \cdot \alpha \cdot r \cdot \cos\phi + 1} \quad (2.18)$$

The resonance state occurs when the phase is the multiple of 2π . Therefore, the resonance condition is as given in eq. 2.19.

$$\phi = 2\pi \cdot m \Rightarrow \lambda_{res} = \frac{2 \cdot \pi \cdot r}{m} \cdot n_{eff} \quad (2.19)$$

where n_{eff} is the effective refractive index of the medium and m is a positive integer number. There is a special case called critical coupling at which the internal loss in ring is equal to the coupled power ($\alpha = |r|$). Under critical coupling case, the transmission of the light becomes zero according to eq. 2.18 at resonance wavelengths ($\phi = 0$). The transmission of the light changes periodically and vanishes at multiples of resonance wavelength (Fig. 2.8).

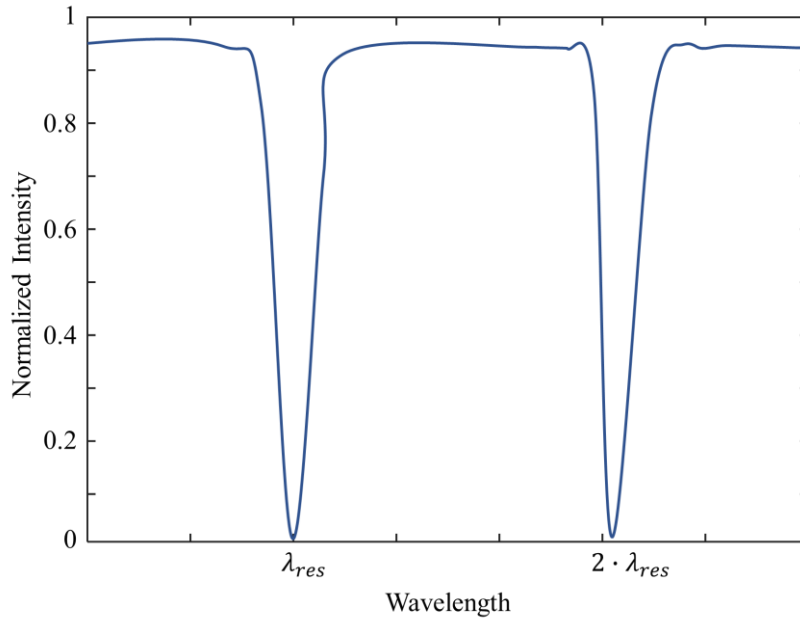


Figure 2.8. Representative spectral normalized intensity of a single ring resonator

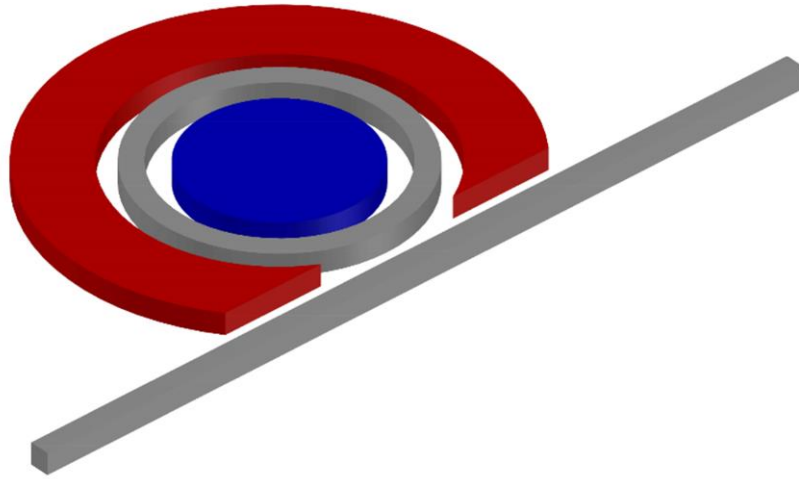


Figure 2.9. Schematic structure of a ring resonator based optical modulator [69,75] with p-i-n structure. Red and blue represent the n-type doped and p-type doped silicon regions, respectively.

2.4.2 Ring Resonator Based Modulators

The ring resonators are sensitive to the optical circumference of the ring and the wavelength of the incoming light beam as mentioned in the previous section. Such property has been used for the purpose of the light modulation [69-78]. In other words, like other optical modulators, the variation in refractive index of the optical medium with applied electrical signal has been used to change the resonance condition of the ring resonator, which leads to shift of the resonance wavelength with varying electrical signal (Fig. 2.10). The control of refractive index can be performed with accumulation, depletion or injection of free carriers via p-n, p-i-n or MOS structures (Fig. 2.9), which is based on the plasma dispersion effect as in the case of MZI-based optical modulators. High operation speeds like 50 Gb/s has been reported [69-78]. Such devices have a ring radius of around 5 μm and requires 2V voltage swing for a proper intensity modulation [70,77]. Since this type of modulators have strong light confinement due to ring, their power consumption and footprint on an optical chip is low compared to MZI-based modulators. On the other hand, they have high sensitivity to fabrication tolerance and variations in temperature due to the low operation bandwidth, which is around 0.1nm in general [77].

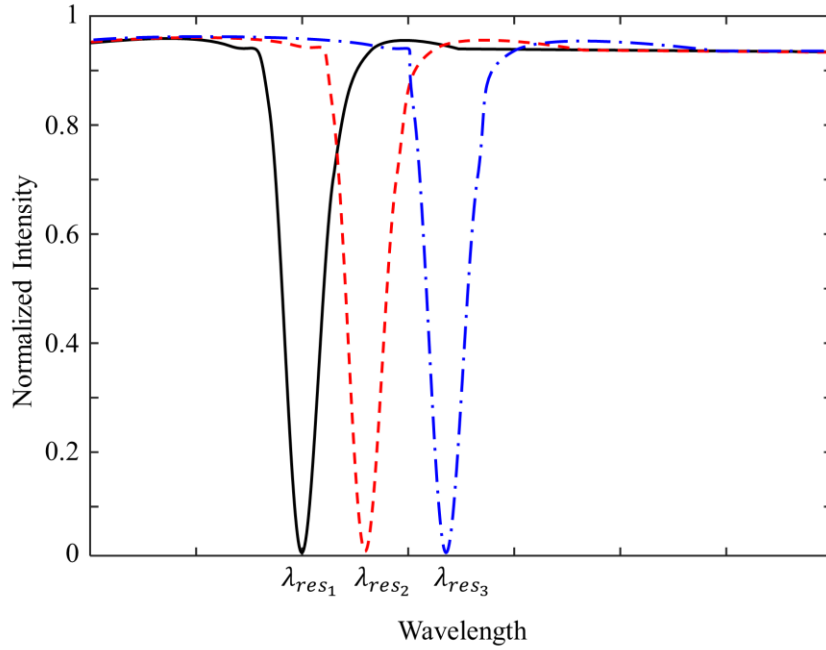


Figure 2.10. Representative spectral intensity of a single ring resonator for different resonance conditions. Each color represents a different amplitude of an electrical signal, which means various refractive indices [69].

2.5 Figure of Merits

There are several figures of merits used for characterization of an optical modulator. The leading ones are operation speed (or switching speed), modulation depth, optical bandwidth, area covered on an integrated chip (footprint), operational wavelength range, power consumption and optical insertion loss.

Modulation speed, which is one of the most important character for a modulator, is defined as the frequency value which the modulation is dropped to half of its maximum level. It is associated with the maximum information carried per second. As stated in previous sections, it was reported that both MZI based and ring resonator based optical modulators can reach up to high operation speeds (~50 Gb/s) [41-51, 69-78].

Modulation depth is the ratio of the maximum light intensity (on-state of the modulator) to minimum light intensity (off-state of the modulator), which is the intensity contrast that an optical modulator relies on ($\frac{I_{max}}{I_{min}}$). It is also known as

extinction ratio. It is better to have a high extinction ratio since it increases the received signal sensitivity and bit error rates [29].

With the developments on integrated optics, placing various optical components on an optical chip has taken more attention day by day. Therefore, footprint of optical modulator is another important specification. As mentioned in section 2.3.2, MZI based modulators requires long phase shifters, which leads to large device area. On the other hand, footprint of ring-based resonators is smaller than that of MZI based ones.

Optical bandwidth range refers to the optical wavelength interval at which an optical modulator works. It is directly connected to the number of optical channels modulated in the device at the same time. In other words, the larger the optical bandwidth is, the more optical signal is modulated at the same system. This results in a larger optical switching speed [79], which will be also mentioned in section 5.2. In the case of bandwidth range, ring-based resonators are disadvantageous compared to their MZI based counterparts due to their narrower bandwidth.

Power consumption is another important characteristic for an optical modulator. It is generally referred to energy per bit for modulators. Although it has several contributors, dc power consumption and dynamic consumption are the leading ones. The electrical side of modulators such as diodes is the source of these consumptions. The first one comes from the electrical resistance of the diode and current passing through the diode during each states of the modulator ($\frac{V_{DD}^2}{R}$). Thus, biasing voltage for modulation is directly related to the dc power consumption. The second contributor of power consumption is associated with the capacitance of diode structures in modulators. energy dissipation during transition from one state to another is affected by how carriers are injected to the corresponding region and how much charge is accumulated in the diode capacitor at transition. Moreover, capacitance of diodes determines the switching speed of the modulator.

Optical insertion loss is the optical power lost due to an optical modulator when it is added to a photonic integrated circuit. It is a passive loss and contains the loss from reflection, absorption and coupling losses. For a MZI based modulator, depending on the length of the device, it is important figure of merit. Thus, reducing the device size is effective on reducing the insertion loss. On the other hand, although the interaction

length in ring-based resonators is shorter than that in MZI based modulators, coupling losses and absorption losses are dominant in ring-based modulator.

Consequently, MZI based and ring resonator based optical modulators provides various improvements, but each type of modulator has different negative aspects. In other words, there is a trade off between specifications. In this thesis, the purpose is to combine advantages of these modulators. The proposed modulator design is a MZI with a phase shifter composed of a photonic crystal (PhC) in the intrinsic region of a p-i-n diode structure. Like previously reported designs, it relies on plasma dispersion effect in order to control the refractive index of the optical medium. However, the aim is to change the refractive index of the silicon for the purpose of photonic band-to-band transition, which leads to much more effective index variation. In fact, the ability of PhCs to provide both positive and negative effective refractive index is used for the modulation purposes [80]. Thus, small phase shifter length and low operation voltage values are obtained in this thesis.

CHAPTER 3

PHOTONIC CRYSTALS

Photonic crystal is one of the most promising structures in integrated photonic systems due to their high integrability with other optical components, small sizes and compact constructions [81-83]. They are composed of dielectric materials periodically arranged such that periodicity of the materials is comparable with the wavelength of light. As in the case of control of electrons in solid state, photonic crystals are able to manipulate the light as a consequence of such periodicity. Just like band diagrams in solid states, photonic crystals are designed in order to control light and generate photonic bands, which is directly related to the light supported in the PhC. The intervals at which light is forbidden are called photonic bandgap [84]. Depending on the dimension of the periodicity, PhCs can be classified. One-dimensional PhCs are also known as Distributed Bragg reflectors (DBR) and they are dielectric stacks. They are mostly used for the reflection purposes (mirrors) and take important role in vertical cavity surface emitting lasers (VCSELs) [85]. If the periodicity is in two dimension, then we have a 2D PhC. Such structures are assumed to have infinite dimension in the direction perpendicular to the plane at which periodicity is available. Thus, they are not physically eligible. However, photonic crystal slab structures were proposed in order to actualize and implement in photonic applications. In fact, PhC slabs are 2D PhCs with a finite thickness (Fig. 3.1). When the spatial periodicity is in all three direction, then it is a 3D PhC. This type of PhCs can be fabricated via top-down etching techniques [86].

The PhC slabs are commonly used structures in integrated photonic applications. One of the most obvious reason is that the fabrication of such structures is easy. They

can be fabricated with simple planar fabrication technology used for the fabrication of electronic components. In this thesis, the phase shift in a MZI structure is created via a silicon PhC slab. Thus, in this chapter, we have provided the theory behind PhC slabs, which is also required to understand the numerical calculations and analysis on PhCs, photonic band structure and its optical meaning, and refractive index calculation methods used for the proposed design in this thesis.

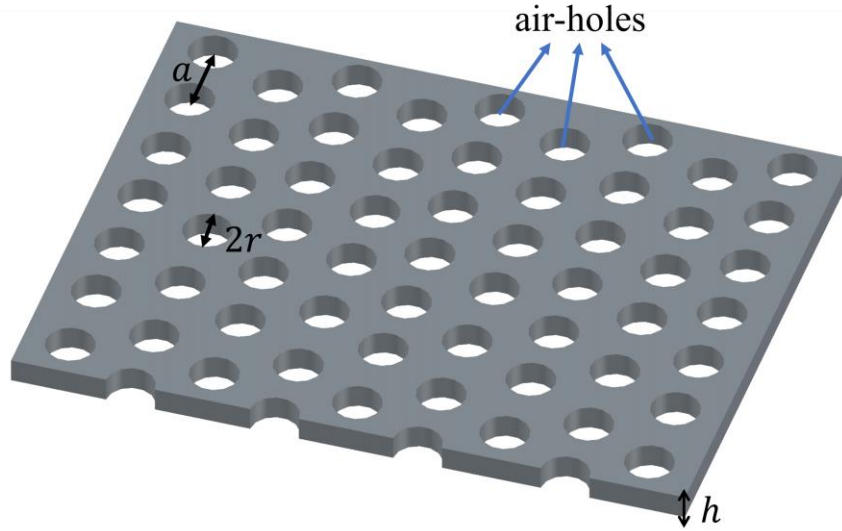


Figure 3.1. Representative schema of a photonic crystal slab composed of an air-hole hexagonal lattice with radius of r , thickness of h and lattice constant of a .

3.1 Theory

The propagation of electromagnetic waves like light in arbitrary mediums is determined by Maxwell equations (eq. 3.1-3.4). This is also valid for the light in PhCs.

$$\nabla \times \mathbf{E} = -\frac{\partial \mathbf{B}}{\partial t} \quad (3.1)$$

$$\nabla \times \mathbf{H} = \mathbf{J} + \frac{\partial \mathbf{D}}{\partial t} \quad (3.2)$$

$$\nabla \cdot \mathbf{B} = 0 \quad (3.3)$$

$$\nabla \cdot \mathbf{D} = \rho \quad (3.4)$$

where \mathbf{E} , \mathbf{H} , \mathbf{B} , \mathbf{D} , \mathbf{J} and ρ represent electric field, magnetic field, magnetic induction field, displacement field, current density and free charge, respectively. Here, we can assume that no free charge or current is available in the medium, and that the medium is homogeneous and time-invariant. Also, the medium is considered as linear and isotropic. Then, the relation between displacement field and electric field can be expressed as given in eq. 3.5. The same is valid for magnetic field and magnetic induction field (eq. 3.6).

$$\mathbf{D}(\mathbf{r}) = \epsilon_0 \epsilon \mathbf{E}(\mathbf{r}) \quad (3.5)$$

$$\mathbf{B}(\mathbf{r}) = \mu_0 \mu \mathbf{H}(\mathbf{r}) \quad (3.6)$$

where ϵ_0 and μ_0 are the permittivity and permeability of the vacuum, respectively. ϵ and μ are relative permittivity and permeability, which are constants depending on isotropic materials. Here, for silicon PhCs we considered relative permeability as $\mu = 1$. Then, eq. 3.3 and eq. 3.4 can be rewritten in terms of \mathbf{H} and \mathbf{E} . For the sake of simplicity, by using the linearity of Maxwell equations, we can separate time and spatial terms of the fields as shown in eq. 3.7 and eq. 3.8.

$$\mathbf{E}(\mathbf{r}, t) = \mathbf{E}(\mathbf{r}) e^{-i\omega t} \quad (3.7)$$

$$\mathbf{H}(\mathbf{r}, t) = \mathbf{H}(\mathbf{r}) e^{-i\omega t} \quad (3.8)$$

Maxwell equations can be decoupled into a single equation, which is named as wave equation (eq. 3.9), by taking the curl ($\nabla \times$) of the eq. 3.2 and substitute it into eq. 3.1. The obtained wave equation is in terms of $\mathbf{H}(\mathbf{r})$. The same equation could be written in $\mathbf{E}(\mathbf{r})$ if we started with eq. 3.1.

$$\nabla \times \frac{1}{\epsilon(\mathbf{r})} \nabla \times \mathbf{H}(\mathbf{r}) = \left(\frac{\omega}{c}\right)^2 \mathbf{H}(\mathbf{r}) \quad (3.9)$$

where, c and ω are speed of light and optical frequency, respectively. Note that the eigenfunctions of the wave equation are $\mathbf{H}(\mathbf{r})$ and the corresponding eigenvalues are $\left(\frac{\omega}{c}\right)^2$. Eq. 3.9 is valid for arbitrary materials under the assumptions stated above. For PhCs, on the other hand, we also have symmetricity. One of them is the discrete translational symmetry, which is invariance of the crystal along one or more than one direction (depending on the dimension of the periodicity) for a lattice vector \mathbf{R} , which is a linear combination of basis vectors. In other words, dielectric profile of a PhC is $\epsilon(\mathbf{r}) = \epsilon(\mathbf{r} + \mathbf{R})$. In a crystal, such repeated spaces are named as unit cells. Moreover, eigenfunctions of eq. 3.9 for periodic medium are the products of a plane wave ($e^{i\mathbf{k}\cdot\mathbf{r}}$) and a periodic function ($\mathbf{u}_k(\mathbf{r})$). This is known as Bloch theorem [87]. The eigenvalues of the product $e^{i\mathbf{k}\cdot\mathbf{r}} \cdot \mathbf{u}_k(\mathbf{r})$ are $\omega_n(\mathbf{k})$ which are functions of wavevector \mathbf{k} . When we substitute this expression into the wave equation, the solutions actually form photonic bands (See Fig. 3.4). Up to this point, all the expressions and solutions are general. In other words, they are valid for all dimensional PhCs. If we restrict ourselves to 2D PhCs, the lattice vector \mathbf{R} is defined as the linear combination of two primitive lattice (basis) vectors (eq. 3.10).

$$\mathbf{R} = m_1\mathbf{a}_1 + m_2\mathbf{a}_2 \quad (3.10)$$

where $m_{1,2}$ and $\mathbf{a}_{1,2}$ are integer numbers and basis vectors for a 2D PhC lattice, respectively. PhCs could be in different periodicity and arrangements of lattices. Each lattice is named as Bravais lattice and there are five lattices for two dimensional PhCs of which most popular ones are hexagonal (Fig. 3.2-a) and square (Fig. 3.2-b) lattices.

A periodic function $f(x)$ in the lattice ($f(x+a) = f(x)$ where “a” is the lattice constant) can be expressed with the summation of exponentials. In other words, the function can be equated to a Fourier series (eq. 3.11).

$$f(x) = \sum_{m=-\infty}^{\infty} A_m e^{iG_m x} \quad (3.11)$$

The periodicity condition is $G_m \alpha = 2\pi m$ and the set of amplitudes is $A_m = \frac{1}{a} \int_0^a f(x) e^{iG_m x} dx$. This relation is one-dimensional. It can be rewritten for two-dimensional lattices as provided in eq. 3.12.

$$f(x + a, y + b) = f(x, y) = \sum_{m_1, m_2 = -\infty}^{\infty} A_{m_1, m_2} e^{i\overrightarrow{G_{m_1 m_2}} \cdot \vec{r}} \quad (3.12)$$

Note that $\overrightarrow{G_{m_1 m_2}}$ represents the reciprocal lattice vector and can be expressed as $m_1 \frac{2\pi}{a} \hat{x} + m_2 \frac{2\pi}{b} \hat{y}$. Also, the basis vectors for reciprocal lattice can be notated as \overrightarrow{g}_i and the relation between a lattice basis vector and reciprocal basis vector is $\overrightarrow{g}_i \cdot \overrightarrow{a}_j = 2\pi \delta_{ij}$. Like regular lattice representation, reciprocal lattice is useful to examine the properties of the periodic structure. The finite repetitive zone in reciprocal space is named as Brillouin zone. Also, this area can be reduced into a minimal space called irreducible Brillouin zone via symmetry operations. Photonic band structures are calculated in this region.

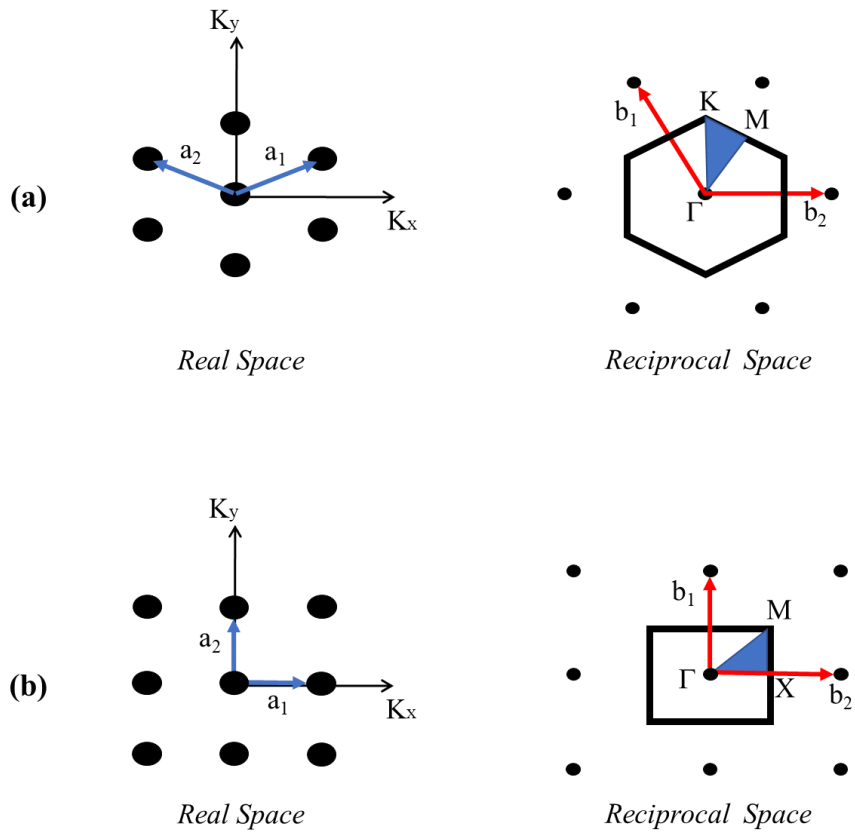


Figure 3.2. Diagrams of hexagonal (triangular) **(a)** and square **(b)** PhC lattices in real and reciprocal spaces. $a_{1,2}$ and $b_{1,2}$ are basis and reciprocal vectors, respectively. Blue shaded areas represent the irreducible Brillouin zones (IBZs).

3.2 Numerical Analysis Methods

3.2.1 Photonic Band Structure

The solutions of Maxwell equations for a PhC are photonic bands and all the bands together form the photonic band diagram, which is also called band structure, of corresponding PhC. Thus, such diagrams give important information regarding optical characteristics of PhCs. For instance, questions like how a light beam propagates through a PhC, how is its optical behavior in a PhC and which optical modes are supported can be answered with the help of band diagrams. Since in this thesis, we focused on designing a PhC with some specific optical properties, photonic band diagrams were studied in detail. The mathematical background of such diagrams was discussed in section 3.1. As stated in that section, each photonic band is actually a band frequency $\omega_{\mathbf{k}}$, which is a function of wave vector \mathbf{k} . These functions are ordered with increasing band numbers for increasing frequency like first photonic band, second photonic band etc. Although infinite number of band is available for PhCs, in practice, the first two bands are studied. The computations on band diagram is performed not in all k-space but along the boundaries of the irreducible Brillouin zone (IBZ) instead because the rest of the k-space is the repetition of IBZ due to the symmetricity of the lattice. The vertical axis of a band diagram is normalized frequency with a unit of $\omega a/2\pi c (= a/\lambda)$. This makes the dimensional scaling of PhCs possible. For this thesis, photonic band diagrams were calculated by using MIT-Photonic-Bands (MPB) software package [88], which is a free software computing eigenfrequencies ($\omega_{\mathbf{k}}$) of Maxwell equations (eq. 3.1-3.4) in dielectric structure with periodicity inside k-space. The unit cell of PhCs is discretized with the resolution of 32 grids per μm . MPB version 1.6.1 was used for all band structure-based calculations on a computer with 64-bit Intel processor of 12 core-threads. (The code used to obtain band diagram is provided in Appendix A.)

3.2.2 Equifrequency Contours

Photonic band diagrams are not the only computation on photonic bands. Equi-frequency contours (EFCs) are also the solutions of Maxwell equations in k-space. The difference is that unlike band diagram, an EFC is calculated along all directions in all points of k-space. It is an important tool for PhC applications since it provides various details regarding PhCs. Propagation in the medium of PhC and refraction between mediums are the leading ones. The behavior of contours for varying optical frequencies ($\omega_{\mathbf{k}}$) gives important ideas about the corresponding PhC [91,92]. For instance, group velocity in a PhC can be obtained from the gradient vector of the contour associated with the frequency at which the PhC operates (eq. 3.13). The group index is the ratio of speed of light to group velocity (eq. 3.14). The phase index is another important optical property one can calculate with the help of EFCs [91]. For the phase accumulation and phase shift calculations, phase index is used as in the case of this thesis. The phase (effective) index calculations with EFCs were explained under the title of “Effective Refractive Index Calculations” in detail (See Section 3.4.3).

$$\mathbf{v}_g = \nabla_{\mathbf{k}}\omega \quad (3.13)$$

$$n_g = c/\mathbf{v}_g \quad (3.14)$$

The EFCs were also obtained via MPB by discretizing the unit cell with $32 \times 32 \times 32$ grid points. The borders of the k-space are determined as $\pm \frac{2\pi}{a}$ for both axes. The k-points between the borders ($-\frac{2\pi}{a} < k_{x,y} < \frac{2\pi}{a}$) create a map and the ones associated with the eigenfrequencies of Maxwell equations form the contours together. Here, the output of MPB simulations were taken as a 100×100 Matrix and was plotted with the help of a plotting software (See Appendix B).

3.2.3 *Electric Field Distribution*

The band diagrams and EFCs provide information based on the plane wave expansion [88]. In other words, light is assumed to be a plane wave and unit cells are expanded infinity in the direction of periodicity. The output of this methods could be related to optical properties of PhC. However, in order to be ensure and obtain more visualized results regarding to effective refractive index of PhCs and slab waveguides, field distributions and profiles can be used. Throughout this thesis, TM-like polarization was exploited. Thus, electric field distribution was focused in this document.

The electric field distribution was obtained with the finite-difference time domain (FDTD) method. It is a very common method for PhC calculations and can be shaped for many different physical structures. The method relies on the discretization of Maxwell equations (eq. 3.1-3.4) in terms of both space and time. Thus, the behavior of fields inside PhCs in time can be observed via this method. The propagation of the fields depends on the effective refractive index of the corresponding medium, which is formalized in Maxwell equation and comes from the wave equation (eq. 3.9). Therefore, in order to calculate effective index and find the phase accumulation inside photonic components, electric field distributions were obtained and examined in several points. For that purpose, MEEP as a computation tool is used. It is free software specialized to solve wave equation via FDTD method [89]. The numerical simulations were performed on MEEP version 1.4.3 with the computation resolution of 24 grid/ μm . The boundary conditions were determined by using perfect matching layers (PMLs) around the PhC slabs. Boundaries along x and z directions were set as $1\mu\text{m}$ -PML and at the remaining boundaries (y-directed) PML was specialized as absorbing layer in order to eliminate the reflected wave-fronts along propagation direction (See Appendix C). The structures examined here are three dimensional and require many grid points to discretize the structures. Thus, in order to reduce the computation time as much as possible, parallel computation package is used (MEEP-MPI) and simulations were performed on 12 core-threads at the same time.

3.3 Photonic Crystal Slab

PhC slabs are the combinations of two-dimensional periodicity of PhCs and the finite thickness of slab waveguides. A PhC slab representation for hexagonal lattice with air-holes is shown in Fig. 3.1. In this thesis, hexagonal lattice (PhC slab) is exploited for the modulation purposes. Note that in the proceeding parts of the text, although phrase “PhC” is used, it refers to the PhC slab.

As a starting point, consider a PhC structure composed of hexagonal lattice with air-holes. The radius of the air-holes and thickness of the silicon slab are determined as $0.3a$ and $0.6a$, respectively. The lattice constant is $a = 0.5\mu\text{m}$. The structure is on SiO_2 layer, which means it is a silicon-on-insulator (SOI) platform. The illustration of this SOI structure is shown in Fig. 3.3. In order to examine the PhC, the band diagram was obtained (Fig. 3.4). As one can observe that only photonic bands under a specific region are physically valid. This is due to the finite thickness of the slab.

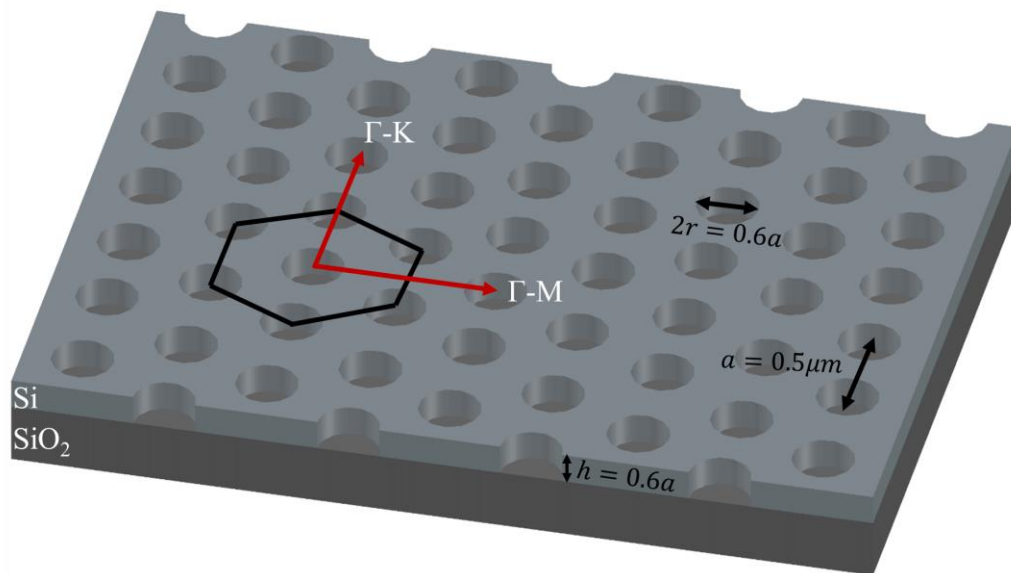


Figure 3.3. PhC slab structure in the form of SOI. It is composed of air-hole based hexagonal lattice and the directions along the lattice are shown on the first Brillouin zone.

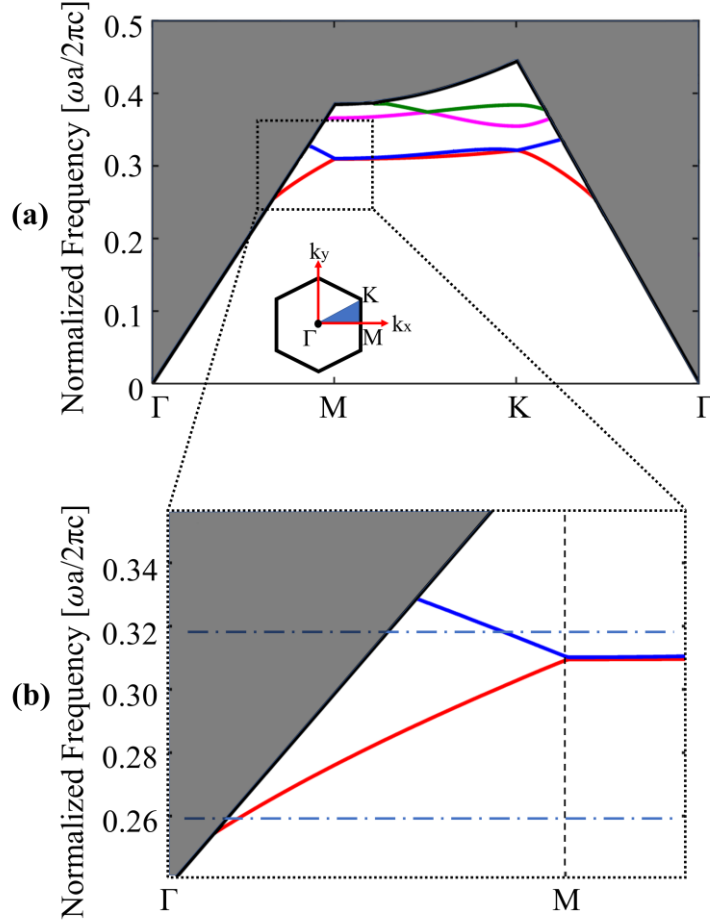


Figure 3.4. (a) Photonic band diagram of the PhC with hexagonal air-hole lattice of radius $0.3a$, thickness $0.6a$ for TM-like polarization. **Inset:** First Brillouin zone and directions on the zone. The blue rectangular represents the Irreducible Brillouin zone. (b) Zoomed view of the band diagram covered via shaded rectangular at (a). The normalized frequencies of 0.26 and 0.32 ($\omega a/2\pi c$) at first two photonic bands are shown with blue horizontal dashed lines. Outside of the light cone is shown as black colored area.

In fact, the localization of the light in PhC slabs is based on the total internal reflection (TIR) in the vertical direction due to the high refractive index contrast between slab and the environment of the slab. On the other hand, in the lateral direction (along the plane of periodicity), light confinement is controlled by the Distributed Bragg reflection (DBR). Thus, light beams with smaller angle than the critical total reflection angle cannot couple to PhC and escape. In order to take into account this loss in band structure analyses, the concept of light cone is used. In the band diagram

given in Fig. 3.4, black area represents the outside of the light cone. There is also another important concept called photonic band gaps. These are the regions where no photonic band is available and no light is supported by the PhC.

Here, we focused on the first and second photonic bands (Fig. 3.4-b). As stated before, band structures provide important information about PhCs. One can observe that the slopes of the first two bands are different along the Γ -M direction. There is a direct relation between the band slope and the refraction of the light [90]. In other words, both the polarity and the magnitude of the slope determines the effective refractive index of the PhC at the operation wavelength. For instance, for the optical wavelengths at the first (second) band along Γ -M, effective-phase index is positive (negative).

3.4 Effective Refractive Index Calculations

One of the most important optical features is the refractive index of a material. The structure here is a three-dimensional PhC slab whose transverse boundaries are air and SO_2 (See Fig. 3.3). Thus, in order to take into account the effects of the geometrical shape and the periodicity of air-holes and silicon material, effective refractive index is calculated. For instance, the refractive index of silicon, silicon dioxide and air are 3.48, 1.5 and 1 at $1.55\mu\text{m}$, respectively. However, the index of the overall structure is quite different as will be seen in proceeding sections. It is directly related to how light gains phase along the same medium (section 3.4.1), how light refracts when it changes its medium (section 3.4.2) and how the wave vector reacts varying optical frequency values (section 3.4.3). Thus, by using each relation, we can reach to effective refractive index of a PhC slab.

3.4.1 Field Distribution

Propagation of a light beam along a medium changes the phase of the light along the path depending on the refractive index of the medium. In other words, phase of the light is proportional to the effective refractive index. This relation is provided in eq. 3.15.

$$\Delta\phi = \left(\frac{2\pi}{\lambda}\Delta d\right)n_{eff} \quad (3.15)$$

where Δd and λ are the distance that light propagate and wavelength of the light, respectively. According to that relation, effective index can be calculated from the change of phase. For that purpose, a continuous plane wave is inserted to the PhC slab mentioned in section 3.3. Two different optical frequencies were examined. These are the normalized frequencies of 0.26 ($\omega a/2\pi c$) and 0.32 ($\omega a/2\pi c$), which are at first and second photonic bands, respectively. Both frequencies were emphasized on the band diagram in Fig. 3.4. The PhC slab length was determined as $14\mu\text{m}$. The electric field profile inside the medium is sinusoidal (Fig. 3.5). This means that the period of the sine corresponds to a phase of 2π radian. Then, by counting the consecutive peaks along a specific distance ($4.4\mu\text{m}$), accumulated phase values were determined as 21.74π radian for 0.26 ($\omega a/2\pi c$) and 32.6π radian for 0.32 ($\omega a/2\pi c$), which corresponds to effective indices of 1.68 and 2.05, respectively. Note that the sign of the indices was not directly induced from the field distribution but one can interpret the index at 0.32 ($\omega a/2\pi c$) as -2.05 with the help of band diagram (Fig. 3.4). The polarity of effective refractive indices will be much clearer in proceeding subsections.

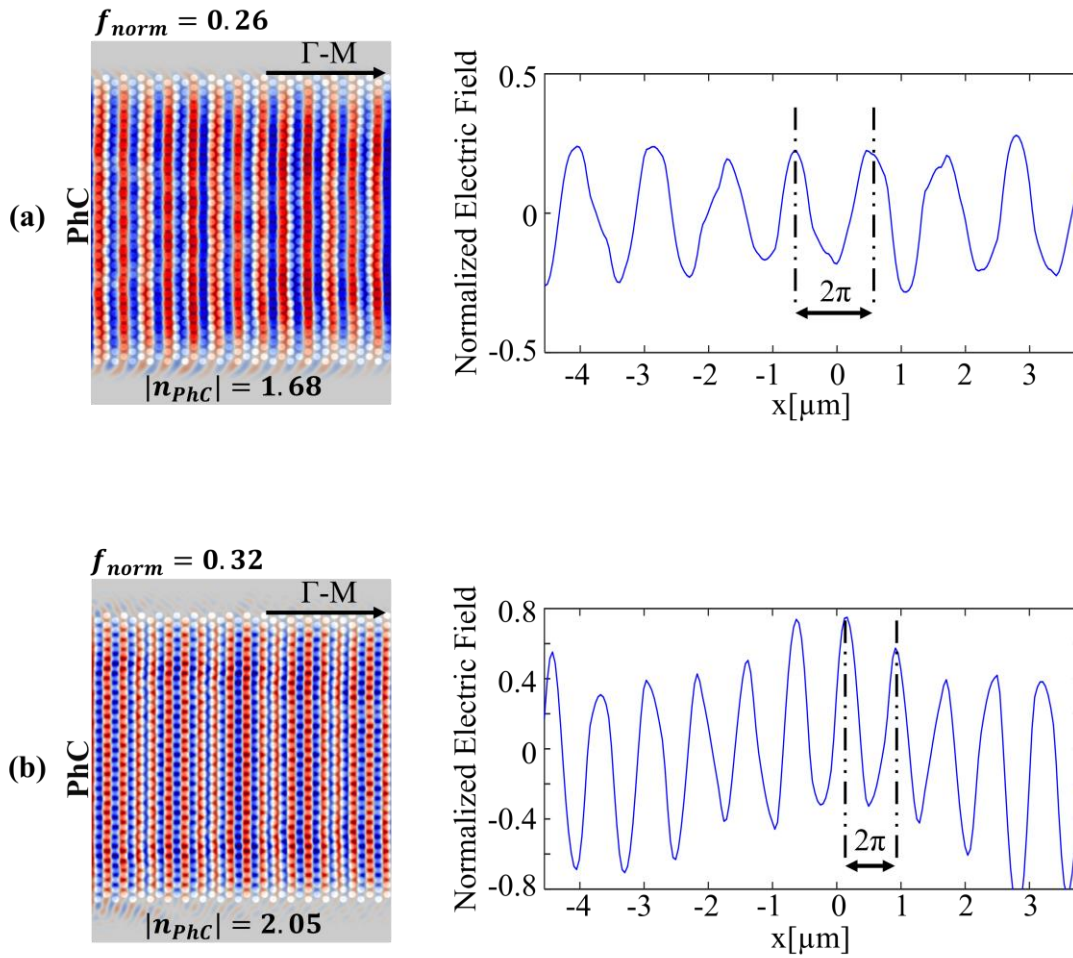


Figure 3.5. (a) Electric field distribution (left) along the PhC slab with hexagonal lattice on oxide ($r=0.3a$, $h=0.6a$, $a=0.5\mu\text{m}$) at the normalized frequency of 0.26 ($\omega a/2\pi c$) and the amplitude profile of the corresponding PhC (right) along the Γ -M direction. The effective index of the structure is calculated as $|n_{eff}| = 1.68$ from field profile. (b) Field distribution (left) and the amplitude profile (right) for the same PhC slab at 0.32 ($\omega a/2\pi c$). Effective index at this frequency is $|n_{eff}| = 2.05$.

3.4.2 Snell's Law

Among all the paths it can follow, light prefers the one that takes the least time. This is known as Fermat's principle and explains reflection at mirrors, refraction of the light at the boundary between different media, and total internal reflection. For that matter, according to Fermat's principle, during reflection the angle of incidence and reflection are equal to each other. Another rule is about the refraction which is also called Snell's Law. There is a relation between the angles of incident/refracted light

rays and the refractive indices of the mediums as provided in eq. 3.16 and its illustration is given in Fig. 3.6.

$$n_1 \cdot \sin(\theta_1) = n_2 \cdot \sin(\theta_2) \quad (3.16)$$

where $n_{1,2}$ and $\theta_{1,2}$ are the refractive indices of the mediums and the angles between incident/refracted light beams and the line normal to the boundary.

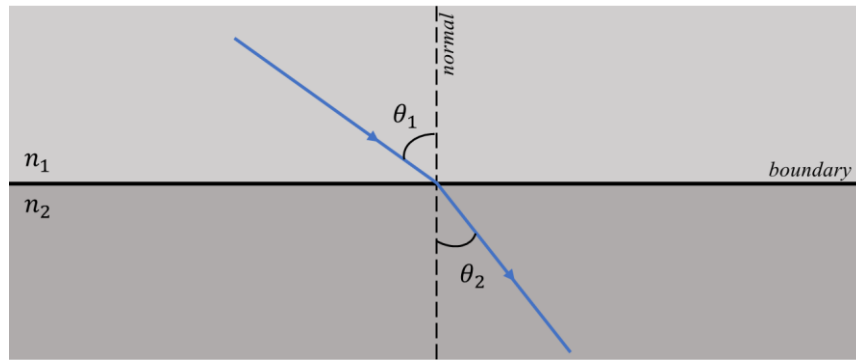


Figure 3.6. Schematic representation of the light refraction at the boundary of two different medium with refractive indices of n_1 and n_2 . The refraction is occurred according to Fermat's Principle and explained with Snell's Law (eq. 3.16).

The propagation inside the PhC under examination here is obtained via FDTD method (See Appendix D). In order to use the Snell's law, the PhC is tilted so that incidence angle is 25° . The propagation (Fig. 3.7) was observed for the two frequency values in the previous subsection. One can see the difference between the positive and negative indices in Fig. 3.7. At the frequency on the first photonic band, light refracts in the way we are used to. On the other hand, at the other frequency, the side of the refracted beam is the same as the incoming light. When Snell's law (eq. 3.16) was applied to the incidence and refraction angles, the effective indices were found as 1.41 at $0.26 (\omega a/2\pi c)$ and -1.25 at $0.32 (\omega a/2\pi c)$. Note that in eq. 3.16, the index of the first medium (n_1) was taken as 2.54, which is the effective index of the asymmetrical Si waveguide calculated by using the effective index method [65].

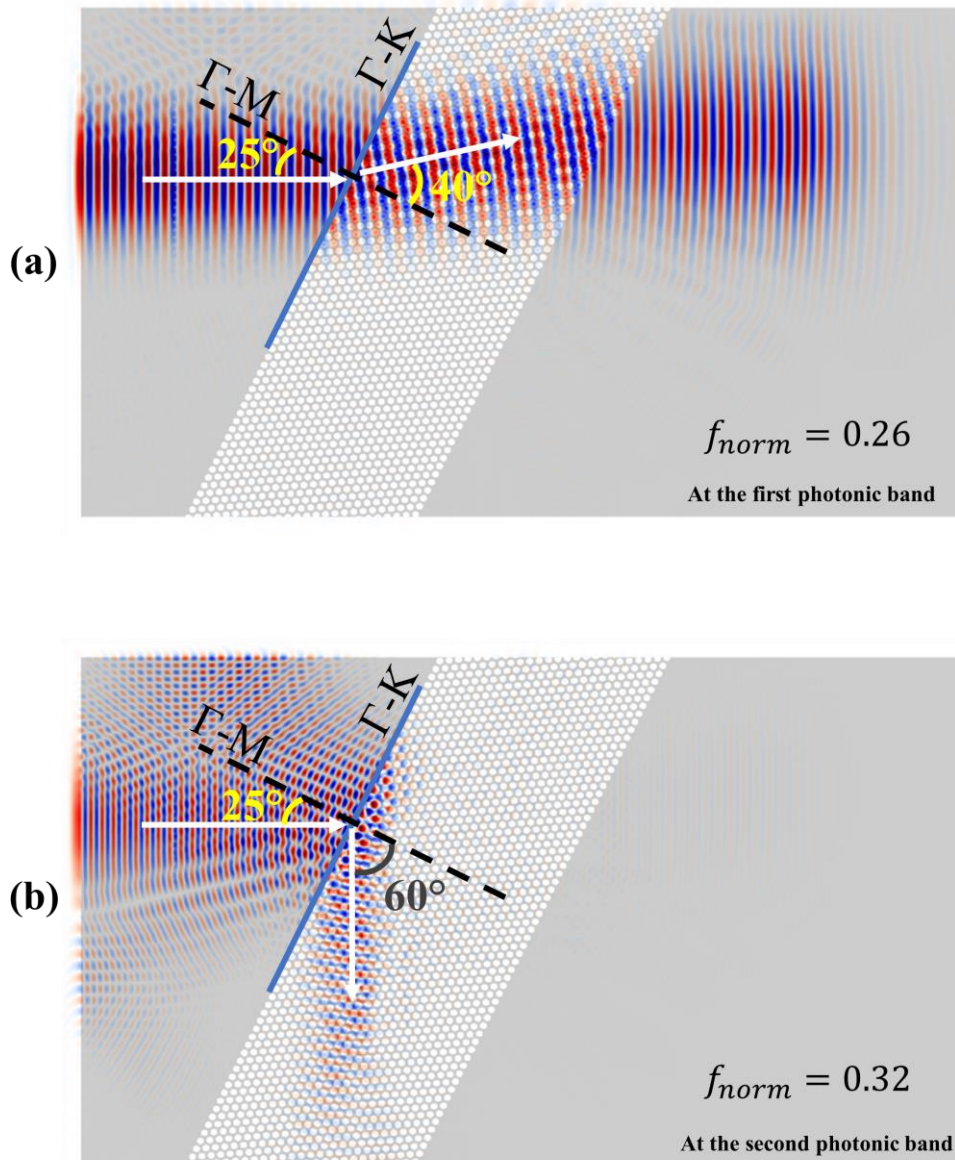


Figure 3.7. The propagation in PhC obtained via FDTD method for the incoming light with the frequencies of (a) 0.26 ($\omega a/2\pi c$) and (b) 0.32 ($\omega a/2\pi c$). The incidence angle is 25° for both cases and the refraction angles are 40° and 60° , respectively. The refraction direction is reverse at (b) due to the negative refraction (See Fig. 3.4-b).

3.4.3 EFCs

Equi-frequency contours like band structures are important tools for analysis of PhCs. As stated before, various optical properties can be obtained from such diagrams. One of them is effective index. The relation between effective (phase) refractive index and the contours is given in eq. 3.17. The wavenumber ($|k|$) of light inside a PhC is represented via the radius of the corresponding contour [91].

$$r_{contour} = \omega \cdot n_{eff} \quad (3.17)$$

where $r_{contour}$, ω and n_{eff} represent radius of the contour associated with the optical wavelength, normalized frequency and effective (phase) index of the PhC at that frequency, respectively. The amplitude of the index can be calculated via eq. 3.17. The sign of the index, on the other hand, is related to the behavior of consequential contours for varying frequency. This is explained with the relative directions of the group velocity (\mathbf{v}_g) and the wave vector (\mathbf{k}) as illustrated in Fig. 3.8. If the contours move outward, which means direction of \mathbf{v}_g is towards outside, with increasing normalized frequency, then the effective index is positive (Fig. 3.8-a). On the other hand, if the direction of contours is reverse with increasing frequency, then one can conclude that the index is negative (Fig. 3.8-b). Thus, the first and second photonic bands are associated with positive and negative refractive indices, respectively [64,91]. Moreover, the shape of EFCs is related to several optical properties. Here, contours for the first band (Fig. 3.8-a) are circular for all frequencies. However, at the other band shape of the contours becomes nonuniform (Fig. 3.8-b). This means that while operating at the first band, the refractive index is the same for all incidence angle (i.e. uniform), but the refractive index depends on the direction of the incoming light at the second band (i.e. nonuniform). Thus, there would be differences in the index values calculated via EFCs and other methods mentioned especially for the second band.

The refractive index of the PhC slab here is calculated via EFCs as 1.61 and -1.63 at 0.26 and 0.32 ($\omega a/2\pi c$), respectively. For the design of a phase shifter this method was used as will be mentioned later.

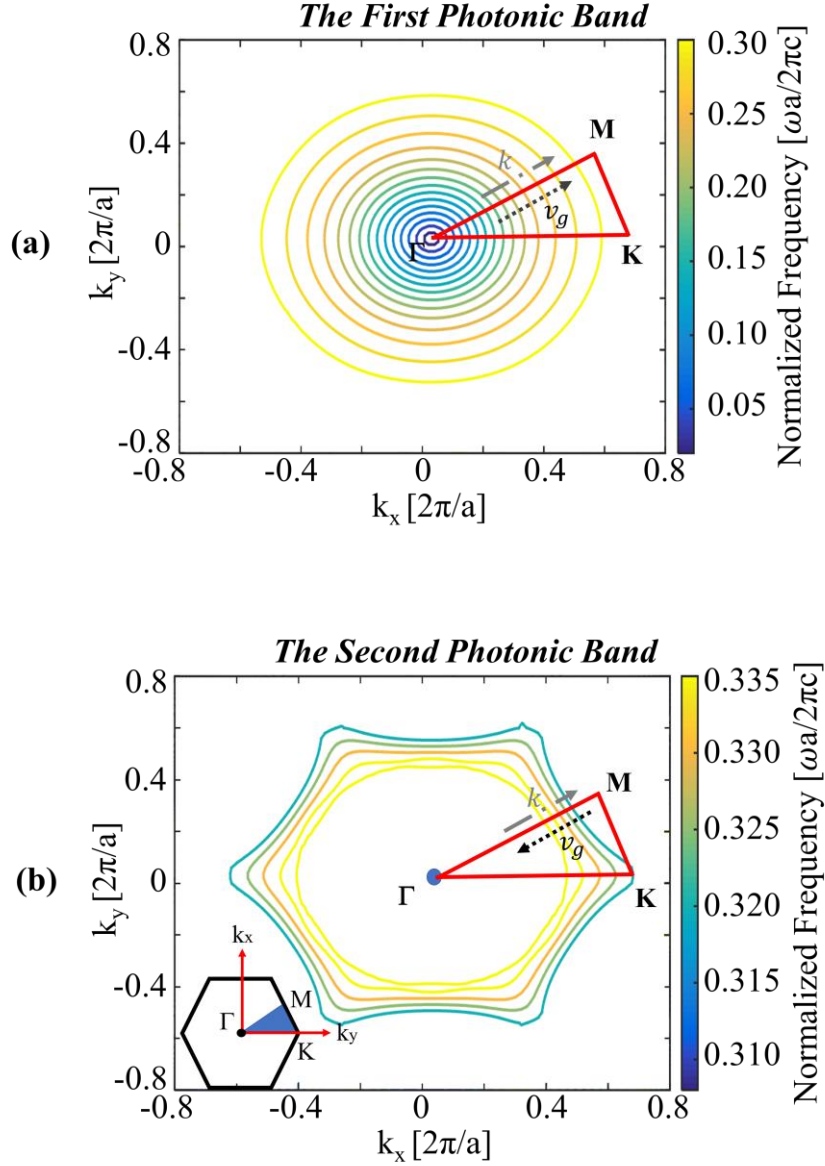


Figure 3.8. The EFC plots for the PhC slab of hexagonal lattice with air-holes (radius of $r = 0.3a$, thickness of $h = 0.6a$ where lattice constant is $a = 0.5\mu m$) for the frequencies at the (a) first and (b) second photonic bands. The area covered by red lines represents the irreducible Brillouin zone (IBZ). The group velocity (\mathbf{v}_g - dashed black line) and wavevectors (\mathbf{k} - dot-solid gray line) are shown with arrows on the direction of Γ -M. Note that frequencies outside the light cone were excluded from plots. **Inset:** The first Brillouin zone of the hexagonal lattice and the IBZ (blue rectangle)

CHAPTER 4

PHOTONIC BAND-TO-BAND TRANSITION BASED OPTICAL MODULATOR

In the previous chapter, the effective index of a PhC can be calculated with different methods. Although the results of each method are slightly different, one point is valid for all of them. Different photonic bands are associated with distinct effective indices in terms of both amplitude and sign. For instance, according to the results of EFCs (Section 3.4.3) for the PhC slab, there is a difference of 0.02 in the amplitude of effective indices. Also, since the first and second bands are related to opposite polarities for index, the shift in indices from one band to another becomes huge. Such a high index variation means a high phase shift (eq. 3.15) which can be utilized in a Mach-Zehnder interferometer for different switching states of a modulator.

As stated in section 2.1.4, refractive index variations in silicon due to applied electric field is not high enough to be used for modulation purposes. Therefore, plasma dispersion effect as a different approach, which relies on the carrier concentration in silicon, is more common in silicon photonics. For example, in order to create refractive index change of 0.01 in a silicon bulk at 1.55 μm -wavelength, one needs a free carrier injection with the concentration of $0.41 \times 10^{19} \text{ cm}^{-3}$ to the medium (both hole and electron) according to Soraf and Bennet [36] (eq. 2.4). If we used a simple silicon bulk for modulation in a MZI, then we would require to have a nearly 78 μm -phase shifter silicon waveguide, which is the minimum length, for a proper modulation (π radian phase shift between on and off states of the modulator). As mentioned before, there are various MZI-based modulator designs relying on different concepts such as slow light on PhCs. This could increase the performance of the modulator and reduce the

length of the phase shifter. For instance, one of such designs has relatively short phase shifter ($80\ \mu\text{m}$) and comparable operation speed ($1\ \text{Gb/s}$) [44].

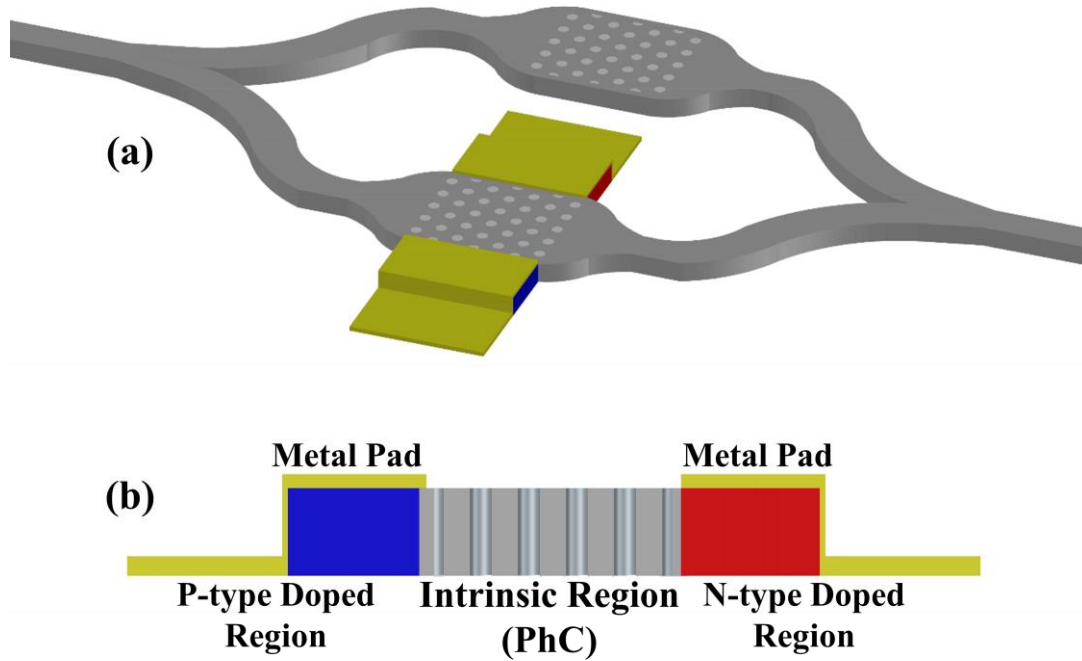


Figure 4.1. (a) The illustration of the proposed design which is a MZI-based optical modulator. The arms ($\sim 5\ \mu\text{m}$) of the MZI contain PhC and one of them also has a p-i-n diode structure whose intrinsic region is the PhC [80]. (b) Schematic representation of the p-i-n diode. *Plot is not drawn for scale and SiO_2 layer at the bottom is not shown.*

The proposed design here is a MZI-based modulator whose arms are composed of PhCs. One of the arms has n-type and p-type doped regions which squeeze the PhC so that a p-i-n diode structure is formed and its intrinsic region is that PhC. The purpose of this structure is to inject free carriers (hole and electron) into the intrinsic region (PhC) with applied electric signal to the diode. The illustration of the proposed modulator is provided in Fig. 4.1.

The index of the silicon bulk is changed via carrier injection but it is not the point in this design. Rather, here the variation in the index of the silicon is utilized to shift the photonic band structure of the silicon PhC. Such a shift in band diagram makes a

transition from one band to another possible at the operation frequency with a forward bias applied to the p-i-n diode. This transition means a large effective refractive index change between two states of the modulator, which results in decreasing device size and operation voltage extensively.

4.1 Band Gap Adjustment

Photonic band gap is the frequency region at which no propagation is supported by a PhC. There has been extensive number of applications based on this gap, most of them are associated with larger band gaps [92]. Here, on the other hand, it is not the case.

The main operation principle of the proposed modulator is to jump above the band gap between photonic bands and to switch the band at the operation frequency/wavelength. Thus, it is important to optimize the band structure of a PhC to be used as a phase shifter. Due to the nature of the photonic band gap, here we required to avoid to jump into the band gap during modulation of the light. In other words, gap size should be minimized as much as possible so that switching between bands is performed with the lowest optical loss and operation voltage. As a starting point, the PhC slab with hexagonal lattice of air-holes ($r = 0.3a$, $h = 0.6a$) which is mentioned in previous chapter was chosen. The size of optical band gap is directly related to the ratio of air-holes radius to thickness (r/h) [92]. The smallest size can be obtained via band structures for different ratios. Here, the thickness was taken constant and the radius was swept from $0.30a$ to $0.25a$. The result of this scanning is provided in Fig. 4.2-a. As the radius is decreased, the band diagram shifts below and the gap size varies. The focused photonic band gap is the first gap, which is the one between the first two photonic bands. For descending radius values, the gap size reduces as a point and reaches the minimum value. Further decreasing in radii results in increasing in the gap size. The change of the gap size for varying radii is shown in Fig. 4.2-b. The minimum gap occurs when the radius of air-holes becomes $0.292a$. Consequently, the optimum PhC for the optical modulation was determined as the silicon hexagonal lattice with radius of $0.292a$ and thickness of $0.6a$. The lattice constant, on the other hand, was determined by considering the optical wavelength $1.55\mu\text{m}$. The normalized frequency of 0.3080 ($\omega a/2\pi c$) was taken as $1.55\mu\text{m}$. Thus, lattice constant was determined as $0.4774\mu\text{m}$.

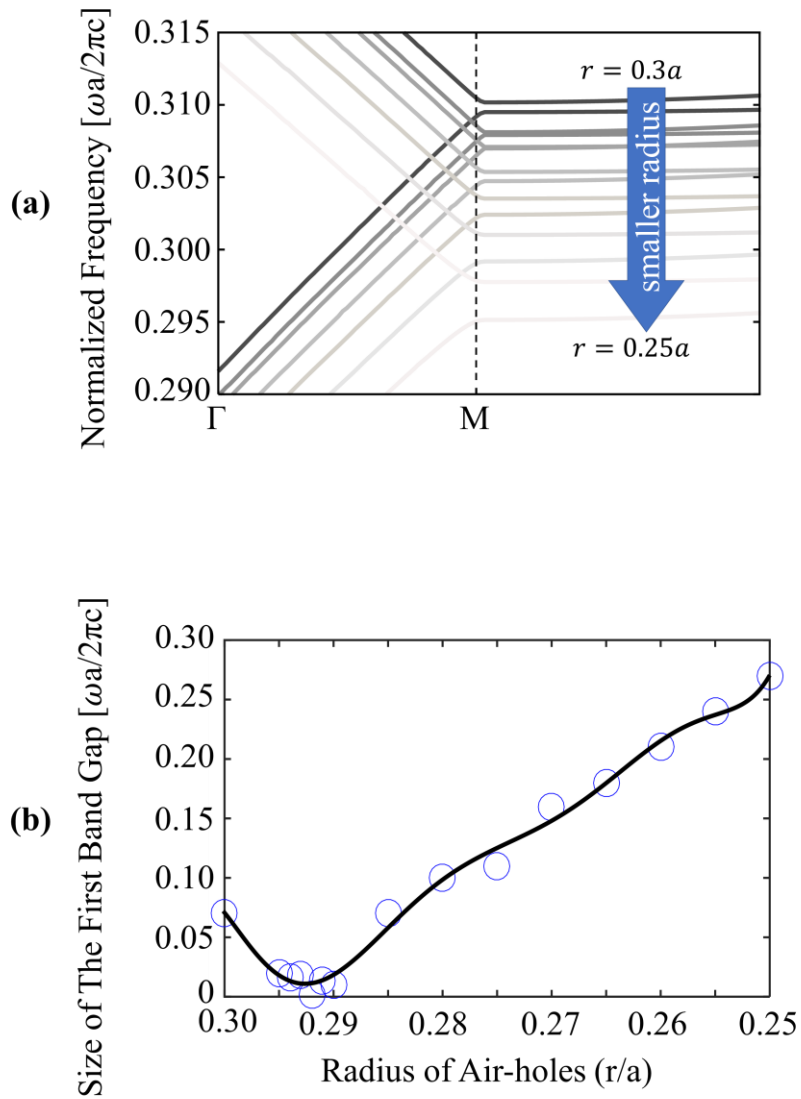


Figure 4.2. (a) Band diagrams of silicon PhCs with hexagonal lattice (thickness of $0.6a$) on SOI for different radii of air-hole. The band diagrams shift towards below with decreasing air-hole radius. (b) Size of the first band gaps for different radius. The band gap size varies for each diagram. The optimal gap size is 1.4×10^{-5} ($\omega a/2\pi c$), which occurs at $r = 0.292a$.

4.2 Band-to-Band Transition

The distinct feature of the proposed optical modulator is that unlike previously reported designs, it relies on the control of the photonic band structure for the phase shift between the on-state and off-state of the modulator. The plasma dispersion effect, which is the change of index via carrier concentration in the medium (See Section 2.1.4), has been utilized in various modulator designs for the optical modulation purposes in the literature. Here, on the other hand, the effect of such index change in silicon on the photonic band structure of the PhC was used [80].

The dielectric density of unit cells in a PhC determines the band structure. For instance, if the density increases for some reason such as bulk index, air-hole radius or locations of the air-holes [65], then the band diagram shifts towards the lower frequencies. Otherwise, the lower dielectric density is, the higher locations of the photonic bands in the diagram are. Here, we consider an index change of 0.01 in the silicon bulk with the carrier injection during the on-state. The refractive index of the silicon is 3.48 at the wavelength of 1.55 μm when no voltage is applied and no carrier is injected to the intrinsic region (PhC) of the diode (off-state). In this state, the operation band of the PhC is the second band (blue-solid) as shown by the band diagram in Fig. 4.3-b. The effective index of the crystal at the operation wavelength (1.55 μm) was calculated as -1.89 via EFCs with the method explained in Section 3.4.3. When a voltage required to inject carriers to create an index change of 0.01 in silicon is applied to the diode (on-state), then refractive index of the silicon becomes 3.47 according to eq. 2.4. Since the dielectric density of the unit cells is reduced, the photonic bands shift towards higher frequencies (Fig. 4.3). Thus, the PhC operating on the second band (blue-solid) starts to operate on the first photonic band (red-dashes). After calculating the effective index of the PhC for the on-state of the modulator, we obtained an index of 1.996 at 1.55 μm . In spite of the small index change in silicon bulk like 0.01, the effective index of the PhC shifted from -1.89 to 1.996 (Fig. 4.4). Such a huge variation ($\Delta n_{eff} = 3.889$) in the index made smaller phase shifter (PhC) lengths possible for a proper modulation. Furthermore, since the optical modulation relies on the band transition, at the operation wavelength PhC requires to have both positive and negative effective indices. This means that the second band at off-state and the first band at on-state should coincide (Fig. 4.4-a). It is the wavelength region that the modulator can operate (active region). Thus, the operation bandwidth of the

device is 3 nm, which will be also explained in more detail and proved in terms of the phase accumulations at other optical wavelengths in the section 5.1.

In the MZI-based modulator here, the intensity contrast between the on-state ($V_{Sig} = V_{DC}$) and off-state ($V_{Sig} = 0 V$) was created via the π radian difference from the phase accumulated in the arms of the MZI during the two states. When the required phase shifter length for π phase shift is calculated, one can reach an extremely short length ($\sim 200\text{nm}$). Although it is theoretically possible, the length here need to be a few micrometers for the sake of preservation of the photonic crystal functionality. In order to determine the length of the phase shifter, several parameters such as the lattice constant of the PhC (a), effective index change (Δn_{eff}) and the integer multiples of π ($m \cdot \pi$) were considered. Then, the PhC length was determined as $5.788 \mu\text{m}$, which is $7a\sqrt{3}$ where lattice constant a is $0.4774 \mu\text{m}$.

The width and thickness of the crystal was adjusted as $1.91 \mu\text{m}$ ($4a$) and $0.286\mu\text{m}$ ($0.6a$), respectively. Note that, the width of the PhC is too wide for a single mode transmission and there is a transition from thin single mode waveguide to thick PhC. Such a transition would create an optical loss. The proposed solution for this loss is the adiabatic transition. In other words, the width of the waveguide is increased up to the PhC very slowly so that the effect of the width difference is neglectable [64].

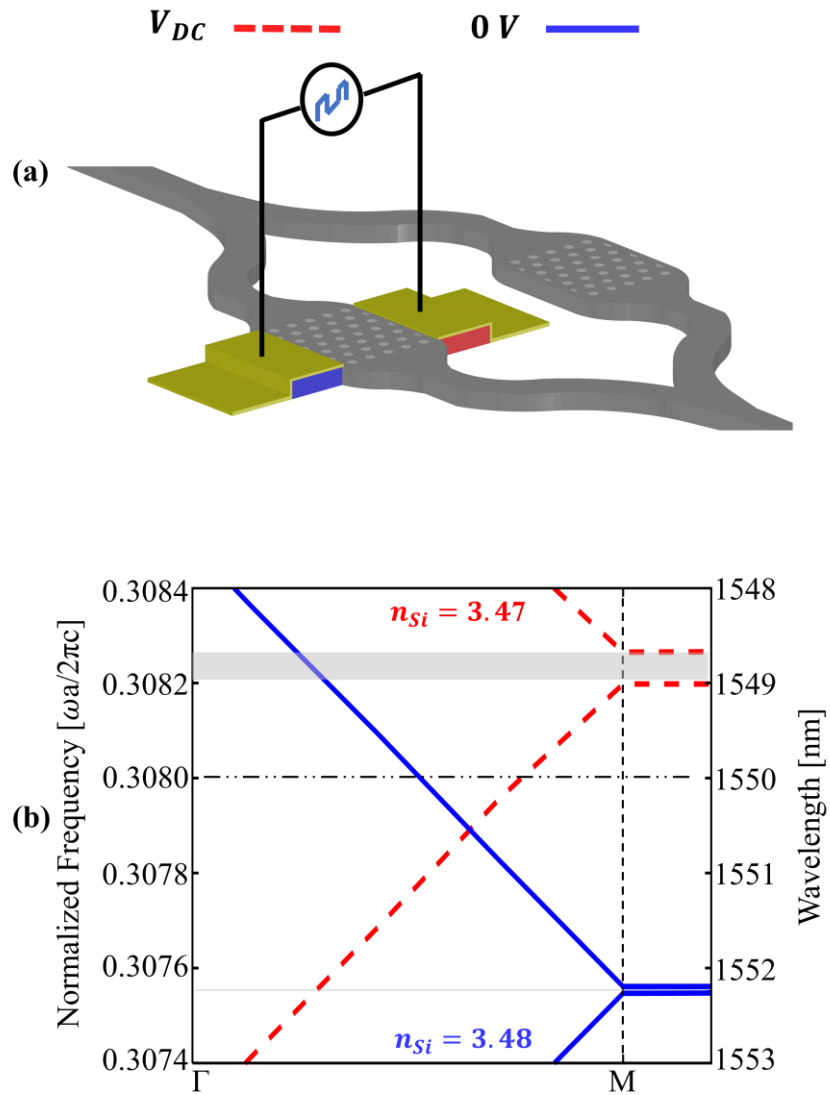


Figure 4.3. (a) Schematic representation of the MZI-based optical modulator for off-state (blue-solid) and on-state (red-dashed). The arms of the MZI are composed of identical hexagonal PhCs with $r = 0.292a$ and $h = 0.6a$ (lattice constant $a = 0.4774\mu m$). One of the arms consists of a p-i-n diode for carrier injection during on-state. Note that SiO_2 layer at the bottom is not seen in the illustration (See Fig. 4.5). (b) The band diagram of the phase shifter (PhC) for TM-like polarization at two states. The refractive index of the silicon bulk ($n_{Si} = 3.48$) at off-state becomes 3.47 when state of the modulator is switched to on-state with applied voltage of V_{DC} . The horizontal black line emphasizes the wavelength of 1.55 μm . Note that band gaps are represented with gray-shaded areas.

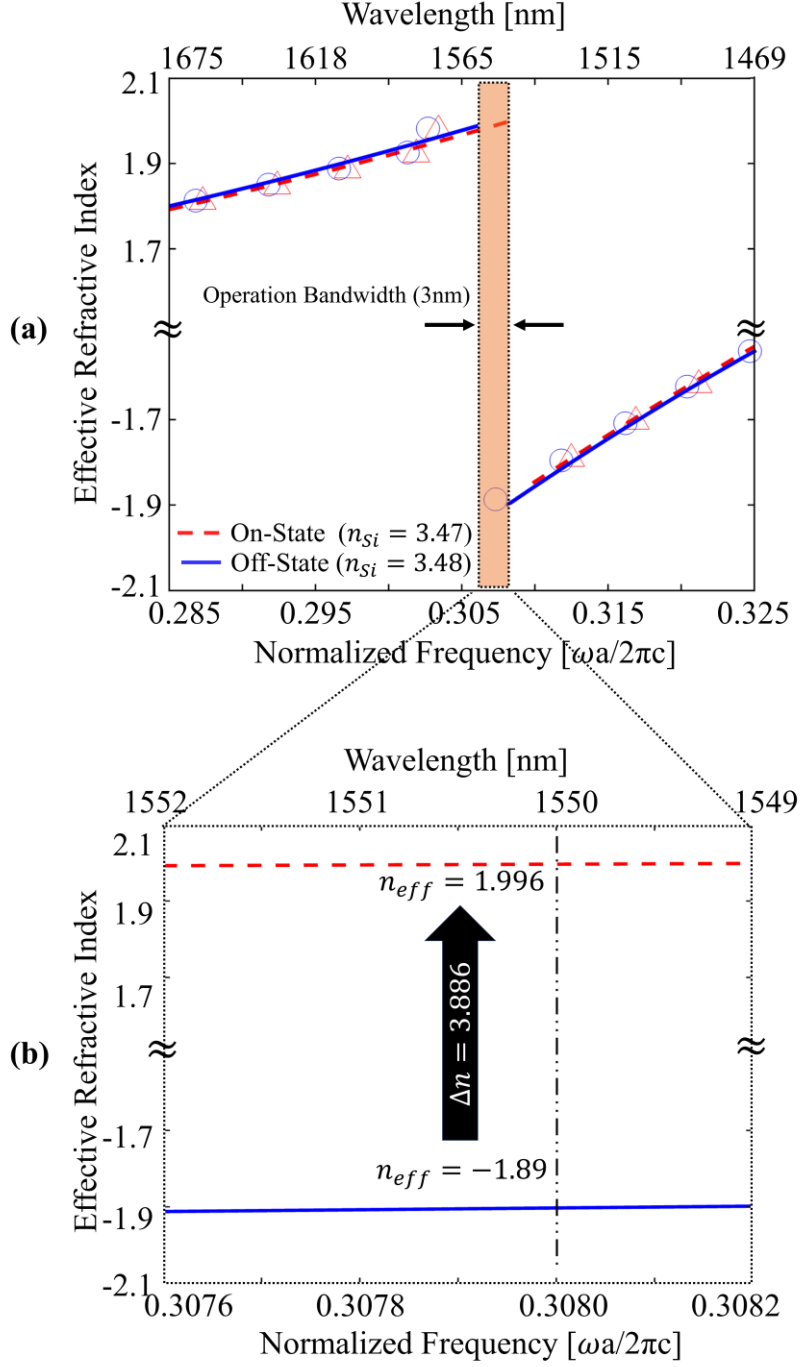


Figure 4.4. (a) Effective refractive index of the phase shifter (PhC) calculated via EFCs at the off-state (blue-circle, solid) and on-state (red-rectangle, dashes) of the modulator. Circles and Rectangles represent effective indices. Solid and dashed lines are the fitted data extracted from the exact index values for off-state ($n_{Si} = 3.48$) and on-state ($n_{Si} = 3.47$), respectively. (b) The focused view of the shaded area in (a). In this region the phase shifter (PhC) can be switched to have positive and negative effective indices during on-state and off-state, respectively. The band-to-band transition creates an index shift from -1.89 to 1.996 ($\Delta n_{eff} = 3.886$).

4.3 The P-I-N Diode

The band-to-band transition performed with the plasma dispersion is based on the carrier injection. In order to introduce free carriers to the PhC, a p-i-n diode (Fig. 4.5) was utilized. In the previous chapter, shift from the second band to the first band was performed via an index change of 0.01. According to Soraf and Bennet [36] (eq. 2.4), in order to create such a change hole and electron carrier injection of $0.41 \times 10^{19} \text{ cm}^{-3}$ is required. The determination of the diode parameters and operation voltage diode analysis was conducted.

4.3.1 Determination of Diode Parameters

The p-i-n diode specification is actually the solution of the electron-hole continuity equations and Poisson equation. The continuity equations provide information about the change of electron (eq. 4.1) and hole (eq. 4.2) concentrations with diffusion or drift in time. The first term in the continuity equations is the effect of the diffusion on the carrier motion. If there is a concentration gradient in the medium, this term contributes to the transportation of the carriers which is proportional to the diffusion coefficients D_n and D_p for electron and hole, respectively. The second term represents the drift component of the motion. It is directly related to the electric field \mathbf{E} and carrier mobilities (μ_n and μ_p). The Poisson equation (eq. 4.3) presents the correlation between the electrostatic potential Φ and the charge distribution ρ . The term ϵ represents the permittivity of the medium. Also, the contributors of the charge distribution are donor concentration (N_D), acceptor concentration (N_A), hole (p) and electron (n) concentrations.

$$\frac{dn}{dt} = \frac{1}{q} \nabla \cdot \left(qD_n \frac{dn}{dx} + q\mu_n n \mathbf{E} \right) \quad (4.1)$$

$$\frac{dp}{dt} = -\frac{1}{q} \nabla \cdot \left(qD_p \frac{dp}{dx} + q\mu_p p \mathbf{E} \right) \quad (4.2)$$

$$\nabla \epsilon \cdot \nabla \Phi = -\rho = -q(N_D - N_A + p - n) \quad (4.3)$$

Note that the relation between electrostatic potential and electric field is $\mathbf{E} = -\nabla\phi$. If we substitute the electric field terms in the continuity equations with this relation, then three partial differential equations for three unknowns (ϕ , p and n) come up. The solution of these equations could be conducted with iteratively. There are various tools for iterative solution. In this thesis, Synopsys Sentaurus Device, which is a program capable of utilizing numerical analysis of semiconductor devices [93], was used. Moreover, in order to obtain more realistic results, several recombination mechanisms such as Auger (eq.4.4), Shockley-Read-Hall (SRH) (eq.4.5) and radiative (eq.4.6) recombination were taken into account during numerical analysis.

$$R_{Auger} = (A_n n + A_p p)(np - n_i^2) \quad (4.4)$$

$$R_{SRH} = \frac{np - n_i^2}{\tau_n(p + p_1) + \tau_p(n + n_1)} \quad (4.5)$$

$$R_{rad} = B(np - n_i^2) \quad (4.6)$$

where A_n , A_p , B and n_i represent Auger, radiative combination rate coefficients and the intrinsic carrier density, respectively. In the eq. 4.5, τ_n and τ_p are the electron and hole lifetimes. They determine the SRH recombination rate as well as the trap energy levels, which are associated with the terms p_1 and n_1 . During the simulations electron and hole life times were taken as equal. Also, it was assumed that trap energy level is at the midpoint of the energy band gap ($n_1 = p_1 = n_i$).

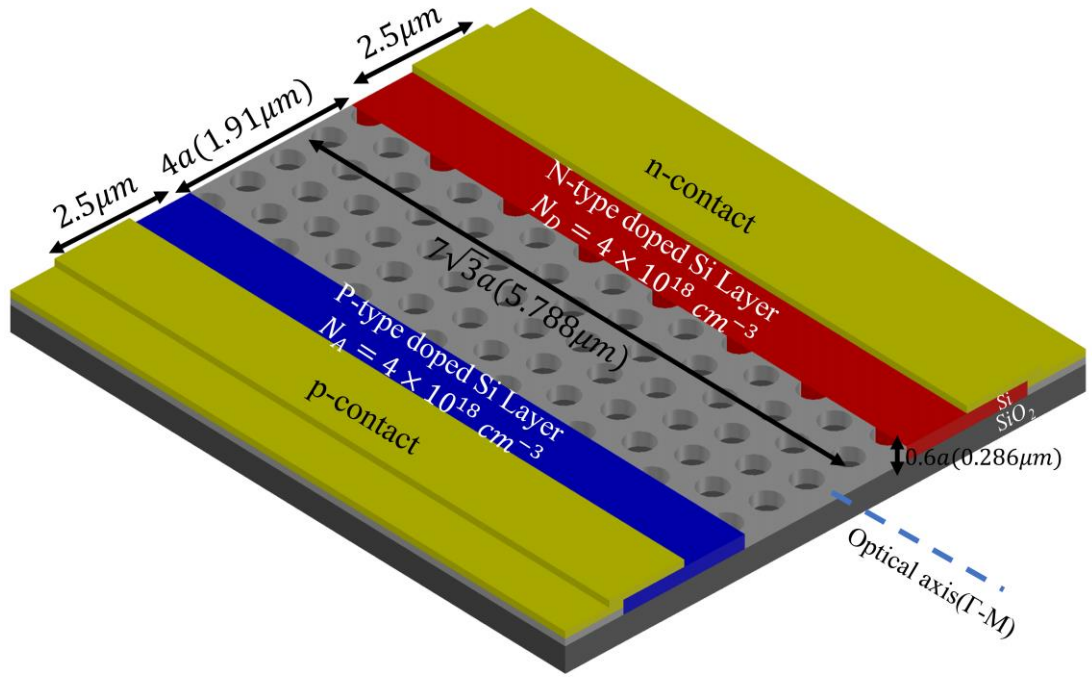


Figure 4.5. Schematic representation of the proposed p-i-n diode whose intrinsic region is the PhC with hexagonal lattice. The physical dimensions are assigned on the plot. The calculated doping density for a proper injection is $4 \times 10^{18} \text{ cm}^{-3}$.

4.3.2 The Structure of the Proposed P-I-N Diode

The free carrier injection required for index change is performed with the forward biased diode. The p-contact and n-contact of the diode behave as positive and negative terminal. The majority carriers in the n-doped and p-doped regions around the intrinsic region (PhC) start to diffuse towards PhC. The relation between the doping densities of the doped regions and operation voltage required to create free carrier concentration of 0.41×10^{19} for the PhC, whose physical dimensions were determined in the previous section, were calculated according to Poisson equation and continuity equations via Sentaurus Device. The result is shown in Fig. 4.6-a. As one can observe, the operation voltage decreases with increasing doping concentration. Although reducing the bias voltage is advantageous in terms of power consumption, high doping concentration would cause nonuniformity in the carriers injected to the intrinsic region. Thus, as an optimum case, doping density for both n-type and p-type was determined as $0.4 \times 10^{19} \text{ cm}^{-3}$ and corresponding biasing voltage is 1.091V. Consequently, a uniform carrier distribution in PhC and low switching voltage were obtained at the

same time. Moreover, the carrier injected with these doping densities for different biasing was examined as shown in Fig. 4.6-b. During on-state with 1.091V, the free carrier concentration reaches to the expected value.

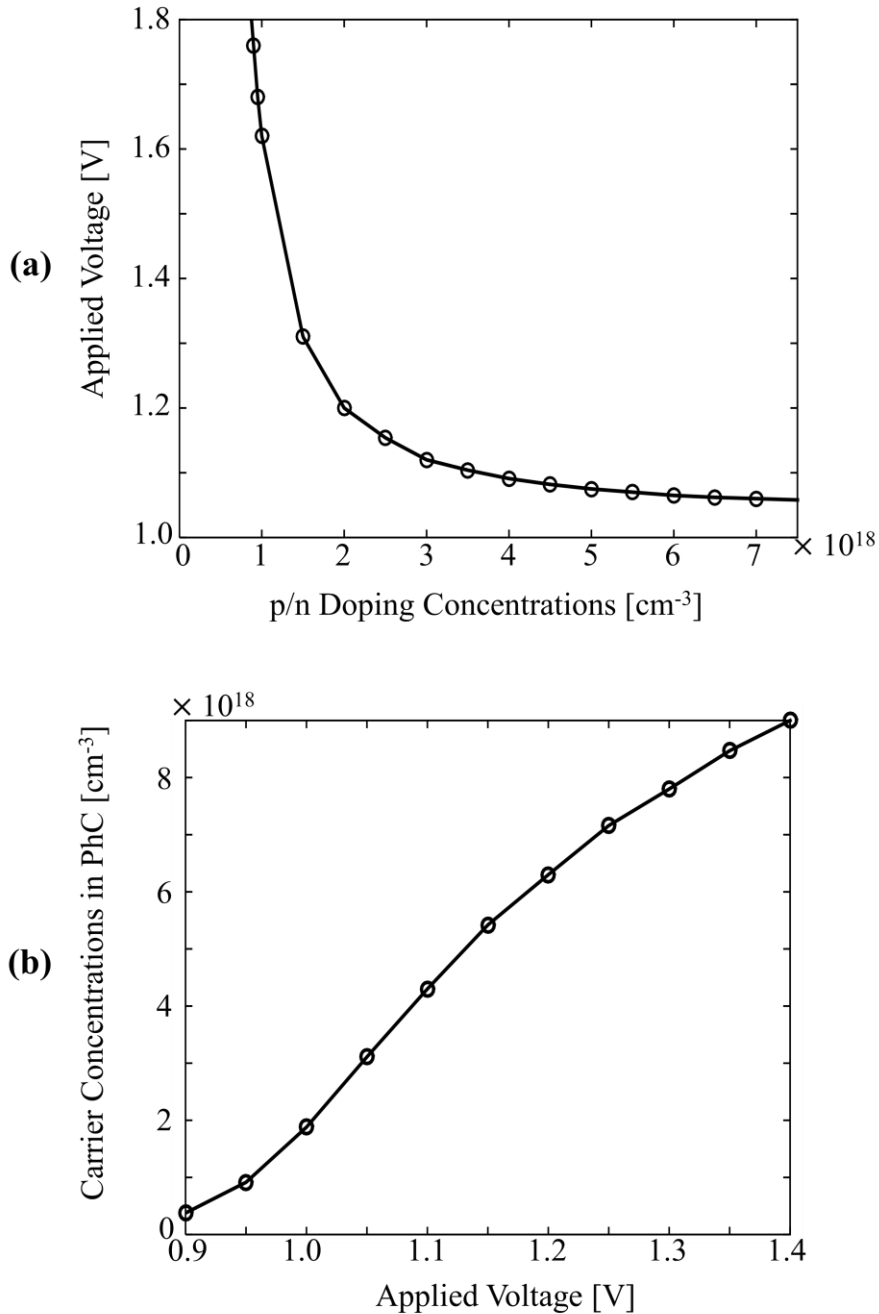


Figure 4.6. (a) The operation voltage values for different doping densities in order to obtain carrier injection of $4.1 \times 10^{18} \text{ cm}^{-3}$ in the intrinsic region (PhC) (b) Free carrier concentration in PhC during on-state for various operation voltages in the proposed p-i-n diode.

CHAPTER 5

RESULTS AND DISCUSSION

5.1 Optical Modulation Operation

The MZI-based optical modulator with identical PhCs in its arms was designed with the parameters determined in the previous chapter. This structure has two switching states namely off-state and on-state. At the off-state, no voltage is applied to the p-i-n diode and both arms of the MZI have the same phase accumulation. In other words, the relative phase in the waves in the arms is zero, which leads to constructive interference. Thus, the optical intensity at the output becomes maximum. During the on-state, however, voltage of 1.091V is applied and a nearly 29π radian phase shift is created along the arm with the p-i-n diode at $1.55\mu\text{m}$ (Fig. 5.1-a). Therefore, the destructive interference occurs at the output side of the MZI, which means the output light intensity is minimum. Consequently, the applied electrical signal controls the phase of the light, which is transformed into intensity contrast at the output of the MZI. Operation wavelength of $1.55\mu\text{m}$ is not the only optical wavelength this modulator can work at. Since it relies on the transition from the second photonic band to the first one, the wavelength interval covering such transition can also be supported by this device, which was named as active region and shown in Fig. 4.4. In order to be sure for the supported wavelength interval, the spectral phase difference between two arms of the MZI during on-state was obtained (Fig. 5.1-b). The phase difference $\cos\phi$ (Recall eq. 2.10) in the interval of 1549nm-1552nm varies between -0.9964 and -0.9974. Such values are related to the destructive interference and there exists a high enough intensity contrast between two states of the modulator. Therefore, all active region of

the PhC can be utilized for modulation purposes, which means the bandwidth of the modulator ($\Delta\lambda$) is 3nm.

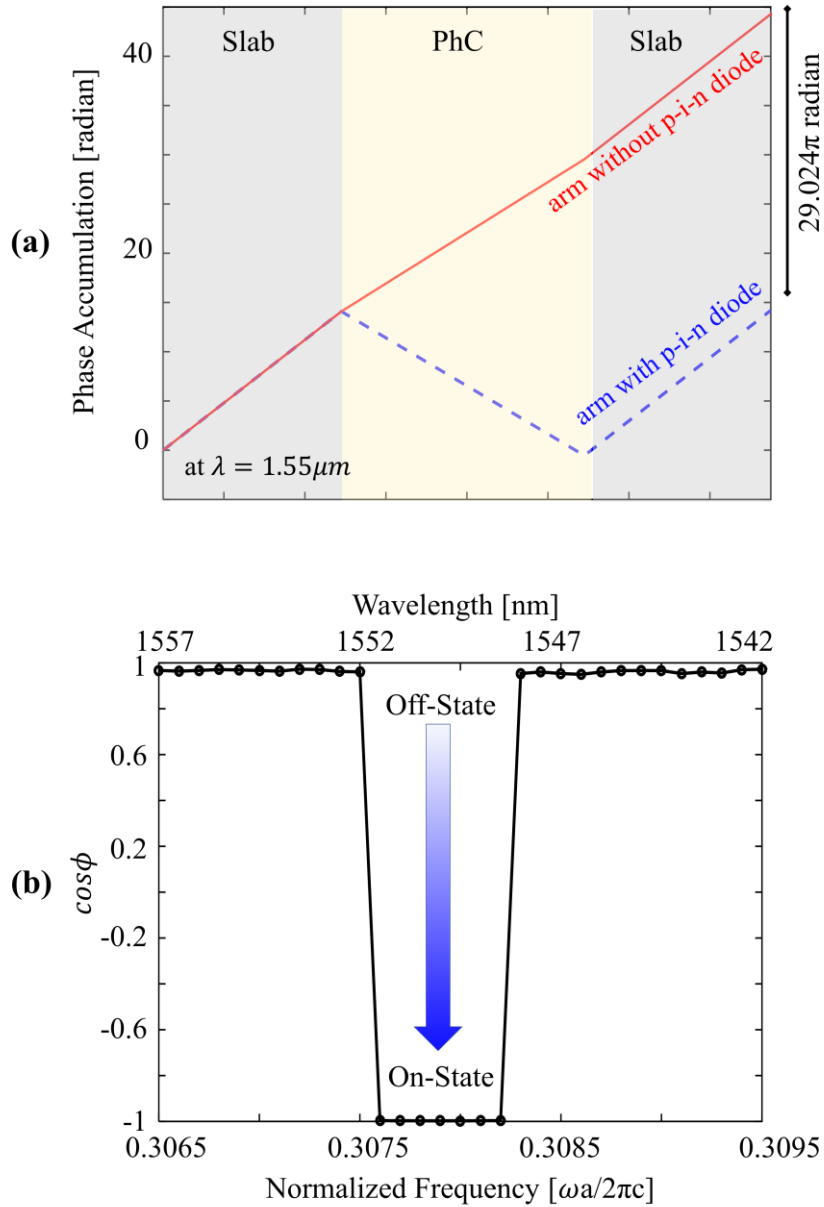


Figure 5.1. (a) The phase accumulation along the both arms of the MZI at $1.55\mu\text{m}$ during on-state. Since PhC in the biased p-i-n diode has a negative effective index, its contribution to the phase accumulation becomes negative along the PhC. Such unusual behavior creates a phase difference between two arms ($\sim 29\pi$ radian), which leads to destructive interference. (b) Spectral phase difference between the arms during on-state ($V_{Sig} = 1.091V$) for the wavelength range of 1542nm-1557nm. The optical modulation occurs in the 1549-1552nm range.

5.2 Modulation Speed

One of the most important features of an optical modulator is the speed of optical modulation. That is, the time required to switch the state of the modulator between on and off. Here, the proposed modulator utilizes the carrier injection via a p-i-n diode for switching. Therefore, the speed of the device is determined by examining the diode characteristics. The faster carriers are injected to PhC during on-state and vanished in PhC during off-state, the higher the operation speed of the modulator is. In order to find the time between the state, the idea that current value reaches to its steady-state value when the transition is completed was used. Thus, a time dependent simulation on the diode was performed via Sentaurus Device for the forward bias current (Fig. 5.2). The oscillations on the current finish at 2 picoseconds and current reaches the operation current value (0.66 mA). In other words, the maximum switching occurs with the frequency of 250GHz for one optical channel. When more than one channel is available in the system, then this speed is multiplied by the number of channel. This makes much faster modulation speeds like terahertz rates possible [5]. For instance, a four-channel system has a speed of 1THz.

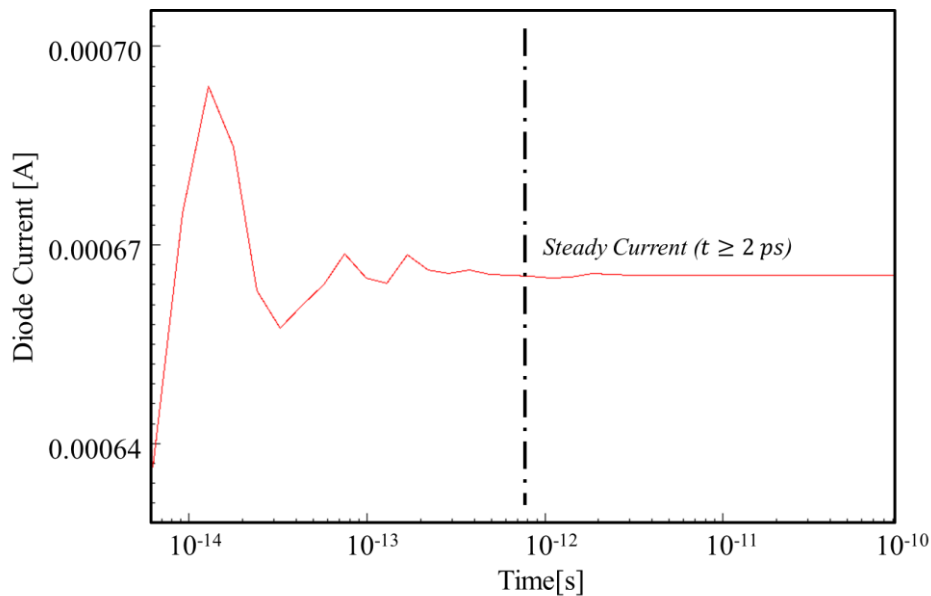


Figure 5.2. Time response of the current passing through the p-i-n diode under the forward bias obtained via time dependent simulations on the diode. After 2 picoseconds the current becomes constant and the state of the modulator changes.

5.3 Optical Insertion Loss

The insertion loss of an optical system is an important concern. It determines the optical intensity at the output of the corresponding system. It can be obtained from the optical transmission behavior via FDTD method. In order to characterize the propagation loss of the proposed modulator, we have run several FDTD simulations and obtained the transmission spectrum along the arms of the Mach-Zehnder interferometer (MZI) when the modulator is at on-state. As can be seen in Fig.5.3, the reference arm (no p-i-n diode) has an insertion loss of ~ 1.08 dB while the device arm (p-i-n diode and applied voltage of 1.091 V) has a loss of ~ 1.05 dB at the operating wavelength ($1.55\mu\text{m}$). In other words, the loss along the device arm is 1.08 dB and 1.05dB during off-state and on-state, respectively. Such a loss value is low enough for a proper optical modulation. That is, modulator operates in the high transmission region.

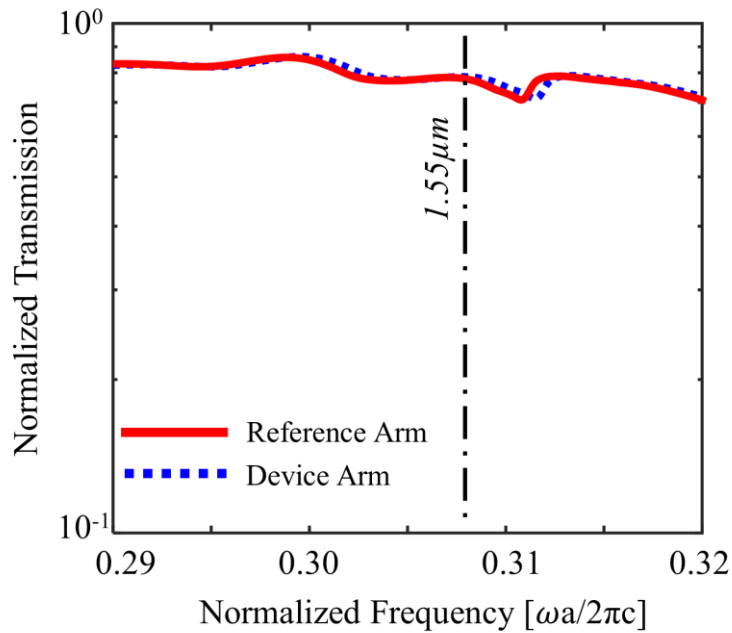


Figure 5.3. Optical transmission spectrum for the reference (no-diode, red-solid) and device arms (diode biased with 1.091V, blue-dashes) of the MZI during on-state. Black horizontal line emphasizes the optical operation wavelength ($1.55\mu\text{m}$).

5.4 DC Analysis of the Device

The physical dimensions and biasing voltage required for the proper modulation were determined in the section 4.3.2. The current-voltage characteristics was also obtained (Fig. 5.4). The dc operation point of the device is 1.091 V and 0.66 mA. Under this dc condition, the forward bias resistance of the diode was determined as 125Ω , which is the inverse slope of the current-voltage slope at the dc operation point (eq. 5.1). Forward-bias resistance creates a DC power consumption ($P = \frac{V^2}{R}$). Such resistance corresponds to $54 \mu\text{W}$.

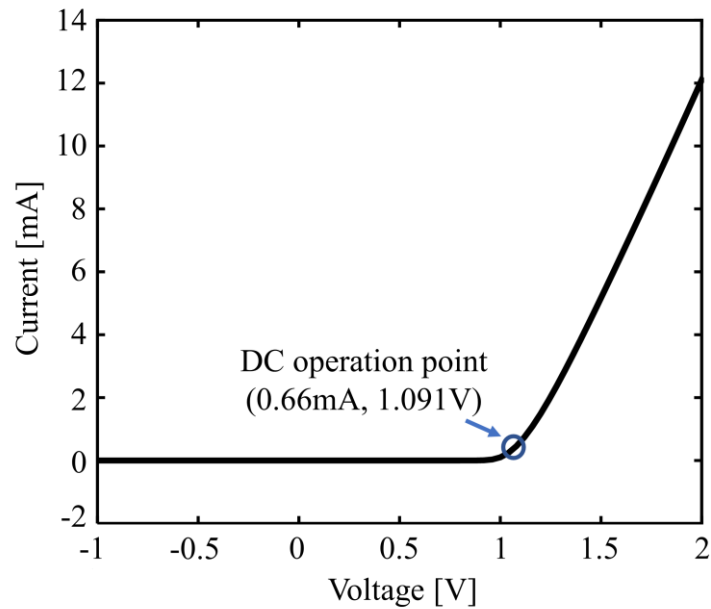


Figure 5.4. DC characteristics of the proposed p-i-n diode. The blue circle represents the DC operation point of this modulator (0.66mA, 1.091 V).

Another important concern is the forward bias capacitance of the diode. It affects both the switching speed and dynamic power consumption. The source of the forward bias capacitance is the minority carriers diffused from n-type and p-type doped regions to the intrinsic region. The minority electron and hole carrier densities for varying biasing voltage was obtained. Then, total charge available (Fig. 5.5-a) in the intrinsic region was calculated from the relation between the carrier density and total charge in a medium (eq. 5.2). The total charge (Q_{total}) is the multiplication of the hole-electron carrier density (h, n), unit charge (q) and volume of the corresponding medium (\hat{V}). Here, the volume of the intrinsic region is $\hat{V} = 5.788\mu m \times 1.91\mu m \times 0.286\mu m = 3.16\mu m^3$. Capacitance is the change rate of the total charge with varying voltage (eq. 5.3). The forward-bias capacitance of the diode for different voltages is shown in Fig. 5.5-b. At the DC operation condition here, capacitance was determined as 24pF. Capacitance is related to the dynamic power consumption during switching between 0V and 1.091V. However, since capacitance value is low, dynamic power is neglectable compared to DC power consumption.

$$R = \left(\frac{dI}{dV} \right)^{-1} \Big|_{DC} \quad (5.1)$$

$$Q_{total} = q \cdot (h + n) \cdot \hat{V} \quad (5.2)$$

$$C = \left(\frac{dQ}{dV} \right)^{-1} \Big|_{DC} \quad (5.3)$$

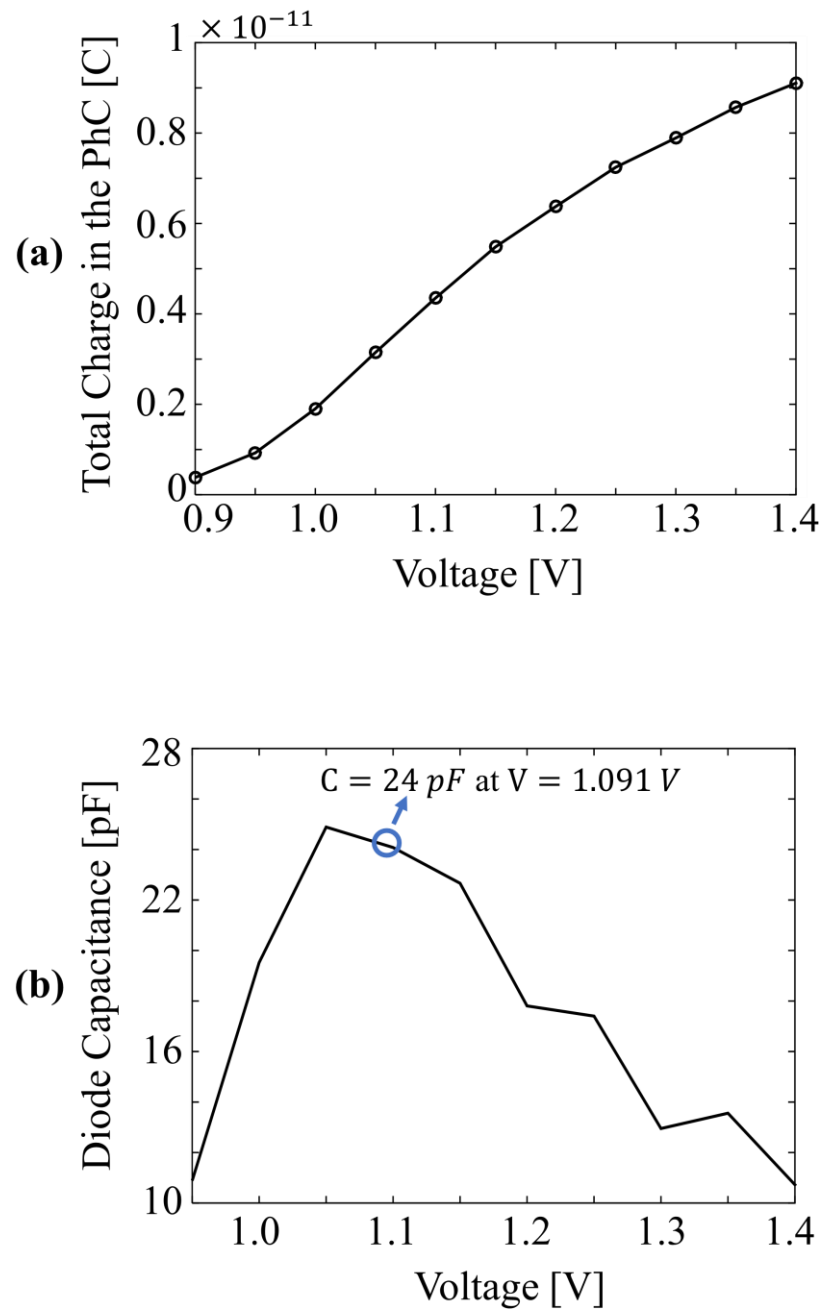


Figure 5.5 (a) The total charge accumulated in the intrinsic region (PhC) for different forward biases. (b) Diffusion capacitance of the diode for varying voltage under forward bias condition. At the dc operation point (0.66mA, 1.091V), the capacitance is 24pF.

5.5 Tuning Range

The study started with the assumption that when the state of the modulator switches to on-state via applied voltage, refractive index change of 0.01 occurs in the silicon bulk. Throughout the study, all analysis and design procedures were performed for such amount of change and corresponding dc operation point (0.66mA, 1.091V). With this value, the operation bandwidth has been determined to be 3 nm (1549-1552 nm) as presented in the Fig. 4.4 and Fig. 5.1. If the biasing voltage is increased, then the index change of the bulk increases with more carrier injection. The photonic band diagram of the phase shifter (PhC) shifts toward much higher frequencies. This means that larger bandwidths for the modulator are possible and the modulator can be tuned with varying bias.

In order to examine the tuning range of the modulation, we have also extended our simulations with a variety of higher voltages that lead to higher carrier densities and different band structures (Fig. 5.6). Obtained operational bandwidth of the modulation with respect to the applied voltage levels are presented in Fig.5.7.

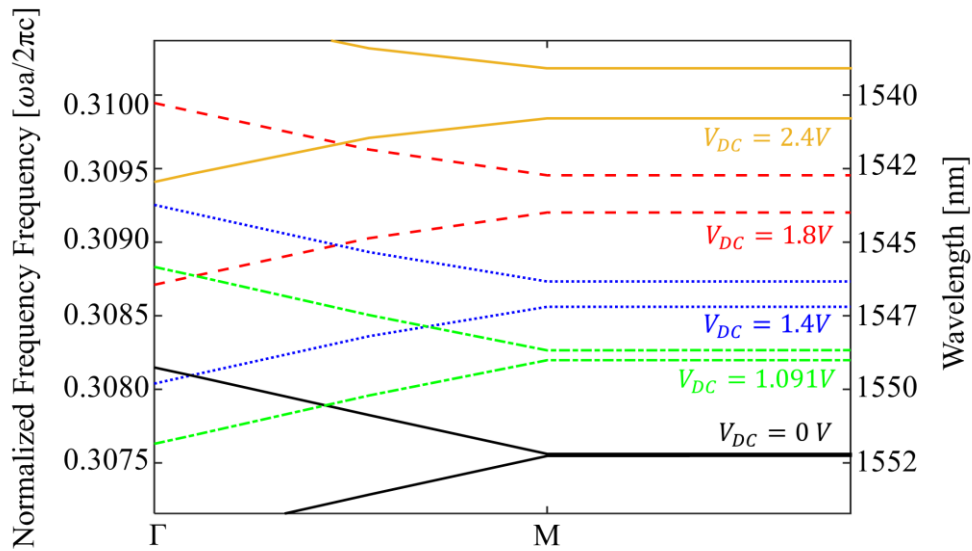


Figure 5.6. Photonic band diagrams for various biasing voltages. As the biasing voltage increases the bands shift more (from 3 nm to 11 nm with 2.4V).

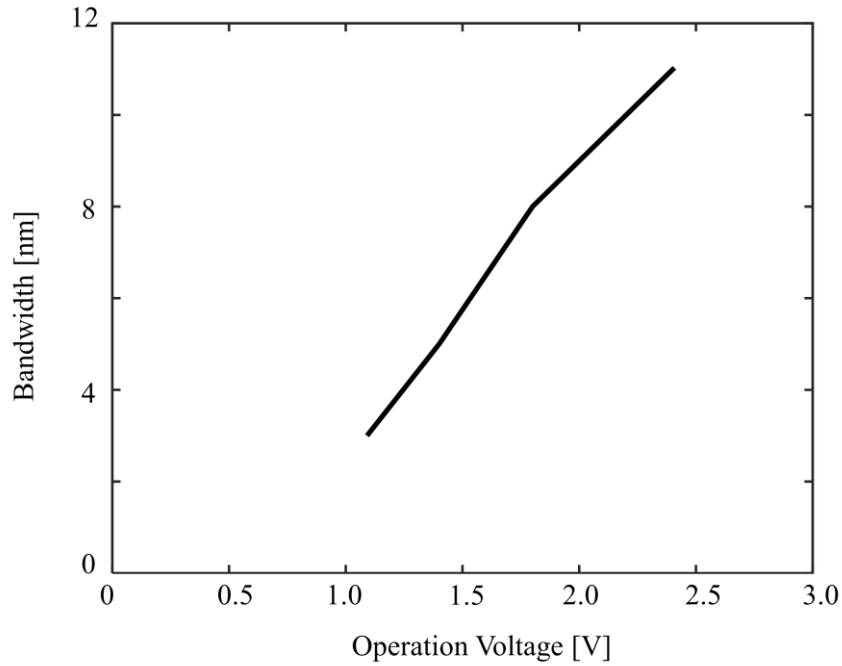


Figure 5.7. Operation bandwidth of the modulator for different on-state voltages. The bandwidth increases with increasing voltages.

5.6 Field Distribution During Optical Modulation

Up to this point, we have mentioned the photonic band calculations and its consequences on the phase accumulation along the arms of the MZI. In order to provide more convincing proves regarding the modulator, field distributions along the arms were examined. The distributions were obtained under the same simulation parameters mentioned in section 3.2.3 and for the operation voltage of 2.4V (on-state) at $1.55\mu\text{m}$. The results are shown in Fig. 5.8. As one can see, at the input side of the PhC, there is no phase difference between the field distributions of the waves, which means they are in-phase. However, at the output of the PhC region, the phase of the field distribution along the device arm (with biased p-i-n diode) is shifted so that there exists a π radian phase difference between the waves propagating along the device arm and reference arm (no p-i-n diode) of the MZI. In other words, it is clearly shown that waves in two arms are out-of-phase. This process is the phase modulation of the light and it is transformed into intensity contrast (intensity modulation) via MZI. At the output of the MZI, the signal is switched between its maximum and minimum intensity at off-state and on-state of the modulator, respectively.

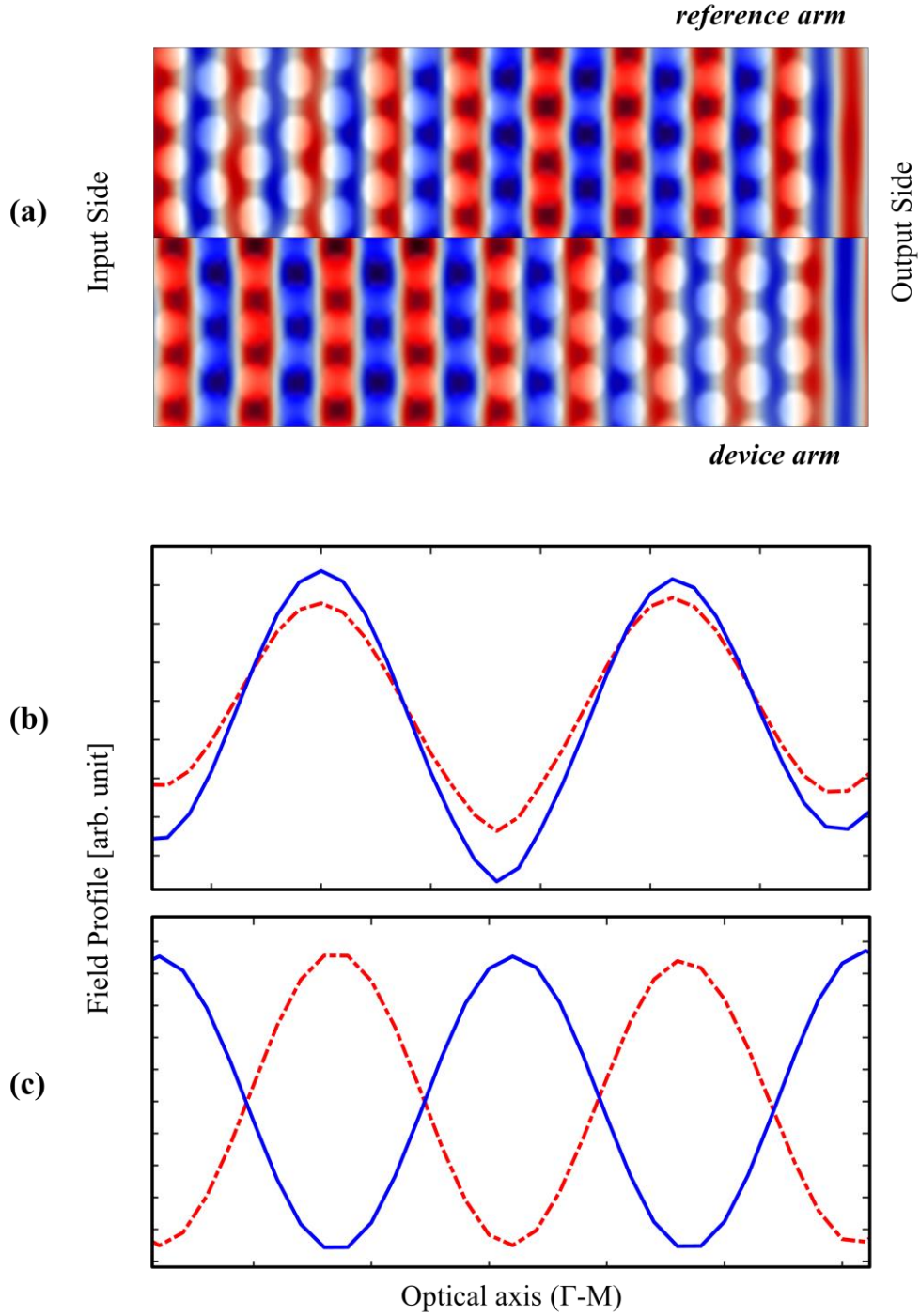


Figure 5.8. (a) Electric field distributions on the phase shifter regions (PhC) along the reference (top) and device (bottom) arms of the MZI during on-state with $V_{DC} = 2.4V$ at the wavelength of $1.55\mu m$. Each color in the distribution represents the maximum and minimum peaks of the electric field. (b) Field profile of the waves at the input side of PhC along the reference arm (red-dashes) and device arm (blue-solid). The waves are in-phase. (c) Field profile in two arms at the output side of the PhC. Due to π radian phase shift, waves are out-of-phase.

CHAPTER 6

CONCLUSION AND FUTURE WORK

The counterparts of the electrical interconnects, optical modulators, have been more and more popular for years. Especially, in the scope of silicon photonics, most of the modulators rely on plasma dispersion effect in order to perform phase modulation. However, implementation of the phase modulation in an optical system requires an extra component. A Mach-Zehnder interferometer, which provides high switching speeds and high modulation depths; but suffers from large device sizes and power consumptions is one of such structures. Other one is a ring resonator that has high operation speeds and relatively small area consumption on optical chips as well as high temperature and production sensitivity. Both type of structures was examined in terms of various figure of merits and working principles were discussed (Table 6.1). A new modulator combining most of the advantages of these modulators in a single device was studied. For that purpose, a Mach-Zehnder interferometer whose arms composed of identical PhC slabs as phase shifter was designed. The new method for creating phase difference between two arms is shifting the band diagram of the PhC via applying voltage to p-i-n diode (plasma dispersion effect), which is placed at one of the arms. Consequently, the photonic band where PhC works at the operation wavelength was changed and transition from one band to another one was performed. Of course, in order to design and optimize the PhC, several numerical simulations were conducted. Different effective index calculation methods were examined and EFCs-based approach was applied to design of the PhC. The phase shifter was defined such that when no voltage applied (off-state) both arms contributes the phase accumulation of the waves equally and that with the applied voltage to the diode at one arm (on-state), the phase is shifted and relative phase accumulation of π radian is created. Such

a phase difference was transformed into minimum intensity at the output of the MZI. During off-state, however, since waves are in-phase, output intensity is maximum. Note that although index change of the silicon bulk is low ($\Delta n_{Si} = 0.01$), the effective refractive index change is extremely high ($\Delta n_{PhC} \cong 4$) due to the band-to-band transition. In order to explain this effective index change, the relation between the polarity of its index and the photonic band at which PhC works were examined. The PhC property of supporting both negative and positive effective index was indicated with various approaches. Such a feature made a shift from negative index to positive index possible. Even the magnitude of the index change is much larger than the bulk index

change ($10 \times \Delta n_{Si}$). Thus, the proper intensity modulation was obtained with much smaller phase shifters ($\sim 5\mu$) than the MZI-based modulators in the literature (the smallest one is 80μ). Moreover, it was shown that biasing voltage for on-state could be reduced to low levels ($\sim 1V$), which is associated with low power consumption. Another important concern, operation speed, was examined with time dependent iterative simulations. Even for one-channel-modulation, modulator operates at high speed ($\sim 250GHz$). With multichannel, extremely high speeds on the order of terahertz are possible. Of course, this operation conditions were not applicable just for 1.55μ . The modulation bandwidth was determined as $3nm$ for $1.091V$ and this interval was shown to be wider with higher operation voltages. Consequently, area and power efficient, high speed optical modulator would be a promising structure and idea for large-scale optical integrated circuits and integrated systems. The structure is compared with several design reported in the literature in the Table 6.1.

This thesis showed theoretically that band-to-band transition could be utilized for optical modulation processes. Although the proposed structure was numerically proven and was examined in terms of all concerns regarding optical modulators, it is important to implement the structure on an optical chip. Thus, the next stage for this research is to fabricate the modulator and perform an experiment on it. For that purpose, a MZI for $260nm$ -Si wafer was designed with new PhC parameters. It was fabricated by e-beam lithography and etched with ICP-RIE etching method. The n-type and p-type doped regions will be doped and metals will be deposited for electrical connections as next moves. After preparing the optical modulator, its optical operation will be tested.

Figure 6.1. Comparison of several designs in the literature with the proposed design

	Structure	Type of Carrier Motion	Phase Shifter Length or Radii	Modulation Speed	Operation Voltage	Optical Working Spectrum
Hinakura, Y. <i>et al.</i> [44]	MZI with MOS process and Slow Light concept on PhC	depletion	200 μm	25Gb/s	Offset=-1V, $V_{PP}=2\text{V}$	20 nm
Gu, L. <i>et al.</i> [52]	MZI with P-I-N junction and Slow Light concept on PhC	injection	80 μm	1Gb/s	$V_{PP}=3\text{V}$ (2V on-state voltage)	> 10 nm
Xu, Q. <i>et al.</i> [72]	Ring resonator with P-I-N junction	injection	5 μm	12.5 Gb/s	$V_{PP}=8\text{V}$	~1nm
Xu, Q. <i>et al.</i> [75]	Ring resonator with P-I-N junction	injection	6 μm	1.5 Gb/s	$V_{PP}=6.9\text{V}$ (from -2.8V to +4.1V)	0.04nm
Xiao, X. <i>et al.</i> [78]	Ring resonator with PN junction	depletion	10 μm	44 Gb/s	$V_{PP}=3\text{V}$	~0.02nm
Proposed Design	MZI with P-I-N junction and band-to-band transition concept on PhC	injection	5.899 μm	250 GHz	$V_{PP}=1.091\text{V}$	> 3 nm

REFERENCES

- [1] Busignies, H., "Communication channels," *Sci. Amer*, vol.227, pp. 99-113, Sept. 1972.
- [2] Senior, J. M. *Optical fiber communications: principles and practice*. Prentice Hall, ISBN, 136354262, 622-629,1992.
- [3] Maiman, T. H., "Stimulated optical radiation in ruby", *Nature*, **187**, pp. 493-494, 1969.
- [4] Gambling, W. A., "The rise and rise of optical fibers", *IEEE J. Sel. Top. Quantum Electron*, 6(6), pp. 1084-1093, 2000.
- [5] Bergman, K., Carloni, L. P., Biberman, A., Chan, J., & Hendry, G. *Photonic network-on-chip design*. (Springer New York, 2014).
- [6] Dimitrov, S., & Haas, H., *Principles of LED light communications: towards networked Li-Fi*. Cambridge University Press, 2015
- [7] Favre, F., & Le Guen, D. High frequency stability of laser diode for heterodyne communication systems. *Electronics Letters*, 16(18), 709-710, 1980.
- [8] Chi, Y. C., Hsieh, D. H., Tsai, C. T., Chen, H. Y., Kuo, H. C., & Lin, G. R. 450-nm GaN laser diode enables high-speed visible light communication with 9-Gbps QAM-OFDM. *Optics express*, 23(10), 13051-13059, 2015.
- [9] Tajima, K. Compensation of soliton broadening in nonlinear optical fibers with loss. *Optics letters*, 12(1), 54-56, 1987.
- [10] Carlsson, C., Martinsson, H., Schatz, R., Halonen, J., & Larsson, A. Analog modulation properties of oxide confined VCSELs at microwave frequencies. *Journal of Lightwave Technology*, 20(9), 1740, 2002.

[11] Coldren, L. A. & Corzine, S. W. Diode Lasers and Photonic Integrated Circuits. New York: Wiley, 1995.

[12] Paoli, T. L., & Ripper, J. E. Direct modulation of semiconductor lasers. Proceedings of the IEEE, 58(10), 1457-1465, 1970.

[13] Nabet, B. Photodetectors: Materials, Devices and Applications. Woodhead Publishing, 2015.

[14] Moore, G. E. "Cramming More Components onto Integrated Circuits," Electronics 38, No. 8, 114, 1965.

[15] Data Center Solutions, IoT, and PC Innovation. (n.d.). Retrieved May 13, 2018, from <http://www.intel.com/>

[16] Boyd, J. T. Photonic integrated circuits. In Photonic Devices and Systems (pp. 313-375). Routledge, (2017).

[17] Dai, D., Bauters, J., & Bowers, J. E. Passive technologies for future large-scale photonic integrated circuits on silicon: polarization handling, light non-reciprocity and loss reduction. Light: Science & Applications, 1(3), 2012.

[18] Nagarajan, R., Joyner, C. H., Schneider, R. P., Bostak, J. S., Butrie, T., Dentai, A. G., & Lambert, D. J. Large-scale photonic integrated circuits. IEEE Journal of Selected Topics in Quantum Electronics, 11(1), 50-65, 2005.

[19] Koester, S. J., Schow, C. L., Schares, L., Dehlinger, G., Schaub, J. D., Doany, F. E., & John, R. A. Ge-on-SOI-detector/Si-CMOS-amplifier receivers for high-performance optical-communication applications. Journal of Lightwave Technology, 25(1), 46-57, 2007.

[20] Muravjov, A. V., Withers, S. H., Pavlov, S. G., Shastin, V. N., & Peale, R. E. Broad band p-Ge optical amplifier of terahertz radiation. Journal of applied physics, 86(7), 3512-3515, 1999.

[21] Mekis A, Gloeckner S, Masini G, Narasimha A, Pinguet T. A grating-coupler-enabled CMOS photonics platform. J Sel Topics Quant Electron 17:597-608, 2011.

[22] Taillaert D, Van Laere F, Ayre M, Bogaerts W, Van Thourhout D, Bienstman P, et al. Grating couplers for coupling between optical fibers and nanophotonic waveguides. *Jpn J Appl Phys.* 45:6071–7, 2006.

[23] Fukuda H, Yamada K, Tsuchizawa T, Watanabe T, Shinojima H, Itabashi SI. Silicon photonic circuit with polarization diversity. *Opt Express* 16:4872–80. doi: 10.1364/OE.16.004872, 2008.

[24] Ahn D, Hong Cy, Liu J, Giziewicz W, Beals M, Kimerling LC, et al. High performance, waveguide integrated Ge photodetectors. *Opt Express* 15:3916-21, 2007.

[25] Assefa S, Xia F, Bedell S, Zhang Y. CMOS-integrated 40GHz germanium waveguide photodetector for on-chip optical interconnects. In: *Optical Fiber Communication Conference*. p. 10–2, 2009.

[26] Kang Y, Liu H, Morse M, Paniccia M. Monolithic germanium / silicon avalanche photodiodes with 340 GHz gain-bandwidth product. *Nat Photonics* 3:59–63 (2008).

[27] Michel J, Camacho-aguilera RE, Cai Y, Patel N, Bessette JT, Dutt BR, et al. An electrically pumped Ge-on-Si laser. In: *Optical Fiber Communication Conference*. Los Angeles, CA: IEEE. p. 5–7 (2012).

[28] Purnawirman, Sun J, Adam TN, Leake G, Coolbaugh D, Bradley JDB, et al. C- and L-band erbium-doped waveguide lasers with wafer-scale silicon nitride cavities. *Opt Lett.* 38:2–5 (2013).

[29] Reed, G. T., Mashanovich, G., Gardes, F. Y. & Tomson, D. J. Silicon optical modulators. *Nature Photonics* 4, 518–526 (2010).

[30] L. V. Keldysh, “Behaviour of non-metallic crystals in strong electric fields”, *J. Exp. Theor. Phys. (USSR)* 33, 994 (1957); translation: *Sov. Phys. JETP* 6, 763 (1958).

[31] Franz, W. “Einfluß eines elektrischen Feldes auf eine optische Absorptionskante”, *Z. Naturforsch., Teil A* 13, 484 (1958).

[32] Lach E. et al., “Application of electroabsorption modulators for high-speed transmission systems”, *J. Opt. Fiber Commun. Rep.* 2, 140–170 (2005).

[33] Weinberger, P. John Kerr and his effects found in 1877 and 1878. *Philosophical Magazine Letters*, 88(12), 897-907 (2008).

[34] Melnichuk, M., & Wood, L. T. Direct Kerr electro-optic effect in noncentrosymmetric materials. *Physical Review A*, 82(1), 013821 (2010).

[35] Norwood, R. A., Derose, C. T., Greenlee, C., & Yeniay, A. Organic waveguides, ultra-low loss demultiplexers and electro-optic (EO) polymer devices. In *Handbook of Organic Materials for Optical and (Opto) Electronic Devices: Properties and Applications*. Elsevier Inc. (2013).

[36] Soref, R. & Bennett, B. Electrooptical effects in silicon. *IEEE Journal of Quantum Electronics* 23, 123–129 (1987).

[37] Reed, G. T. & Knights, A. P. *Silicon photonics: an introduction*. (John Wiley & Sons, 2005).

[38] Espinola, R., Tsai, M., Yardley, J. & Osgood, R. Fast and low-power thermo-optic switch on thin silicon-on-insulator. *IEEE Photonics Technology Letters* 15, 1366–1368 (2003).

[39] Yan, S. et al. Slow-light-enhanced energy efficiency for graphene microheaters on silicon photonic crystal waveguides. *Nature Communications* 8, 14411 (2017).

[40] Yamane, T., Nagai, N., Katayama, S.-I. & Todoki, M. Measurement of thermal conductivity of silicon dioxide thin films using a 3omega method. *J. Appl. Phys.* 91, 9772–9776 (2002).

[41] Terada, Y., Tatebe, T., Hinakura, Y. & Baba, T. Si photonic crystal slow-light modulators with periodic p–n junctions. *Journal of Lightwave Technology* 35, 1684–1692 (2017).

[42] Thomson, D. J. et al. 50-Gb/s Silicon Optical Modulator. *IEEE Photonics Technology Letters* 24, 234–236 (2012).

[43] Akiyama, S. et al. 50-Gb/s silicon modulator using 250- μm -Long phase shifter based-on forward-biased pin diodes. *The 9th International Conference on Group IV Photonics (GFP)* <https://doi.org/10.1109/group4.2012.6324130> (2012).

- [44] Hinakura, Y., Terada, Y., Tamura, T. & Baba, T. Wide Spectral Characteristics of Si Photonic Crystal Mach-Zehnder Modulator Fabricated by Complementary Metal-Oxide-Semiconductor Process. *Photonics* 3, 17 (2016).
- [45] Terada, Y., Ito, H., Nguyen, H. C. & Baba, T. Theoretical and experimental investigation of low-voltage and low-loss 25-Gbps Si photonic crystal slow light Mach-Zehnder modulators with interleaved p/n junction. *Frontiers in Physics* 2 (2014).
- [46] Xu, H. et al. High-speed silicon Mach-Zehnder modulator based on interleaved PN junctions. *Optics Express* 20, 15093 (2012).
- [47] Marris-Morini, D. et al. Low loss 40 Gbit/s silicon modulator based on interleaved junctions and fabricated on 300 mm SOI wafers. *Optics Express* 21, 22471 (2013).
- [48] Xu, H. et al. Demonstration and Characterization of High-Speed Silicon Depletion-Mode Mach-Zehnder Modulators. *IEEE Journal of Selected Topics in Quantum Electronics* 20, 23–32 (2014).
- [49] Yang, L. & Ding, J. High-Speed Silicon Mach-Zehnder Optical Modulator With Large Optical Bandwidth. *Journal of Lightwave Technology* 32, 966–970 (2014).
- [50] Kajikawa, K., Tabei, T. & Sunami, H. An Infrared Silicon Optical Modulator of Metal-Oxide-Semiconductor Capacitor Based on Accumulation-Carrier Absorption. *Japanese Journal of Applied Physics* 48 (2009).
- [51] Liao, L. et al. High speed silicon Mach-Zehnder modulator. *Optics Express* 13, 3129 (2005).
- [52] Gu, L., Jiang, W., Chen, X., Wang, L. & Chen, R. T. High speed silicon photonic crystal waveguide modulator for low voltage operation. *Applied Physics Letters* 90, 071105 (2007).
- [53] Notomi, M. Theory of light propagation in strongly modulated photonic crystals: Refractionlike behavior in the vicinity of the photonic band gap. *Physical Review B* 62, 10696–10705 (2000).
- [54] Baba, T. Slow light in photonic crystals. *Nature Photonics* 2, 465–473 (2008).

- [55] Soljačić, M. et al. Photonic-crystal slow-light enhancement of nonlinear phase sensitivity. *Journal of the Optical Society of America B* 19, 2052 (2002).
- [56] Vlasov, Y. A., Oboyle, M., Hamann, H. F. & Mcnab, S. J. Active control of slow light on a chip with photonic crystal waveguides. *Nature* 438, 65–69 (2005).
- [57] Jiang, Y., Jiang, W., Gu, L., Chen, X. & Chen, R. T. 80-micron interaction length silicon photonic crystal waveguide modulator. *Applied Physics Letters* 87, 221105 (2005).
- [58] Gu, L. et. al. Silicon-on-insulator-based photonic-crystal Mach-Zehnder interferometers. *Photonic Crystal Materials and Devices IV*, <https://doi.org/10.1117/12.645287> (2006).
- [59] Cai, W. *Optical metamaterials: fundamentals and applications*. (Springer, 2016).
- [60] Pendry, J. B. Negative Refraction Makes a Perfect Lens. *Physical Review Letters* 85, 3966–3969 (2000).
- [61] Melville, D. O. S. & Blaikie, R. J. Super-resolution imaging through a planar silver layer. *Optics Express* 13, 2127 (2005).
- [62] Veselago, V. G. The electrodynamics of substances with simultaneously negative values of ϵ and μ . *Usp. Fiz. Nauk* 92, 517–526 (1964) [*Sov. Phys. Usp.* 10, 509–514 (1968)].
- [63] Jiang, Q. et al. Mechanism Analysis of the Inverse Doppler Effect in Two-Dimensional Photonic Crystal based on Phase Evolution. *Scientific Reports* 6 (2016).
- [64] Kocaman, S. et al. Zero phase delay in negative-refractive-index photonic crystal superlattices. *Nature Photonics* 5, 499–505 (2011).
- [65] Moradi, S., Govdeli, A. & Kocaman, S. Zero average index design via perturbation of hexagonal photonic crystal lattice. *Optical Materials* 73, 577–584 (2017).

[66] D. A. B. Miller, "Energy consumption in optical modulators for interconnects," *Opt. Exp.*, vol. 20, no. S2, pp. A293-A308, 2012.

[67] J. Heebner, R. Grover, and T. Ibrahim, *Optical Microresonators: Theory, Fabrication and Applications*, 1st edn., Springer Series in Optical Sciences (Springer, London, 2008)

[68] Yariv, Amnon. "Critical coupling and its control in optical waveguide-ring resonator systems." *IEEE Photonics Technology Letters* 14.4 (2002): 483-485.

[69] Almeida, V. R., Barrios, C. A., Panepucci, R. R. & Lipson, M. All-optical control of light on a silicon chip. *Nature* 431, 1081–1084 (2004).

[70] Baba, T. et al. 50-Gb/s ring-resonator-based silicon modulator. *Optics Express* 21, 11869 (2013).

[71] Manipatruni, S., Chen, L. & Lipson, M. 50 Gbit/s wavelength division multiplexing using silicon microring modulators. 2009 6th IEEE International Conference on Group IV Photonics <https://doi.org/10.1109/group4.2009.5338375> (2009).

[72] Xu, Q., Manipatruni, S., Schmidt, B., Shakya, J. & Lipson, M. 12.5 Gbit/s carrier-injection-based silicon micro-ring silicon modulators. *Optics Express* 15, 430 (2007).

[73] Manipatruni, S., Xu, Q., Schmidt, B., Shakya, J. & Lipson, M. High Speed Carrier Injection 18 Gb/s Silicon Micro-ring Electro-optic Modulator. LEOS 2007 - IEEE Lasers and Electro-Optics Society Annual Meeting Conference Proceedings <https://doi.org/10.1109/leos.2007.4382517> (2007).

[74] You, J.-B., Park, M., Park, J.-W. & Kim, G. 12.5 Gbps optical modulation of silicon racetrack resonator based on carrier-depletion in asymmetric p-n diode. *Optics Express* 16, 18340 (2008).

[75] Xu, Q., Schmidt, B., Pradhan, S. & Lipson, M. Micrometre-scale silicon electro-optic modulator. *Nature* 435, 325–327 (2005).

[76] Gardes, F. Y. et al. High-speed modulation of a compact silicon ring resonator based on a reverse-biased pn diode. *Optics Express* 17, 21986 (2009).

[77] Dong, P. et al. Low V_{pp} , ultralow-energy, compact, high-speed silicon electro-optic modulator. *Optics Express* 17, 22484 (2009).

[78] Xiao, X. et al. 44-Gb/s Silicon Microring Modulators Based on Zigzag PN Junctions. *IEEE Photonics Technology Letters* 24, 1712–1714 (2012).

[79] Bergman, K., Carloni, L. P., Biberman, A., Chan, J., & Hendry, G. *Photonic network-on-chip design*. (Springer New York, 2014).

[80] Govdeli, Alperen, et al. "Integrated Optical Modulator Based on Transition between Photonic Bands." *Scientific reports* 8.1 (2018): 1619.

[81] Yablonovitch, E. "Inhibited Spontaneous Emission in Solid-State Physics and Electronics," *Phys. Rev. Lett.* 58, 2059-2062 (1987).

[82] John, S. "Strong localization of photons in certain disordered dielectric superlattices," *Phys. Rev. Lett.* 58, 2486-2489 (1987).

[83] Notomi, M. "Theory of light propagation in strongly modulated photonic crystals: Refractionlike behavior in the vicinity of the photonic band gap." *Physical Review B* 62.16, 10696 (2000).

[84] Sakoda, K. *Optical Properties of Photonic Crystals*. Springer, Berlin: Springer, (2001).

[85] Jewell, J. L. et al. "Vertical-cavity surface emitting laser: Design, growth, fabrication, characterization," *IEEE J. Quantum Electron.* 27, 1332-1346 (1991).

[86] Cheng, C. and A. Scherer, A. "Fabrication of photonic band-gap crystals," *J. Vac. Sci. Tech. B*, vol. 13, no. 6, pp. 2696-2700 (1995).

[87] Bloch, F. "Über die Quantenmechanik der Elektronen in Kristallgittern," *Zeitschrift für Physik*, vol. 52, no. 7-8, pp. 555-600 (1929).

[88] Johnson, S. & Joannopoulos, J. Block-iterative frequency-domain methods for Maxwells equations in a planewave basis. *Optics Express* 8, 173 (2001).

[89] Oskooi, A. F. et al. Meep: A flexible free-software package for electromagnetic simulations by the FDTD method. *Computer Physics Communications* 181, 687–702 (2010).

[90] Namdar, A., Shadrivov, I. V. & Kivshar, Y. S. Excitation of backward Tamm states at an interface between a periodic photonic crystal and a left-handed metamaterial. *Physical Review A* 75 (2007).

[91] Jiang, B., Zhang, Y., Wang, Y., Liu, A. & Zheng, W. Equi-frequency contour of photonic crystals with the extended Dirichlet-to-Neumann wave vector eigenvalue equation method. *Journal of Physics D: Applied Physics* 45, 065304 (2012).

[92] Joannopoulos, J. D., Johnson, S. G., Winn, J. N., and Meade, R. D. *Photonic crystals: molding the flow of light*. (Princeton University Press, 2008)

[93] Sentaurus Device User Guide, Version K-2015.06, June 2015

APPENDIX A

PHOTONIC BAND DIAGRAM

```
; Alperen Govdeli
; METU, EEE, 2017

; The MPB code for obtaining photonic band diagram of the PhC used in
; the proposed optical modulator

; Photonic crystal slab consisting of a hexagonal lattice of air
; holes in a finite-thickness Silicon slab with a SiO2 substrate

; define silicon thickness, air-hole radius, permittivity of mediums,
; define lattice and block dimensions

; triangular lattice with vertical supercell:
(set! geometry-lattice (make lattice (size 1 1 sz)
    (basis1 (/ (sqrt 3) 2) 0.5)
    (basis2 (/ (sqrt 3) 2) -0.5)))
(set! geometry
  (list
    (make block (material (make dielectric (epsilon SiO2_eps)))
      (center 0 0 (- 0 (/ (+ h h_sub) 2)))
      (size infinity infinity h_sub))
    (make block (material (make dielectric (epsilon 1 )))
      (center 0 0 (+ 0 (/ (+ h h_sub) 2)))
```

```

(size infinity infinity h_sub))

(make block (material (make dielectric (epsilon Si_eps)))
(center 0 0 0) (size infinity infinity h))

(make cylinder (material (make dielectric (epsilon 1)))
(center 0 0 0) (radius r) (height h) )))

; 1st Brillouin zone of a triangular lattice:
(define Gamma (vector3 0 0 0))
(define M (vector3 0 0.5 0))
(define K (vector3 (/ -3) (/ 3) 0))

(define-param only-K false) ; run with only-K=true to only do this k-point
(define-param k-interp 500) ; the number of k points to interpolate
(if only-K
  (set! k-points (list K))
  (set! k-points (interpolate k-interp (list Gamma M K Gamma))))

(set-param! resolution (vector3 32 32 16))
(set-param! num-bands 8)

; Run even and odd bands, outputting fields only at the K point:
(if (= SiO2_eps (* SiO2 SiO2) )
  (begin ; we only have even/odd classification for symmetric structure
    (run-zodd (output-at-kpoint K output-efield-z))) ; for TM-like bands
  (run (output-at-kpoint K output-hfield-z) display-zparities))

(display-eigensolver-stats)

```

APPENDIX B

EQUI-FREQUENCY CONTOURS

```
; Alperen Govdeli
; METU, EEE, 2017

; The MPB code for obtaining EFCs of the PhC used in the proposed optical
; modulator

; Photonic crystal slab consisting of a hexagonal lattice of air
; holes in a finite-thickness Silicon slab with a SiO2 substrate

; define lattice constant, silicon thickness, air-hole radius, permittivity of mediums,
; define lattice and block dimensions, PML structure

; triangular lattice with vertical supercell:
(set! geometry-lattice (make lattice (size 1 1 supercell-h)
    (basis1 (/ (sqrt 3) 2) 0.5)
    (basis2 (/ (sqrt 3) 2) -0.5)))
(set! geometry
  (list
    (make block (material (make dielectric (epsilon SiO2_eps )))
      (center 0 0 (- 0 (/ (+ h h_sub) 2)))
      (size infinity infinity h_sub))

    (make block (material (make dielectric (epsilon 1 )))
```

```

(center 0 0 (+ 0 (/ (+ h h_sub) 2)))
(size infinity infinity h_sub))

(make block (material (make dielectric (epsilon Si_eps)))
(center 0 0 0) (size infinity infinity h))

(make cylinder (material (make dielectric (epsilon 1)))
(center 0 0 0) (radius r) (height h) )))

(set-param! resolution 32)
(set-param! num-bands 8)

; Mapping the k-points in k-space and interpolating them
(define (kgrid kx-min kx-max ky-min ky-max nkx nky)
  (map (lambda (kx)
        (interpolate nky (list (cartesian->reciprocal(vector3 kx ky-min))
(cartesian->reciprocal(vector3 kx ky-max))))))
      (interpolate nkx (list kx-min kx-max))))

; Frequencies above the light cone are excluded (n-lightcone = 1)
; In order to take into account these frequencies, set n-lightcone = 0

(define (wavevector-diagram kgrid parity n-lightcone)
  (map (lambda (kylist)
        (set! k-points kylist)
        (run-parity parity true)
        (map
         (lambda (band)
           (print "kgrid:, " band " ", (vector3-x (car kylist)))
           (map (lambda (freqs k)
                 (print " ", "
                        (* (if (and (positive? n-lightcone)
                                   (> (list-ref freqs (- band 1))
                                       (* n-lightcone

```

```

(vector3-norm
  (reciprocal->cartesian k)))) -1 1)
(list-ref freqs (- band 1))))
all-freqs k-points)
(print "\n")
(arith-sequence 1 1 num-bands)))
kgrid))

```

; The output will be lines of the form:

; kgrid:, band#, kx, frequencies at kys...

; “grep” function can be used to grep lines corresponds to specific band and result

; is a 100x100 matrix, which can be plotted by the help of a plotting software.

APPENDIX C

FIELD DISTRIBUTION FOR PHASE ACCUMULATION

```
; Alperen Govdeli
; METU, EEE, 2017

; The MEEP code for obtaining field distribution along the PhC used in the proposed
; optical modulator

; Photonic crystal slab consisting of a hexagonal lattice of air
; holes in a finite-thickness Silicon slab with a SiO2 substrate

; define lattice constant, silicon thickness, air-hole radius, permittivity of mediums,
; define lattice and block dimensions, PML structure

(define holes (list (make cylinder (center 0 0 0) (radius 0) (height 0) (material air))))
(define-param copy 8)

(set! geometry
  (append!
    (list (make block (center 0 0 0) (size infinity infinity h)
      (material (make dielectric (epsilon eps))))
      (make block (center 0 0 (-(/ (+ h sz) 4))) (size infinity infinity (/(- sz h) 2) ) (material
        (make dielectric (epsilon SiO2))))))
    (do ((k 0 (+ k 1))) ((= k copy) holes)
      (do ((i 0 (+ i 1))) ((= i (+ 1 1)))
```

```

(do ((j 0 (+ j 1))) ((= j 4))
  (append!
    holes (list(make cylinder (center
(+(* a(* k (sqrt 3)))(-(* i (* a (/ (sqrt 3) 2))) (- (/ sx 2) 3)))
(+(* i (* a 0.5))(-(* j a) (-(/ sy 2) 0.36))) 0)
(radius r) (height h) (material air))))))
(set-param! resolution 24) ; resolution
(define-param wcen 1.550) ; center frequency

; Source Formation
(define-param cenx (+(* -1 (/ sx 2)) 1))
(set! sources (list
(make source
(src (make continuous-src (frequency (/ 1 wcen)) ))
(component Ez) (center cenx 0 0) (size 0 (- sy 1) 0))))

; Simulation
(run-until 200 (at-beginning output-epsilon) (at-end output-efield-z))

; The output H5 file is transformed into PNG file for the time at which field reaches
; at the output of the structure. The numerical data can be taken from H5 file.

```

APPENDIX D

FIELD DISTRIBUTION (APPLICATION OF SNELL'S LAW)

; Alperen Govdeli

; METU, EEE, 2017

; The MEEP code for obtaining field distribution along the tilted PhC given in
; the Fig 3.3

; Photonic crystal slab consisting of a hexagonal lattice of air-holes in a finite-
; thickness Silicon slab with a SiO₂ substrate

; The tilt angle (T) is 75 degrees.

; define lattice constant, silicon thickness, air-hole radius, number of holes in each
; row and column permittivity of mediums, define lattice and block dimensions, PML
; structure

; Simulation parameters

(define-param res 16) ; resolution

(define-param F 2048) ; Fourier transform sampling points (ideally x^2)

; Formation of the Source

(define-param beam-waist 2.5) ; beam sigma (gaussian beam width)

(define-param rotation-angle (* (/ 0 360) 2 pi)) ; Source can be tilted (here no tilt)

(define-param source-points 60) ; number of dot sources forming the overall source

```

(define-param source-size (* 10 beam-waist)); should be bigger than beam-waist
(define-param src_list (list ))
(define-param fcn 0.64) ; pulse center frequency (1/lam0)
(define-param df 0.16) ; pulse width (freq)
(define-param f_min 1e-3) ; field decay at which simulation is stopped (1e-3 should
be enough for most cases)

```

```

(define-param r (* ra a)) ; starting radius for cylinders
(define-param aX (* (/ (sqrt 3) 2) a)) ; separation between two hole columns
(define-param d2 (* 90 aX)) ; length of PhC region

```

```

; Create vector of super-periods as d2
(define vsperiods (make-vector snum))
(do ((i 0 (+ i 1)))
  ((= i snum) vsperiods)
  (vector-set! vsperiods i d2))
(define speriods (vector->list vsperiods))

```

```

; Define block sizes
(define-param ubx (+ (list-sum speriods) (* 1 d2)))
(define-param bx (+ ubx (* ifblock 2)))
;(define-param by (* (- (+ 13 hnum) 0.5) a))

```

```

(define-param by (* (- (+ 13 45) 0.5) a))

```

```

; Define lattice sizes
(define-param sx (+ bx (* 2 ablock)))
(define-param sy (+ by (* 2 ablock)))
(define-param sz (+ h h_sub (* 2 ablock)))
; Tilt angle “ T ” of the PhC
(define-param cosT 0.9063077870366499632)
(define-param sinT -0.422618261740699436)

```

```

;; Create geometry

```

```

; Create geometry lattice
(set! geometry-lattice (make lattice (size sx sy sz)))

; Begin geometry
(set! geometry
  (append
    (list
      (make block (center 0 0 0) (size bx by h) (material (make dielectric (epsilon
Si_eps))))
      (make block (center 0 0 (- 0 (/ (+ h h_sub) 2))) (size bx by h_sub) (material
(make dielectric (epsilon SiO2_eps))))))
    (do ((i 0 (+ i 1)) ((= i (+ snum 1)) holes)
      (do ((j 0 (+ j 1)) ((= j (+ lnum 1))
        (do ((k 0 (+ k 1)) ((= k hnum))
          (append!
            holes (list
              (make cylinder
                (center
                  (- (* cosT (+ (/ (* -1 ubx) 2) (+ (* j aX) (list-sum (list-tail
(reverse periods) (- (length periods) i)))))) (* sinT (if (even? j) (- (/ by 2) (* a (+ k
0.5))) (- (/ by 2) (* a k))) (* -1 10) ) ;X
                  (+ (* cosT (if (even? j) (- (/ by 2) (* a (+ k 0.5))) (- (/ by 2) (* a
k))) (* sinT (+ (/ (* -1 ubx) 2) (+ (* j aX) (list-sum (list-tail (reverse periods) (-
(length periods) i)))))) (* -1 1) ) ) ;Y
                  0) ; Z
                (radius r)
                (height h)
                (material (make dielectric (epsilon air_eps))))
              ;(make block (center (+ (- 0 (/ bx 2) 5)) 0 0) (size 10 by h)
(material (make dielectric (epsilon Si_eps))))
              ;(make block (center (- (+ 0 (/ bx 2) 5)) 0 0) (size 10 by h)
(material (make dielectric (epsilon Si_eps))))
            ))))))))

```

```

;; Define simulation parameters
; Resolution
(set-param! resolution res)

; Source
(do
  (( r_0 (/ source-size -2) (+ r_0 (/ source-size (- source-points 1)))) ((> r_0 (/ source-
size 2)))
  (set! src_list
    (append src_list
      (list
        (make source
          (src (make continuous-src (frequency fcen) (width 3))) (amplitude
            (exp (- 0 (/ (* r_0 r_0) (* 2 beam-waist beam-waist))))))
          (component Ez)
          (center (- (* r_0 (sin rotation-angle)) (/ bx 2) (* -1 5) ) (+ (* r_0
            (cos rotation-angle)) 5 ) ))))))
  (set! sources src_list)

;; Simulation
; Run
(run-until 150
  (at-beginning output-epsilon)
  (to-appended "ez" (at-every 1 output-efield-z)))

```

; The output H5 file is transformed into PNG files for each second. The propagation
; of the field can be observed for each second.